Seismic Imaging of the Sedimentary and Upper Crustal Structures of the Western Canada Sedimentary Basin

by

Cheng Zhang

A thesis submitted in partial fulfillment of the requirements for the degree of

Master of Science

In

Geophysics

Department of Physics
University of Alberta

Abstract

Secondary converted waves from receiver functions are highly sensitive to physical properties below the Earth's surface. When modeled properly, the waveforms of converted waves offer direct constraints on the impedance contrast, depth, and P-to-S velocity ratio pertaining to sedimentary, crustal and mantle interfaces. In this thesis we introduce a nonlinear waveform inversion algorithm that matches the first 5 seconds of receiver functions recorded in the Alberta Basin within the Western Canada Sedimentary Basin (WCSB). Our algorithm searches for the optimal thickness of the sedimentary cover and shear velocities of appropriately selected layers within and below it. Combining inversions with forward simulations, we determine the supracrustal stratigraphy from the regional broadband seismic stations in the WCSB. The inverted models show east tapering sedimentary layers with their thicknesses ranging from ~6 km beneath the foothills of the Rocky Mountains to 3-4 km beneath the Alberta Basin. This finding is consistent with the sedimentary strata determined from regional well-logging data. Our shear velocity models near the top of the basement complement the existing sonic-logs or single component seismic data and offer new constraints on the subsidence history of the WCSB. The resolved range of depths (0-14 km) effectively bridges the gap between the vertical scales of well logging (0-6 km) and those of traditional broadband analysis (> 10 km) involving receiver functions and surface waves. The S-velocity model of the study area reveals (1) the existence of sedimentary low velocity zones of variable thicknesses and amplitudes, (2) the existence of upper-middle crustal anomalous shear velocity zones, and (3) the tectonic evolution history of the subsidence of the Alberta Basin. These findings contribute to better understanding of the tectonic structure and evolution history of the Western Canada Sedimentary Basin.

Acknowledgement

I would like to express my sincere gratitude to my supervisor Dr. Gu for the continuous support and careful guidance during my MSc study and research. His enthusiasm for scientific research always inspires me.

I also would like to thank my fellows and friends in the University of Alberta for the help and fun that make my life here so much enjoyable.

Finally, special thanks to my beloved partner and parents for your loves and supports throughout the peaks and valleys of my life.

Table of Contents

List of Figures

Figure 5.5. a. Optimal results from 30 inversions based on different depth intervals from 100 m to 800 m. **b.** Correlation coefficients and the percentages of LVZ recovery of the inversions of the second simulation model by using different depth intervals (100, 200, 400, 600, and 800 m, respectively). **c.** Averaged S-velocity models of the southwestern cluster by using the depth intervals of 200 (black) and 400 m (red), respectively. **d.** Two inverted models of station TD016 based on the depth increments of 200 (black) and 400 m (red), respectively.

Figure 5.6. a. A map showing the distribution of sedimentary LVZ. **b.** The average shear wave velocity model (red) for stations underlain by LVZs.

Figure 5.7. a. A map showing the values of misfit of inversion. **b**. Some inverted models of stations with (upper) and without (lower) LVZ.

Figure 5.8. Inversion models (i.e. shear velocity models) of stations showing abnormal high (**a**) and low (**b**) shear velocity zones.

Figure 5.9. Results of waveform simulations and correspondent non-linear inversion outcomes.

Figure 5.10. **a**. Input models with or without LVZs. **b**. Five high-frequency RFs computed from the given models in **a**.

Figure 5.11. Stacked high frequency RFs of selected stations.

Figure 5.12. **a**. Three input models with LVZ or HVZ. **b**. Correspondent high-frequency RFs computed from the models in **a**.

Figure 5.22. a. Basement subsidence curve of the Alberta Basin derived from 'stripping-away' method. **b**. Burial history curves of the Alberta Basin based on Well 8-17-53-21W4 (Wright et al., 1994). **c**. 3D model of the subsidence process of the Alberta Basin.

List of Symbols and Abbreviations

μ	Regularization parameter
κ	V_p/V_s ratio
D	Second-order differential matrix
$F[\mathbf{m}]$	Operator that produces the receiver function based on given model
G	Inversion kernel
W	Weighting matrix
J	Cost Function
d	Data vector
m	Model vector
$A(H,\kappa)$	Stacking amplitude in the H-κ domain
H	Thickness between the surface and the target interface

$G(\omega)$	Gaussian filter function
$H(\omega)$	Fourier transform of the receiver function
$R(\omega)$	Frequency spectrum of radial-component seismogram
$R(t)$	Radial-component seismogram
$S(\omega)$	Frequency spectrum of the source time function
$Z(\omega)$	Frequency spectrum of vertical-component seismogram
$Z(t)$	Vertical-component seismogram
c	Water-level parameter
p	Ray parameter
r_k	Amplitude of k-th ray on radial-component seismogram
$s(t)$	Source time function
w_i	Weighting factor

z_k	Amplitude of k-th ray on vertical-component seismogram
z	Depth
AGS	Alberta Geological Survey
AK135	AK135 Reference Earth Model
CANOE	Canadian Northwest Experiment
CCP	Common Conversion Point
CDF	Cordilleran Deformation Front
CRANE	Canadian Rockies and Alberta Network
EAGLE	Ethiopia Afar Geoscientific Lithospheric Experiment
GA	Genetic Algorithm
Ga	Billions of year
HVZ	High Velocity Zone

IASP91	IASP91 Velocity Model
LVZ	Low Velocity Zone
Ma	Millions of year
Pp	P converted phase generated by a given interface
PpPs	S reverberated phase generated by a given interface
PREM	Preliminary Reference Earth Model
Ps	P-to-S converted phase generated by a given interface
Q	Population size in Genetic Algorithm
RAVEN	Regional Alberta Observatory for Earthquakes Studies Network
RF	Receiver Function
SNR	Signal-to-noise ratio

TD	TransAlta Dam Monitoring Network
TOC	Total Organic Carbon Content
WCSB	Western Canada Sedimentary Basin
WRS	Winagami reflection sequence

Chapter 1. Introduction

1.1 Overview

Seismic imaging is one of the most effective tools in extracting subsurface structures, thereby providing a window into their formation and evolution (e.g. Backus & Gilbert, 1967, 1968; Aki & Lee, 1976; Dziewonski & Anderson, 1981; Woodhouse & Dziewonski, 1984; Snieder & Romanowicz, 1988; Eaton & Cassidy, 1996; Ekstrom & Dziewonski, 1998; Gu et al., 2001; Brouzidi et al., 2002; Clowes et al., 2002; Eaton & Hope, 2003; Boschi et al., 2007; Chen et al., 2015; Dokht, et al., 2016; Chen et al., 2017). Since the debut of seismic networks in the 1950s (Carpenter, 1965; Rost & Thomas, 2009; Gu, 2010), high-quality seismic signals recorded from increasingly uniform, broadband stations worldwide enabled substantial improvements in signal-to-noise ratio (SNR) and array processing techniques (Rost and Thomas, 2002). Aided by ever-improving observational constraints, researchers worldwide are increasingly able to map arrival times, amplitudes, and full waveforms of seismic energy to tangible subsurface physical attributes. Thanks to the widely used global models such as the Preliminary Reference Earth Model (PREM, Dziewonski and Anderson, 1981), IASP91 (Kennett et al., 1995), AK135 (Montagner and Kennett, 1996), GHENGIS (Roecker, 2001), EAGLE (Bastow et al., 2005), CANOE (Mercier et al., 2008), USARRAY (Henyey, 2000), CRUST 1.0 (Laske et al., 2013), and the LITHO 1.0 (Pasyanos, 2014), regional and local understandings of density, velocity, elastic moduli, as well as depth and impedance contrast of stratified layers are largely improved.

A prime example of improved seismological constraint is Western Canada Sedimentary Basin (WCSB), formed during the collision of the Pacific Plate (a oceanic plate) and the North American Plate (a continental plate) convergence and now overlay the Precambrian core of the North American Craton. Buried beneath the much younger sediment sequence, the crystalline basement of the WCSB has recorded more than three billion years of tectonic evolution of the North American craton. The WCSB stretches eastward from eastern British Columbia to western Manitoba, spanning the entirety of Alberta and parts of western Saskatchewan. It borders with

southern Northwest Territories to the north and extended southward down to the US-Canada border. The major geological units of the WCSB are the Canadian Cordillera (Price, 1994) and two primary depocenters – the Williston basin and the Alberta basin (Gerhard et al., 1990; O'Connell & Bell, 1990; Meijer Drees, 1994; Wright et al., 1994). A detailed review of geological findings in the WCSB will be provided in chapter 2. As one of the largest reservoirs of fossil fuel resources in the world, thanks to the development of oil and natural gas industries, significant information has been gained pertaining to the regional- and local-scale subsurface structures beneath the WCSB. Tens of thousands of wells from regional exploration seismic surveys over the past 3 decades have provided relatively dense spatial sampling of the sedimentary rocks, offering first-order constraints on the sedimentary strata. Based on the existing reports, the sedimentary basin reaches a thickness of 5-6 km beneath the Rocky Mountains foothills and tapers eastward to the exposed Canadian Shield (Price, 1994; Wright et al., 1994). Owing to the multi-disciplinary researches on these samples and surveys (Wanless, 1970; Burwash & Culbert, 1976; Burwash et al., 1985; McGregor, 1986; Dods et al., 1989; Ross & Stephenson, 1989; Ross et al., 1989; Broome, 1990; Burwash & Power, 1991; Sweeney et al., 1991; Burwash et al., 1994; Ross et al., 1994), various stratigraphic layers have been refined and incorporated to an integrated model of the WCSB (Ross et al., 1991; Villeneuve et al., 1993; Wright et al., 1994; Branscombe et al., 2018).

Complementary to the active source surveys, passive seismic entail greater penetrating powers and are, therefore, able to resolve structures within and below the crust in western Canada (Hanssen, 2011; Chen et al., 2015; Tesoniero et al., 2015; Naghizadeh et al., 2022). Specific to the WCSB, a major breakthrough was made by the Alberta Basement Transects of Lithoprobe – a milestone trans-Canada geophysical experiment that targeted crustal structures and continental evolution (Clowes et al., 1995; Ross et al., 1995; Boerner et al., 2000; Ross et al., 2000; Clowes et al., 2002). A synopsis of the refraction/wide-angle reflection profiles shapes the present knowledge of the tectonic history of the WCSB (Eaton et al., 1999; Lemieux et al., 2000; Bouzidi et al., 2002), offering improved constraints to crustal domains in the northern (Peace River Arch Industry Seismic Experiment; Eaton et al., 1999; Ross & Eaton, 2002), central (Central Alberta Transect; Ross et al., 1995; Eaton & Cassidy, 1996; Bouzidi et al., 2002) and southern Alberta (Southern Alberta Lithospheric Transect; Eaton et al., 1999; Lemieux et al., 2000). Recent studies based on passive source surveys from newly deployed arrays, particularly the Canadian Rockies and Alberta

Network (CRANE; Gu et al., 2011), have revealed strong structural variations within and below the Precambrian crust that largely corroborated with the proposed tectonic framework (Bao & Eaton, 2015; Chen et al., 2015; Gu & Shen, 2015; Gu et al., 2015; Bao et al., 2016; Chen et al., 2017; Gu et al., 2017; Chen et al., 2018; Wu et al., 2019; Chen et al., 2020; Wang et al., 2020) and laid the groundwork for a more accurate, and higher resolution model of the tectothermal history surrounding the WCSB (Eaton et al., 1999; Ross et al., 2000; Bouzidi et al., 2002).

This dissertation aims to conduct high-resolution geophysical surveys of the sedimentary and upper crustal structures in the WCSB while taking advantage of nearly two decades (2001-2018) of data recorded from seven regional seismic networks. It focuses on the integrity and characteristics of the sedimentary structures and the Precambrian basement, thereby providing an updated appraisal of the existing sedimentary strata and the subsidence history of the Precambrian basement. The target of this thesis is secondary converted waveforms from receiver functions (RFs), which impose direct constraints on the impedance contrast, depth, and P-to-S velocity ratio of sedimentary and crustal interfaces. We process the RFs by introducing a novel nonlinear waveform inversion algorithm that matches the first 5 seconds of RFs, and the equivalent depth range (0-14 km) effectively bridges the gap between the vertical scales of reported well logs (0-6 km) and those of traditional broadband analysis (> 10 km) typical of receiver functions and surface waves.

1.2 Thesis outline

This dissertation focuses on imaging the subsurface structures of the WCSB within and below the sedimentary strata. It is organized as follows:

Chapter 2 provides a general overview of the geological and the geophysical background of the WCSB. This chapter focuses on a comprehensive literature review of the regional tectonics, evolution and lithology.

Chapter 3 summarizes the methodology, which consists of (1) the RF analysis and (2) the inversion algorithm. Part 1 details the pre-processing, seismic source equalization and two phase-equalization methods. In the second part, we introduce a non-linear inversion based on a genetic algorithm, to reduce the non-uniqueness and offer improved constraints of the subsurface structures.

Chapter 4* presents receiver function-based sedimentary structures and the Precambrian crystalline basement depths of the WCSB. The nature and locations of the basement invites discussions on the foreland basin formation during the billion-year-aged orogeny. Profiles of S-velocities refine the sedimentary structure of the Alberta Basin and provide updated information on the subsurface for future studies.

Chapter 5* focuses on the analysis of RF models in previous chapter. RF imaging shows a broad region of sedimentary Low Velocity Zones (LVZs) beneath southwestern Alberta Basin and along the Cordillera deformation front, which are subsequently linked to fossil fuel deposits embedded within the sedimentary strata. The analysis of anomalous shear wave velocity bodies from the upper to the middle crust of western Laurentia also reveals the locations of the LVZ and high velocity zone (HVZ). The geometries and scales of the LVZ and HVZ are consistent with the

proposed Precambrian evolution history of the WCSB. Reconstructed models based on inverted results of RFs offer further supports for the tectonic evolution history of the WCSB.

Chapter 6 summarizes the main findings of this thesis and briefly outlines future directions and improvements to the existing studies of the WCSB.

*Significant portions of Chapter 4 and Chapter 5 are now published in JGR-Solid Earth. [Zhang, C., Gu, Y. J., Dokht, R. M. H., & Chen, Y. (2023). Recovery of the Alberta Basin sedimentary structures in southern-central Alberta using nonlinear inversions of receiver functions.]

Chapter 2. Geological and geophysical background

The WCSB is predominantly located in southwestern Canada, spanning approximately 1.4 million square kilometres (MacKay & Pedersen, 2022) and covering Alberta, southwestern Manitoba, southern Saskatchewan, and northeastern British Columbia. This basin effectively marks the boundary zone between stable exposed Canadian Shield in the East and Northeast and much younger, and tectonically active, Canadian Cordillera (i.e. the Rocky Mountains; Figure 2.1). Due to major episodes of plate convergence in the past 3-billion years, which triggered both subduction and orogenesis (Price, 1994; Wright et al., 1994), the basement beneath the 600-million-year-aged sediments now consists of a network of 'terranes' with ages ranging from Precambrian to Quaternary. The following sections review the formation and characteristics of this basin on the basis of previous geological and geophysical studies.

Figure 2.1. Geographic location of the WCSB. The basin outline (red polygon) is obtained from Wright et al. (1994).

2.1 Foreland basin

A foreland basin is known as a structural basin that forms adjacent and parallel to a mountain belt. It is mechanically coupled to the adjacent orogen (Laubscher, 1978; Beaumont, 1981). In a foreland basin system, an elongate region of potential sediment accommodation forms on continental crust between a linear contractional orogenic belt and the adjacent stable craton, mainly in response to flexural subsidence that is driven by geodynamic processes related to subduction (Price, 1973; Dickinson, 1974; Dickinson & Suczek, 1979; Beaumont, 1981; Quinlan & Beaumont, 1984; Lyon-Caen & Molnar, 1985; DeCelles & Hertel, 1989; Crampton & Allen, 1995; Jordan, 1995; DeCelles and Giles, 1996; Figure 2.2a). This system comprises four discrete depozones – the wedge-top (Riba, 1976; Boyer & Elliott, 1982; Rankin et al., 1991; Lawton et al., 1993; DeCelles, 1994; Srivastava & Mitra, 1994; Coney et al., 1996), foredeep (Baltzer & Purser, 1990; Coakley & Watts, 1991; Sinclair & Allen, 1992; Sinha & Friend, 1994; Jordan, 1995), forebulge (Jacobi, 1981; Turcotte & Schubert, 1982; Patton & O'Connor, 1988; Coakley & Watts, 1991; Currie, 1994) and back-bulge (Bradley & Kusky, 1986; Flemings & Jordan, 1989; DeCelles & Burden, 1992; Reid & Dorobek, 1993; Holt & Stern, 1994; Giles & Dickinson, 1995) depozones (Figure 2.2b). The sediments resided therein depends on the location at the time of deposition rather than the ultimate geometric relationship with the fold-thrust belt (Jordan, 1981; Karner & Watts, 1983; Quinlan & Beaumont, 1984). The longitudinal dimension of the foreland basin system is roughly equal to the length of the adjacent fold-thrust belt (Figure 2.2a), excluding the masses of sediment that spill into remnant oceanic basins or continental rifts (Miall, 1981; Covey, 1986; Ingersoll et al., 1995; Sengor, 1995; DeCelles and Giles, 1996).

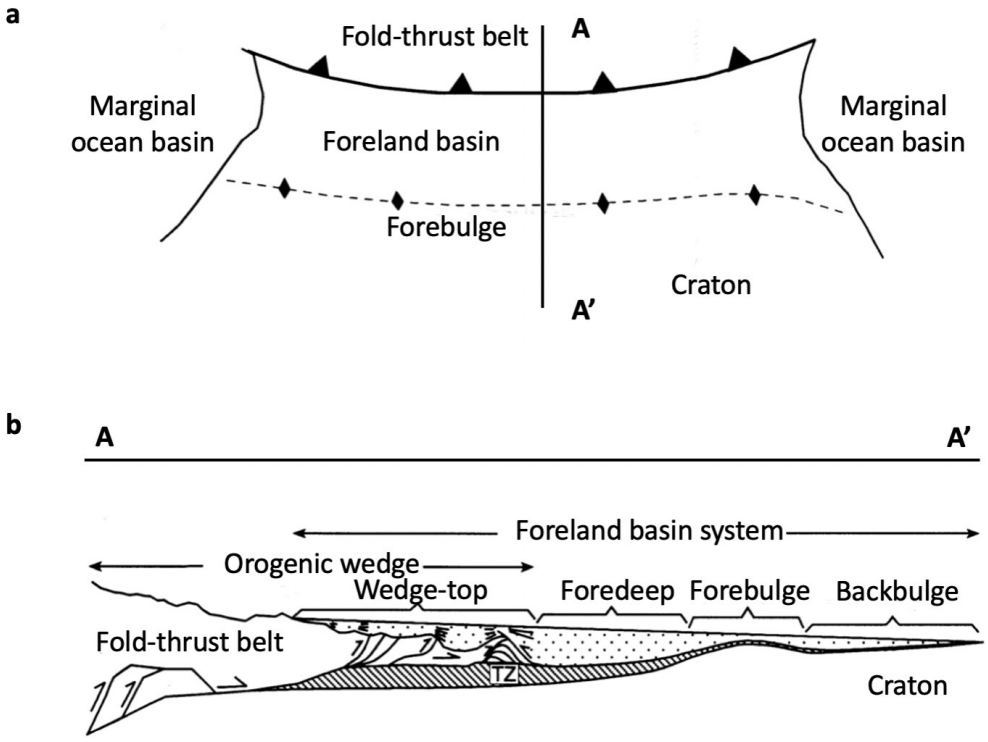

Figure 2.2. **a**. A schematic map of a foreland basin that forms between a pair of marginal ocean basins. The line AA' indicates a cross-section shown in part **b**. **b**. A schematic cross-section depicts the concept of the foreland basin system. The foreland basin is represented by the coarse stipple. TZ stands for a frontal triangle zone, represented by shade. Short lines with arrows indicate the progressive deformation in the orogenic wedge. Note the topographic load and basin fill load are applied on the fold-thrust belt and foreland basin, respectively. Modified from DeCelles and Giles, 1996.

According to a number of pioneering studies, foreland basins are divided into two types (Dewey & Bird, 1970; Dickinson, 1974, 1976; Beaumont, 1981; Catuneanu, 2004; Figure 2.3). One type is peripheral foreland basin or pro foreland basin (Beaumont, 1981; Jordan, 1981; Allen et al., 1986; DeCelles & Giles, 1996; Sinclair, 1997; Pfiffner et al., 2002), which results from the geodynamic process of the continent-island arc collision or continent-continent collision during the late orogen, where sediments are placed on the subducted or underthrust plate in front of the orogenic belt. A typical example is the Molasse Basin north of the Alps, which formed as the result of the flexure of the European plate during orogeny (Karner & Watts, 1983, Lyon-Caen & Molnar, 1989; Royden, 1993; Sinclair, 1997; Schlunegger & Mosar, 2011). The second type of foreland

basin is retro-arc foreland basin or retro foreland basin (Price, 1973; Dickinson, 1974; Laubscher, 1978; Beaumont, 1981; Jordan, 1981; Parcell & Williams, 2005), which is formed in response to subduction and underthrusting of a continental plate during continent-ocean convergence (Gurnis, 1992; Holt & Stern, 1994; Burgess et al., 1997). In this case, sediments are placed on the overriding plate inboard of continental-margin magmatic arcs and the associated thrust belts (Dewey & Bird, 1970; Beaumont, 1981; Catuneanu, 2004). The WCSB, which is the area of interest in this dissertation, is a typical retro-arc foreland basin (Wright, 1984; Wright et al., 1994).

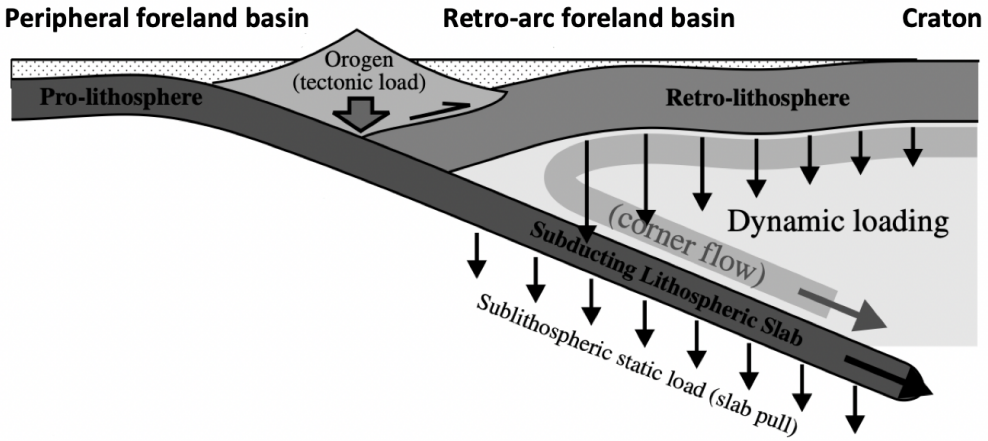

Figure 2.3. Peripheral and retro-arc foreland basin systems. The coarse stipple shade to the left of the orogen mark the peripheral foreland basin, whereas the coarse stipple shade to the right of the orogen shows the retro-arc foreland basin. This figure is modified from Catuneanu, 2004.

2.2 Western Canada Sedimentary Basin (WCSB)

The WCSB is a vast sedimentary wedge overlying the Precambrian crystalline basement of the western margin of the North American craton. The western edge of the WCSB is rich in exposed and deformed sediments originating near the ancestral North American margin between the Omineca and Intermontane Belts. In the East, the WCSB is bounded by the Phanerozoic edge of

the exposed craton, stretching from Tathlina high - a Precambrian arch in the Slave province (north) to Medicine Hat - Northern Montana (south). The sedimentary wedge begins with a thickness of over 7 km near the Rocky Mountain Foothills and thins toward the northeast, ultimately terminates at the eastern basin margin (Price & Fermor, 1984; Evenchick, 1991; Wright et al., 1994).

Major geological components of the WCSB are eastern Canadian Cordillera (Price, 1994) and two major sedimentary basins – the Alberta Basin and the Williston Basin – near the western margin of the ancestral North American craton (Gerhard et al., 1990; O'Connell & Bell, 1990; Meijer Drees, 1994; Wright et al., 1994; Figure 2.4). The Alberta Basin is a northwest trending trough in front of the Cordilleran Deformation Front and the fold-thrust belt, and extends eastward to the exposed Canadian Shield. The Williston Basin is an intracratonic sedimentary basin centered in North Dakota (Peterson & MacCary, 1987; Lefever et al., 1987), extending northward to southern Saskatchewan and southwestern Manitoba (Thomas, 1974; Kent & Christopher, 1994; Gerhard et al., 1990). These two basins are separated by a broad northeast-trending positive element that includes the Kevin-Sunburst Dome, Bow Island Arch and Sweetgrass Arch (Herbaly, 1974; Chistopher, 1990; Wright et al., 1994).

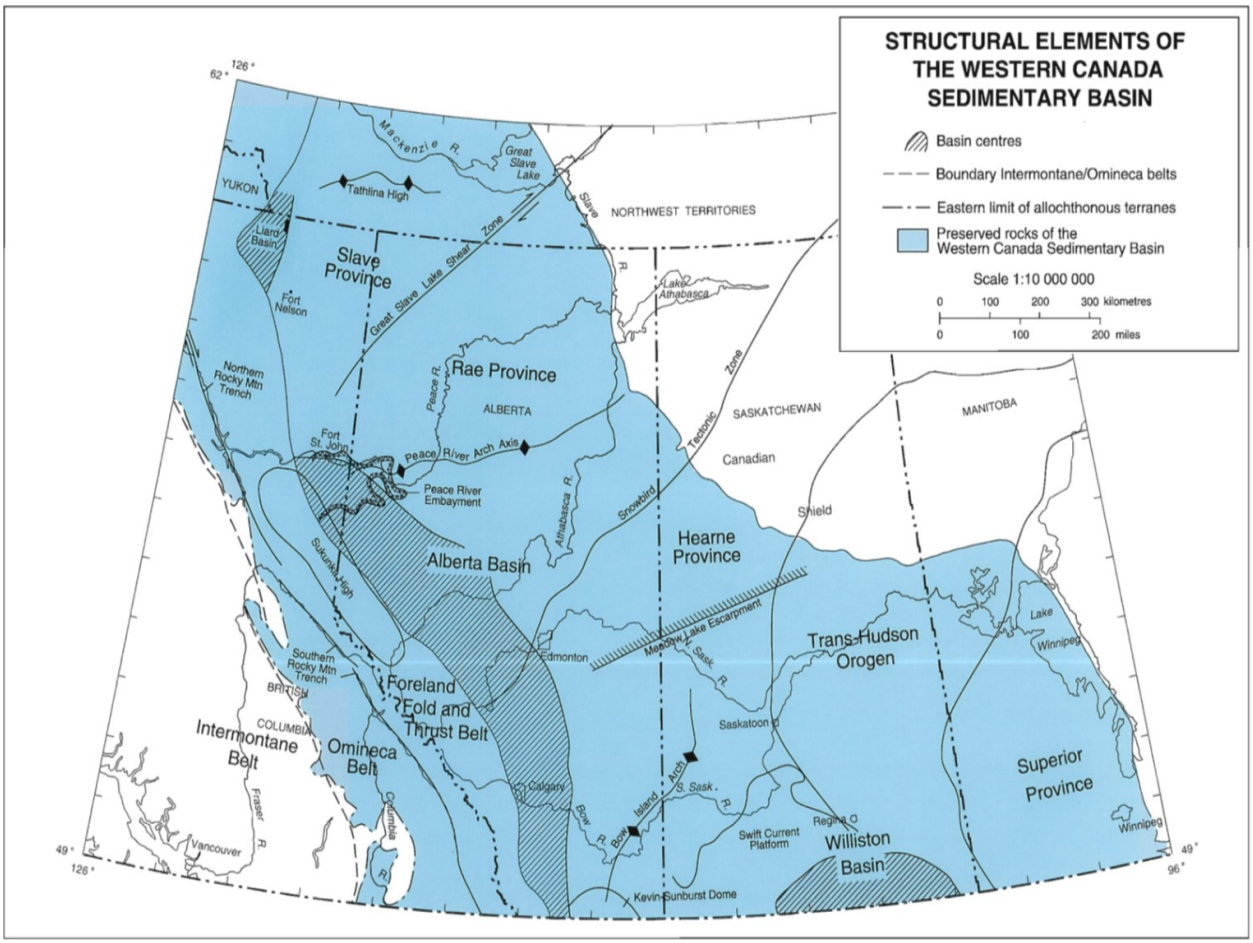

Figure 2.4. Structural elements of the WCSB (Wright et al., 1994). The blue area shows the outline of the WCSB. Depocenters of two major basins are labeled in dark shaded color.

2.2.1 The evolution of the WCSB

Beneath the sedimentary succession of the WCSB belies a crystalline basement at the western margin of the Canadian Shield (Burwash et al., 1994) that underwent more than two billion years of tectonic evolution. Two distinct stages during the formation of the WCSB have been interpreted from a profound change of clastic deposits preserved within the sedimentary wedge (Bally et al., 1966; Price & Mountjoy, 1970; Ewing, 1980; Price, 1994) during 1)late Proterozoic to late Jurassic miogeocline-platform stage (Stewart, 1972; Monger & Price, 1979) and 2) late Jurassic to early

Eocene foreland basin stage (Davis et al., 1978; Ewing, 1980; Price, 1994; Rohais et al., 2018; Figure 2.5).

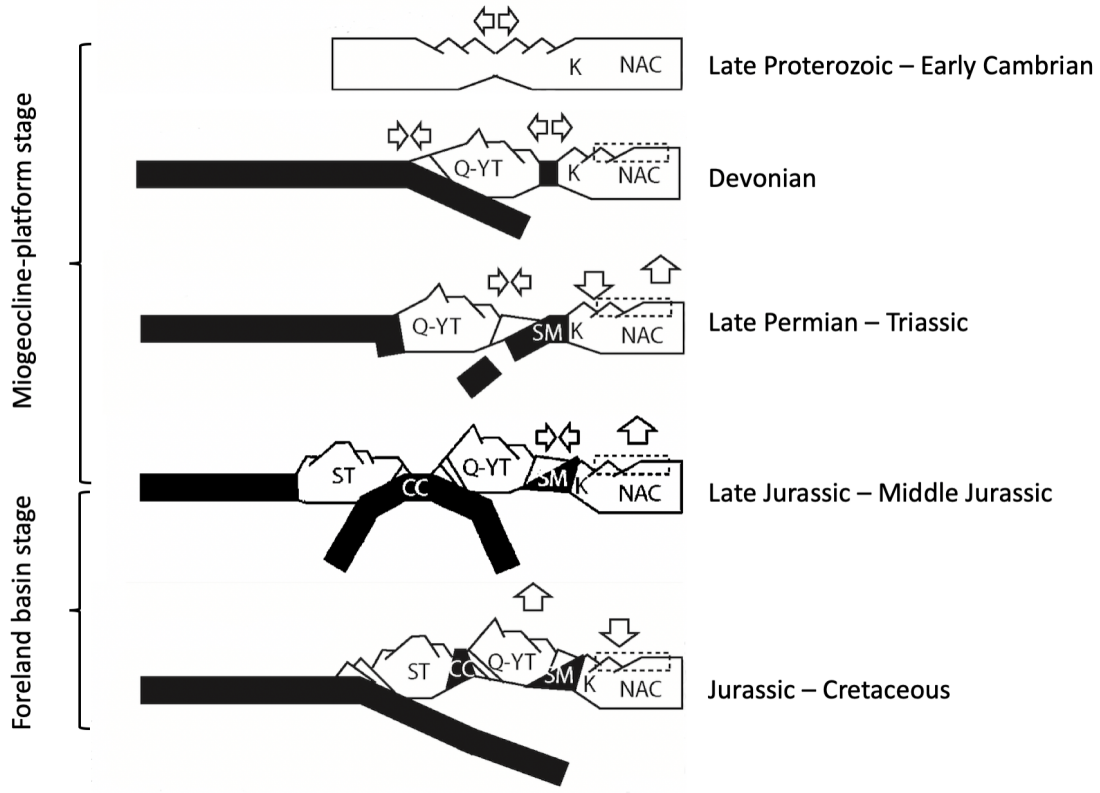

Figure 2.5. Discrete evolutionary history of the WCSB and the associated North American margin based on Rohais et al. (2018). The dashed rectangles denote the WCSB during each stage. The arrows indicate the main tectonic forces and their orientations reflect uplift, subsidence, extension, or compression. Abbreviations: CC, Cache Creek; K, Kootenay; NAC, North American Craton; Q-YT, Quesnellia and Yukon-Tanana; SM, Slide Mountain; ST, Stikinia. Modified from Rohais et al. (2018).

Paleozoic miogeocline-platformal stage

Driven by the tectonic process of continental rifting and drifting, an initial Cordilleran-continental margin was created between the North American craton and its adjacent ocean basin (Dewey &

Bird, 1970; Dickson, 1974; Beaumont, 1981). Subsequently, the miogeocline prograde outward from this passive continental margin (Stewart, 1972; Monger and Price, 1979). In the miogeoclinal-eugeoclinal couple, the main external source of sediments is from the craton in the northeast (Price, 1994).

Foreland basin stage

An accretion of allochthonous oceanic terranes driven by the subduction of the intervening oceanic lithosphere, as well as the closure of the intervening oceanic basins dominate the foreland basin stage of the tectonic evolution of the WCSB (Davis et al., 1978; Monger and Price, 1979, Price, 1994). As a consequence of the oblique collision between the accreted oceanic terranes and the North American craton (Dewey & Bird, 1970; Dickson, 1974), the outboard part of the miogeocline-platform component of the miogeocline was detached from its basement and displaced to the northeast. This part experienced compression and thickening during the tectonic process, from which the increasing weight induced the subsidence of the foreland basin (Price, 1973; Beaumont, 1981). The uplift and erosion associated with the subsidence process provided most of the sediment deposited in the foreland basin (Price, 1973; Beaumont, 1981; Cant and Stockmal, 1989). As the orogeny continued, older deposits of the foreland basin were detached from the basement, and then attached to the accreted terranes formed by oblique collisions between the oceanic terranes and the North American craton. Much of the older-aged deposit was uplifted and eventually eroded to younger deposits for the foreland basin. This pattern of tectonic evolution results in the fold-and-thrust belt along the Rocky Mountains. Crustal extension in the central part of the Cordillera (i.e. the present-day Cordillera-Craton transition) during the episode of the Early and Middle Eocene marks the termination of the whole foreland basin stage (Price, 1979; Ewing, 1980; Price, 1986).

2.2.2 Phanerozoic overview

The Phanerozoic evolution of the WCSB was dominated by post-Jurassic convergence along the western margin of the North American craton, and was eventually terminated by the Mesozoic-Cenozoic Cordilleran orogeny that shaped the entire western coast of the North America (Wright et al., 1994; Ricketts, 2008; Chen, 2018). The development of the foreland basin has been correlated with the oblique collision between the Cordilleran terranes and North American craton (Price, 1973; Beaumont, 1981; Cant & Stockmal, 1989). Driven by the subsidence induced by the load of easterly fold-thrust belt, the largest depocenter – the Alberta basin, was formed in front of the Cordilleran Deformation Front (CDF). Deposits in the sedimentary basin are derived from Paleozoic miogeosyncline-platform sequences to Mesozoic-Cenozoic eroded clastic debris from the accreted terranes, indicating the distinct evolution stages of the WCSB from the Early Paleozoic rifted margin to the foreland region of the Cordillera orogen (Davis et al., 1978; Porter et al., 1982; Price, 1994).

The foreland belt (i.e. fold-and-thrust belt), adjacent to the Alberta basin, comprises the easternmost Cordillera. The decollement folding and the east-verging thrust faulting within the eastern-tapering wedge of supracrustal rocks indicates this belt has recorded some of the most intense deformations of the WCSB during the orogeny (Price, 1986). The subsurface structures of the WCSB are mainly constrained by a few deep seismic reflection and refraction lines as well as a significant number of well-logs. The seismic observations from these profiles, in combination with geological information from multi-disciplinary studies involving stratigraphy, petrology, geochronology and geochemistry (Wanless, 1970; Burwash & Culbert, 1976; Burwash et al., 1985; McGregor, 1986; Dods et al., 1989; Ross & Stephenson, 1989; Ross et al., 1989; Broome, 1990; Burwash & Power, 1991; Sweeney et al., 1991; Burwash et al., 1994; Ross et al., 1994), offer first-order sedimentary constraints and evolving crustal/lithosphere models of the WCSB (Ross et al., 1991; Villeneuve et al., 1993; Wright et al., 1994; Branscombe et al., 2018).

2.2.3 Precambrian overview

The Precambrian crystalline basement marks the boundary between the sedimentary basin and the upper crust. The Precambrian domains, which are integral parts of the western margin of the Laurentia, formed in the early Proterozoic from 2.0 to 1.8 Ga (Hoffman, 1988; Hoffman, 1989). Basement lithology shows that the types of most rocks are quartzo-feldspathic gneiss, granitoids, granulites and retrogranulites, metasedimentary rocks, mylonites, and amphibolites (Burwash and Culbert, 1976; Burwash and Power, 1991; Chacko et al., 2000). Although the abundance of rock types varies spatially, it is difficult to constrain the boundaries between terranes on this basis as high grade metamorphic and/or deep-seated igneous rocks are dominant in all areas (Burwash et al., 1994). Thanks to the aeromagnetic data and isotropic analyses of drill-core samples, various constraints on the subdivision of the crystalline basement suggest more than 20 distinctive Precambrian crustal domains (Figure 2.6). A number of seminal studies of the Precambrian domains, especially those associated with LITHOPROBE (Boerner et al., 2000; Ross et al., 2000; Clowes et al., 2002), shaped the current view of the tectonic evolution and supracrustal structures of the WCSB (Hoffman, 1988; Ross et al.,1991; Villeneuve et al., 1993; Ross et al., 1995; Eaton et al., 1999; Boerner et al., 2000; Ross et al., 2000; Ross & Eaton, 2002; Dickinson, 2004; Heaman et al., 2004; Welford & Clowes, 2006).

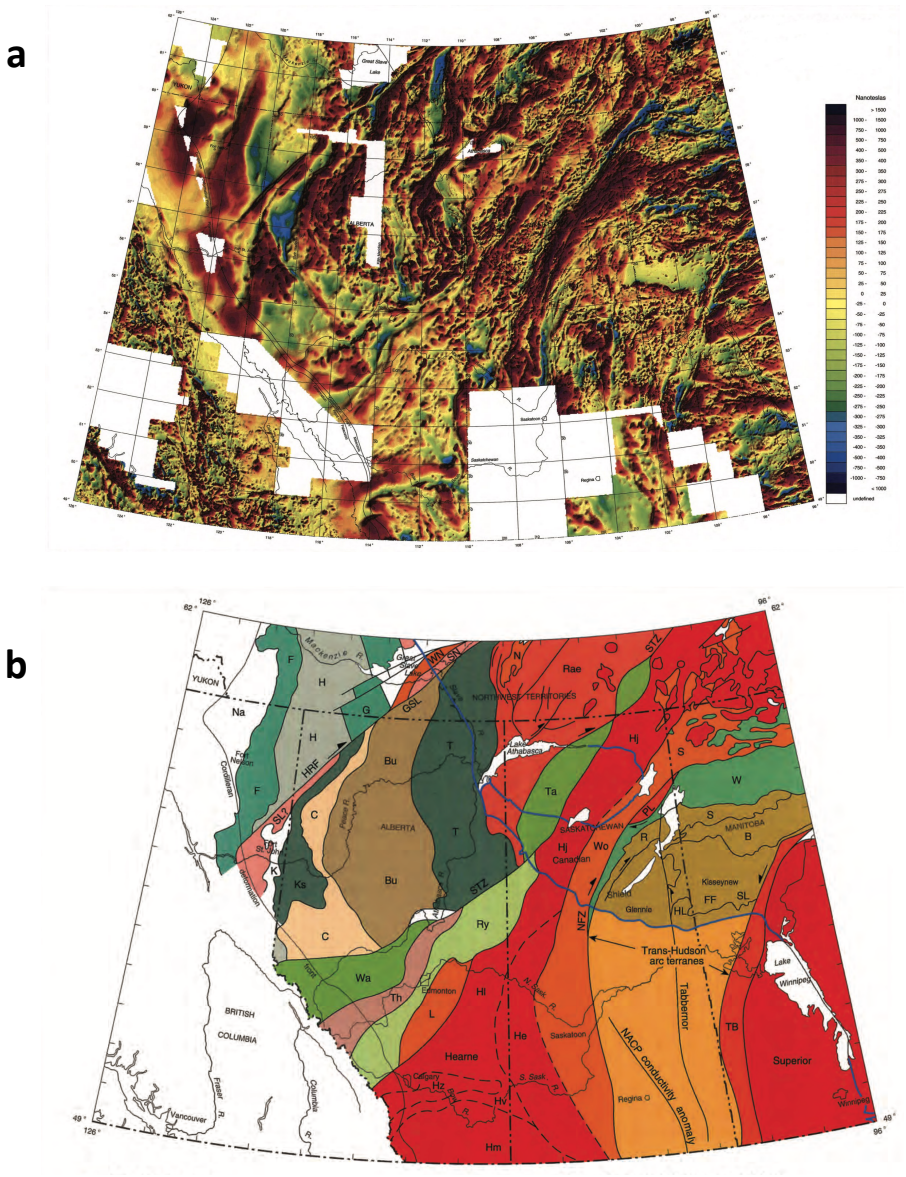

Figure 2.6. **a**. Aeromagnetic anomaly map of the western Canada (Ross et al., 1994). **b**. Tectonic domains of the Precambrian basement of the WCSB (Ross et al., 1994). Dark blue line marks the edge of platform cover. Abbreviations: B, Baldock; Bu, Buffalo Head; C, Chinchaga; F, Fort Simpson; FF, Flin Flon; G, Great Bear; GSL, Great Slave Lake Shear Zone; H, Hottah; HL, Hanson Lake; HRF, Hay River Fault; He, Eyehill High; Hj, Mudjatik Domain; Hl, Loverna Block; Hm, Medicine Hat Block; Hv, Vulcan Low; Hz, Matzhiwin High; K, Kiskatinaw Domain; Ks, Ksituan; L, Lacombe Domain; N, Nonacho; NFZ, Needle Falls Shear Zone; Na, Nahanni Terrane; PL, Peter Lake Domain; R, Reindeer; Ry, Rimbey; S, Snake Indian; SL, Snow Lake; SN, Simpson Island Terrane; STZ, Snowbird Tectonic Zone; T, Taltson; TB, Thompson Belt; Ta, Tantato; Th, Thorsby; W, Wathamun-Chipewyan; WN, Wilson Island Terrane; Wa, Wabamun; Wo, Wollaston.

2.2.4 Alberta Basin

The Alberta Basin is vast sedimentary wedge superimposed on the Precambrian crystalline basement of the western North American Craton. As a key constituent of the WCSB, the Alberta Basin initiate at the CDF to the west, stretches southeastward to the Bow River Arch, and eventually reaches its northern boundary at the Tathlina High (Wright et al., 1994). The Alberta Basin features the Peace River Arch and the West Alberta Ridge, two major topographic highs formed at the time of Cambrian (Meijer Drees, 1994). As one of the world's largest reservoirs of fossil fuels, the deposition age of the Alberta Basin ranges from Cambrian (540 Ma) to Quaternary (2.6 Ma – present). Owing to a prolonged history of well-drilling and exploration seismic surveys, the spatial sampling of the sedimentary rocks offers first-order constraints on the sedimentary strata beneath the Alberta Basin (Ross et al., 1991; Villeneuve et al., 1993; Wright et al., 1994; Boerner et al., 2000; Lemieux et al., 2000; Clowes et al., 2002; Branscombe et al., 2018). Based on pioneering studies in the 20th century (Price, 1973; Price and Fermor, 1984; Wright, 1984; Kent, 1987; Sloss, 1988; Evenchick,1991; Burwash et al., 1994; Ross et al., 1994; Wright et al., 1994), the sedimentary wedge reaches a maximum thickness of 5-6 km beneath the foothill of Rocky Mountains and narrows eastward towards the exposed Canadian Shield.

Beneath the sedimentary succession of the WCSB belies a crystalline basement at the western margin of the Canadian Shield (Burwash et al., 1994) that underwent more than three billion years of tectonic evolution. Early knowledge of the Alberta basin structure and history benefited from petrography, as well as geochemical and isotropic aging analyses (Burwash & Krupicka, 1969, 1970; Wanless, 1970; Burwash & Culbert, 1976; Collerson et al., 1988; McGregor et al., 1990) of drill core samples from a number of exploratory wells. Since the early 1990s (Ross et al., 1991, 1994), a series of regional aeromagnetic, gravity and seismic surveys (Eaton et al., 1999; Welford & Clowes, 2006; Clowes, 2010) provided unprecedented opportunities to systematically explore the crust beneath the WCSB. A complex network of basement domains (known as terranes) was proposed (Ross et al., 1991), which laid the groundwork for an improved understanding of the overall tectonic framework in the cratonic crystalline basement. A recent study conducted by

Alberta Geological Survey (AGS) on sedimentary strata sheds new light on the Precambrian basement by interpolating between wellbore logging information (Branscombe et al., 2018).

2.3 Motivation

Scores of researches are deployed in the WCSB to reveal the local tectonics and evolutions, which is an important part of the global tectonics and evolution history. Previous studies have applied RFs for imaging the Moho (Wolbern et al., 2009; Gilbert, 2012; Schmandt et al., 2015, Chen et al., 2015; Song et al., 2017; Zhang et al., 2019), mid-lithospheric discontinuities (Abt et al., 2010; Hopper & Fischer, 2015; Selway et al., 2015; Chen et al., 2018; Krueger et al., 2021), Lithosphere-Asthenosphere boundary (Li et al., 2007; Kind et al., 2012; Lekic & Fischer, 2014; Olugboji et al., 2016; Liu & Gao, 2018; Liu et al., 2021), and mantle transition zone interfaces (Gurrola & Minster, 1998; Li et al., 2000; Lawrence & Shearer, 2006; Chen & Ai, 2009; Gao & Liu, 2014; Gu et al., 2015; Agius et al., 2017; Duan et al., 2017). But limited applications of RFs are performed at the depth level of the sediments. Because of the low resolution of CRUST 1.0 model and the depth limitation of models built through well-logging and seismic exploration from Alberta Geological Survey (AGS), I propose that a new shear wave velocity model of the sedimentary and upper crustal structures of WCSB with finer resolution can provide a more detailed information on the sedimentary strata beneath the WCSB. Regardless of the depth limitation and potential defects of sonic waves in well-logging, this regional-scale model derived from the nonlinear-inversion-based receiver function analysis on high-quality datasets sheds new light on the tectonic structures and subsidence history of the WCSB.

Chapter 3. Methodology

Passive seismic imaging techniques are the core method of this project. Unlike the active seismic imaging techniques, passive seismic imaging from recorded source induced by global earthquakes has the advantage of broader data coverage and greater penetrating power, offering improved sensitive to the subsurface impedance contrast, depth, and P-to-S velocity ratio. With the help of inversion procedures, we construct the velocity models for the WCSB. The following sections give the details of the methodology in this dissertation.

3.1 Receiver function method

3.1.1 Overview

In general, receiver functions (RF) are time series computed from three-component seismograms (Ammon, 1991). The waveform is a composite of the P-to-S converted seismic waves generated at the subsurface impedance interfaces beneath the seismometer. The two-component seismogram, comprising the radial and the vertical components, provides a lot of information about properties under Earth, especially the velocity discontinuities which can be indicated directly by the P-to-S converted phases (Burdick & Langston, 1977). After removing the source time function and instruments responses from the radial component (i.e. deconvolution, Langston, 1979), we get the receiver functions as the source equalized radial component seismograms (Figure 3.1).

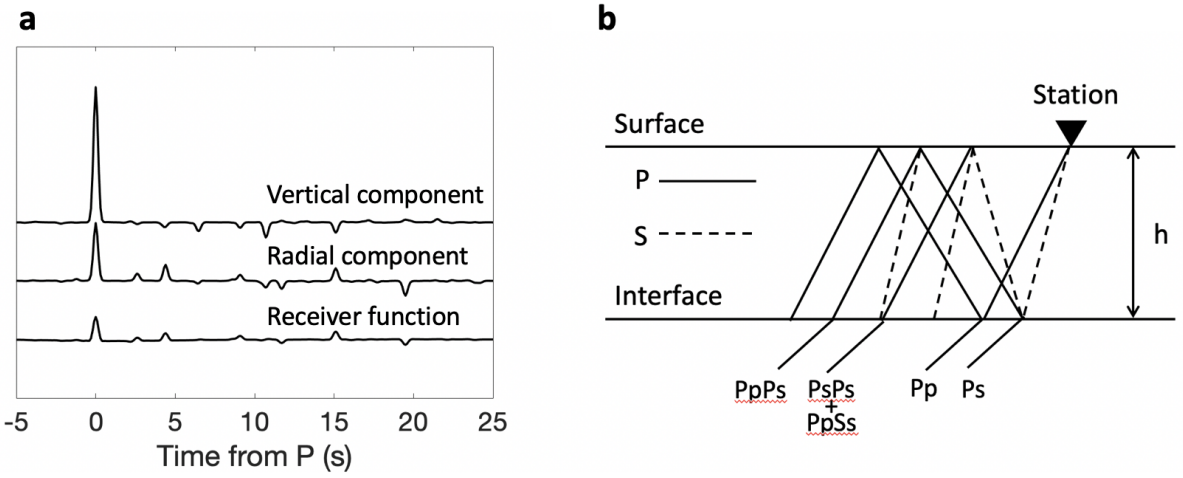

Figure 3.1. **a**. A schematic diagram of a receiver function and the corresponding vertical and radial components. **b**. Ray paths of converted waves between the surface and the given interface (e.g. basement or Moho).

The high sensitivity of RF to subsurface discontinuities makes it an effective tool to image the Moho (Zhu & Kanamori, 2000; Gilbert, 2012; Schmandt et al., 2015), crustal LVZ in tectonically

active orogens (Zandt et al., 1994; Kind et al., 1996; Beck & Zandt, 2002), craton structure (James et al., 2003), mid-lithospheric discontinuities (Abt et al., 2010; Hopper & Fischer, 2015; Chen et al., 2018), lithosphere-asthenosphere boundary (LAB; Lekic & Fischer, 2014; Liu & Gao, 2018), and mantle transition zone (Bostock, 1996; Li et al., 1998; Li et al., 2000; Lawrence & Shearer, 2006; Chen & Ai, 2009; Gao & Liu, 2014; Gu et al., 2015). A typical RF analysis consists of (1) the observation organization, also known as data pre-processing, which examines variations in incident-wave azimuth (a function of source back azimuth) and incident-wave angle (a function of source distance and depth), (2) isolation of the receiver response, also known as source equalization, which derives RFs after equalizing near-source effects, (3) stacking, which is used to improve the signal-to-noise ratio (SNR), (4) forward modeling or inversion, which simulates the receiver function based on a given model or recovers a model on the basis of recorded observations, and (5) solution optimization.

3.1.2 Data pre-processing

Data pre-processing is based on the idea that the seismic signals need to be organized into clusters by the distance and azimuth of appropriate sources (Ammon, 1991). Because of (1) the steep incidence angle of the seismic waves, (2) the lack of mantle triplications and the PcP converted phases, and (3) the planar incident P-wave beneath the regional array, only teleseismic events with source-receiver distances of 30 and 90 degrees (which are ~3000-10000 km) are ideal for RF analysis (Rondenay, 2009). In this thesis, the dataset consists of over 80 regional broadband seismic stations from 7 seismic networks in southern-central Alberta (Figure 3.2), recording earthquakes from 2001 to 2018. After the removal of the instrument responses and gains, we rotate the original N-to-S, E-to-W, and the vertical component seismograms to radial, transverse and vertical oriented components using the matrix transformation equation:

$$\begin{bmatrix} R \\ T \\ Z \end{bmatrix} = \begin{bmatrix} -cos\theta & -sin\theta & 0 \\ sin\theta & -cos\theta & 0 \\ 0 & 0 & 1 \end{bmatrix} \begin{bmatrix} N \\ E \\ Z \end{bmatrix}, \tag{3.1}$$

where θ is the back azimuth, which is a projection of the azimuth from the origin to the opposite side of the azimuth circle, and N, E, and Z represent the original N-S, E-W, and vertical components. Subsequently, the data are bandpass filtered by a Butterworth bandpass filter to remove incoherent noise at low and high frequencies. The filtered observations are usually tapered at 30 seconds prior, and 120 seconds after, the predicted direct P-wave arrival time based on PREM (Dziewonski & Anderson, 1981). The pre-processed vertical and radial components seismogram can be expressed by the time series according to the following equations:

$$\begin{matrix} Z(t) = \sum_{!}^{"} \#_{\$}\, z_{!} s(t - t_{!}) \\ R(t) = \sum_{!}^{"} \#_{\$}\, r_{!} \; s(t - t_{!}) \end{matrix} \quad , \tag{3.2}$$

where *s(t)* is the source time function; *k* is the *k*-th ray recorded signal; z_k and r_k represent the amplitudes of the *k*-th ray on the vertical and radial components, respectively; t_k represents the corresponding arrival time.

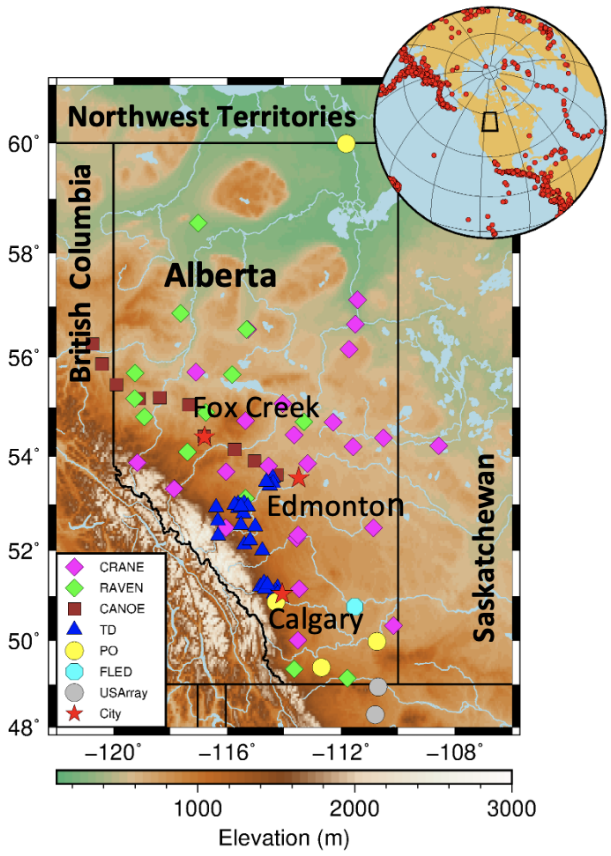

Figure 3.2. The distribution of regional seismic stations from 7 seismic networks (i.e. CRANE, RAVEN, CANOE, TD, PO, FLED, and USArray) examined in this dissertation. The inset global map shows all earthquake events (red dots) analyzed in this study. The study region is marked by black polygon on the globe.

3.1.3 Source equalization

P-to-S conversions occur at impedance contrasts, and their presence are therefore important in revealing the subsurface strata (Aki & Richards, 2002). Due to the near vertical incidence angles of seismic waves, Ps phases are normally recorded on radial component seismograms. However, the energy of direct P phase and other reverberations is projected onto both vertical and radial components (Figure 3.1a) as they have similar orientations. Hence, the removal of the vertical

component from the corresponding radial component seismogram can preferentially emphasize the P-to-S converted waves recorded on the radial component, and thus offering greater clarity on the amplitude and timing of the converted waves. This step is typically conducted by deconvolving the vertical response from the radial response (Ammon, 1991). The removal of the source term procedure, known as the source equalization, can further improves the coherency of the scattered wave energy (Langston, 1979). Deconvolving in the frequency domain yields

$$H(\omega) = \frac{R(\omega)Z(\omega)}{Z(\omega)Z(\omega)} = \frac{R(\omega)}{Z(\omega)} \quad , \tag{3.3}$$

where $H(\omega)$ is the Fourier transform of the RF; the term $S(\omega)$ is the frequency spectrum of the source time function $s(t)$ in Equation (3.2); $R(\omega)$ and $Z(\omega)$ are the frequency spectra of the radial and vertical components, respectively. The expansion equations of $R(\omega)$ and $Z(\omega)$ are

$$\begin{aligned} R(\omega) &= r_0 \sum_{k=0}^{n} r_k \, e^{+i\omega t_k} \\ Z(\omega) &= z_0 \sum_{k=0}^{n} z_k e^{+i\omega t_k} \end{aligned} \quad , \tag{3.4}$$

where r_0 and z_0 represent the amplitudes of the direct P wave on the radial and vertical components, respectively; r_k represents the amplitude of the k-th arrival normalized by the amplitude of the direct P wave on the radial component, and z_k is the vertical component equivalent amplitude term with the following expressions:

$$\begin{aligned} r_k &= r_k / r_0 \\ z_k &= z_k / z_0 \end{aligned} \quad . \tag{3.5}$$

Focusing on the sizable energy of the first three arrivals (direct P phase, Ps phase, and PpPdp phase), Equation (3.3) can be rewritten as

$$H(\omega) = \frac{.''}{/''}\frac{01.\#3^{\$\%\&'\#1.(3^{\$\%\&'(}}{01/\#3^{\$\%\&'\#1/(3^{\$\%\&'(}} \quad . \tag{3.6}$$

According to the data selection criteria, Equation (3.6) can be simplified in view that (1) the incidence of P wave is a plan wave approximately equalizes r_p and z_p; (2) the incidence angles of P waves between 30 and 90 degrees are steep, which means that z_s is much smaller than 1 and $z_4 e^{+,'-(}$ is therefore neglectable. Because z_p is normally smaller than 1/2, we can expand Equation (3.6) using Taylor series and neglect the higher order terms. The RF in frequency domain can be eventually simplified as

$$H(\omega) = \frac{.''}{/''}(1 + r_4 e^{+,'-(}) \quad . \tag{3.7}$$

Through inverse Fourier transform, we are able to retrieve raw RFs in time domain. It is essentially a scaled version of the recorded radial component at the removal of the P wave multiples (Ammon, 1991).

To further improve the quality of RF, the Gaussian filter and(or) water-level deconvolution are(is) applied in source equalization. The Gaussian filter is a low-pass filter aimed to remove high frequency noise in observed signals. It has the advantages of simple shape, zero phase distortion, and lack of side-lobes (Langston,1979). The term water-level (or water-level parameter) is a fraction multiplied by the maximum denominator amplitude in the deconvolution process, which acts as a threshold to determine the minimum amplitude allowed in the denominator for the stability of spectral division outlined in Equation (3.3) (Clayton & Wiggins, 1976). With water-level and Gaussian filter in the source equalization, the RF in frequency domain can be given as

$$H(\omega) = \frac{\%(')**(')}{567\{*(')**('),:\cdot 567[*(')**(')]\}} G(\omega) \quad , \tag{3.8}$$

where c is the water-level parameter; symbol '*' represents the complex conjugate; $G(\omega)$ is the function of the Gaussian filter as

$$G(\omega) = e^{+(\frac{\omega}{2\alpha})^2} \quad , \tag{3.9}$$

where α is the Gaussian parameter (or Gaussian factor) that controls the frequency content of the filter. In this thesis, Gaussian factors of 2.5 and 5.0 are used to acquire the low-frequency and high-frequency RFs.

3.1.4 Stacking

Stacking is an important procedure to improve the SNR of individual RFs (Owens et al., 1984). Two commonly adopted practices are Common Conversion Point (CCP) stacking and station-based stacking. CCP stacking is based on the assumption that the receiver functions are composed solely of P-to-S conversions at velocity boundaries, while station-based stacking is simply adding up the receiver functions recorded by a single station. Choices between these two methods largely depend on the relationship between the station spacing and the station aperture. The lateral sampling distance is approximately the one third of the depth to the subsurface interface (Landes et al, 2006), and generally ranges from 0.4 to 0.7 times the thickness between the surface and the interface depending on frequencies and underground structures (Cassidy, 1992). Due to this criterion, resolution of CCP stacking increases along the depth. In other word, the CCP stacking provides higher lateral resolution than station-based stacking for relatively deep interfaces (Dueker & Sheehan, 1997). Unfortunately, the target structure of this thesis (< 15 km) and the relatively large station spacing (~90 km) are unable to satisfy the requirements of CCP-based stacking. Therefore, the station-based stacking will be the main focus of our study.

We manually select more than 14,000 high-quality RFs for the subsequent processing, with an approximately 100 RFs retained at each station. After stacking, noises are obviously depressed, offering much clearer converted waves on seismogram (Figure 3.3).

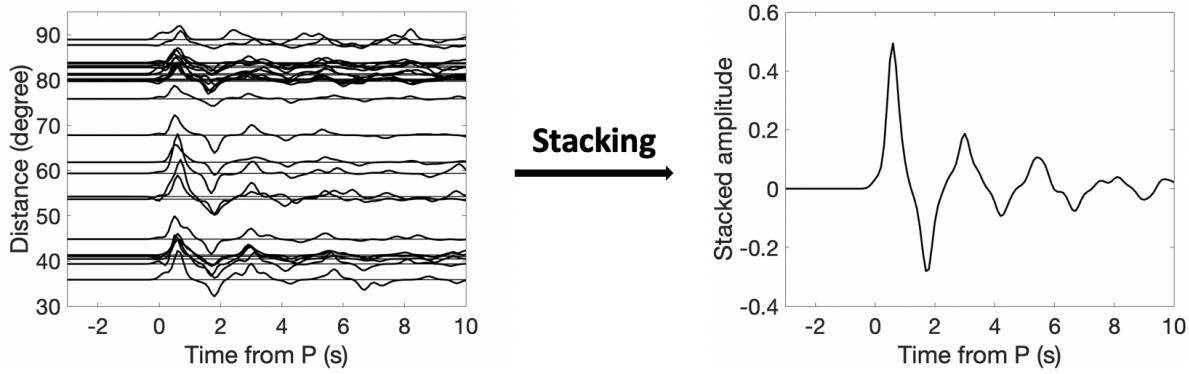

Figure 3.3. An example of station-based stacking performed on recorded RFs from the Station DOR.

To further constrain the boundary between the sedimentary strata and the Precambrian crystalline basement, we introduce a modified *H-κ* stacking. The *H-κ* stacking algorithm was first introduced by Zhu and Kanamori (2000) to solve the problem in delineating the Moho interface. This stacking performs a grid search for the most energetic stack of the direct Ps phase and the later multiple converted phases (the clear and comparable PpPs and PpSs+PsPs phases) on the basis of predicted delays relative to the direct P phase (Zhu and Kanamori, 2000; Yeck et al., 2013). The stability and flexibility of this approach is further improved by Gu et al. (2018) through a ray tracing-based approach (Niu et al., 2007) and a multilayer global crustal model - CRUST 1.0 (Laske et al., 2013; Pasyanos et al., 2014). In theory, the arrival time of Ps phase and the multiples are calculated by

$$t_{?4} = \int_{/\#\$}^{/\#C} \mathrm{AB}\overline{\frac{0}{@(/)^{*}} - p^{\mathrm{A}}} - \mathrm{B}\overline{\frac{0}{[\mathrm{B}(/)@(/)]^{*}} - p^{\mathrm{A}}}\mathrm{D}\, dz \ , \tag{3.10}$$

$$t_{?\mathrm{D}?4} = \int_{/\#\$}^{/\#C} \mathrm{AB}\overline{\frac{0}{@(/)^{*}} - p^{\mathrm{A}}} + \mathrm{B}\overline{\frac{0}{[\mathrm{B}(/)@(/)]^{*}} - p^{\mathrm{A}}}_{\mathrm{D}} dz \ , \tag{3.11}$$

$$t_{?\mathrm{D})41?4?4} = \int_{/\#\$}^{/\#C} \mathrm{A2B}\overline{\frac{0}{@(/)^{*}} - p^{\mathrm{A}}}_{\mathrm{D}} dz \ , \tag{3.12}$$

where p is the ray parameter of the incident wave; H is the presumed thickness between the surface and the interface; z represents the depth; $V_s(z)$ is a function of the shear wave velocity and the depth; $\kappa(z)$ is a function of the V_p/V_s ratio and the depth. Because of the relatively low SNR of individual RF, one can use multiple events to stack their RFs based on this algorithm (Equation (3.10) – (3.12)), which is the so-called H-κ stacking. With a pair of given values of H and κ (V_p/V_s ratio), the stacked amplitude of Ps, PpPs, and PpSS+PsPs phases is calculated as a weighted sum

$$A(H,\kappa) = w_0 r(t_{?4}) + w_{\mathrm{A}} r\mathrm{K}t_{?\mathrm{D}?4}\mathrm{L} + w_{\mathrm{E}} r(t_{?\mathrm{D})41?4?4}) \ , \tag{3.13}$$

$$\sum w_{,} = w_0 + w_{\mathrm{A}} + w_{\mathrm{E}} = 1 \ , \tag{3.14}$$

where A represents the stacked amplitude, $r(t)$ is the amplitude of the radial RF; t_{Ps}, t_{PpPs}, and $t_{PpSs+PsPs}$ are the predicted arrival times using Equation (3.10) – (3.12), and w_i are weighting factors. $A(H,\kappa)$ reaches a maximum value when all three phases are stacked coherently with the optimal thickness (H) and V_p/V_s ratio (κ) (Figure 3.4c and 3.4d). Theoretically, P-to-S conversion occurs at the Precambrian basement is similar with that occurs at the Moho, so H-κ stacking can be equally effective in mapping the lateral variation of Precambrian basement depth under WCSB. For examples, basement depths beneath station TD005 and station TD006 calculated from H-κ stacking (Figure 3.4) are consistent with those from the Alberta Geological Survey (AGS) based on well-logs (Branscombe et al., 2018).

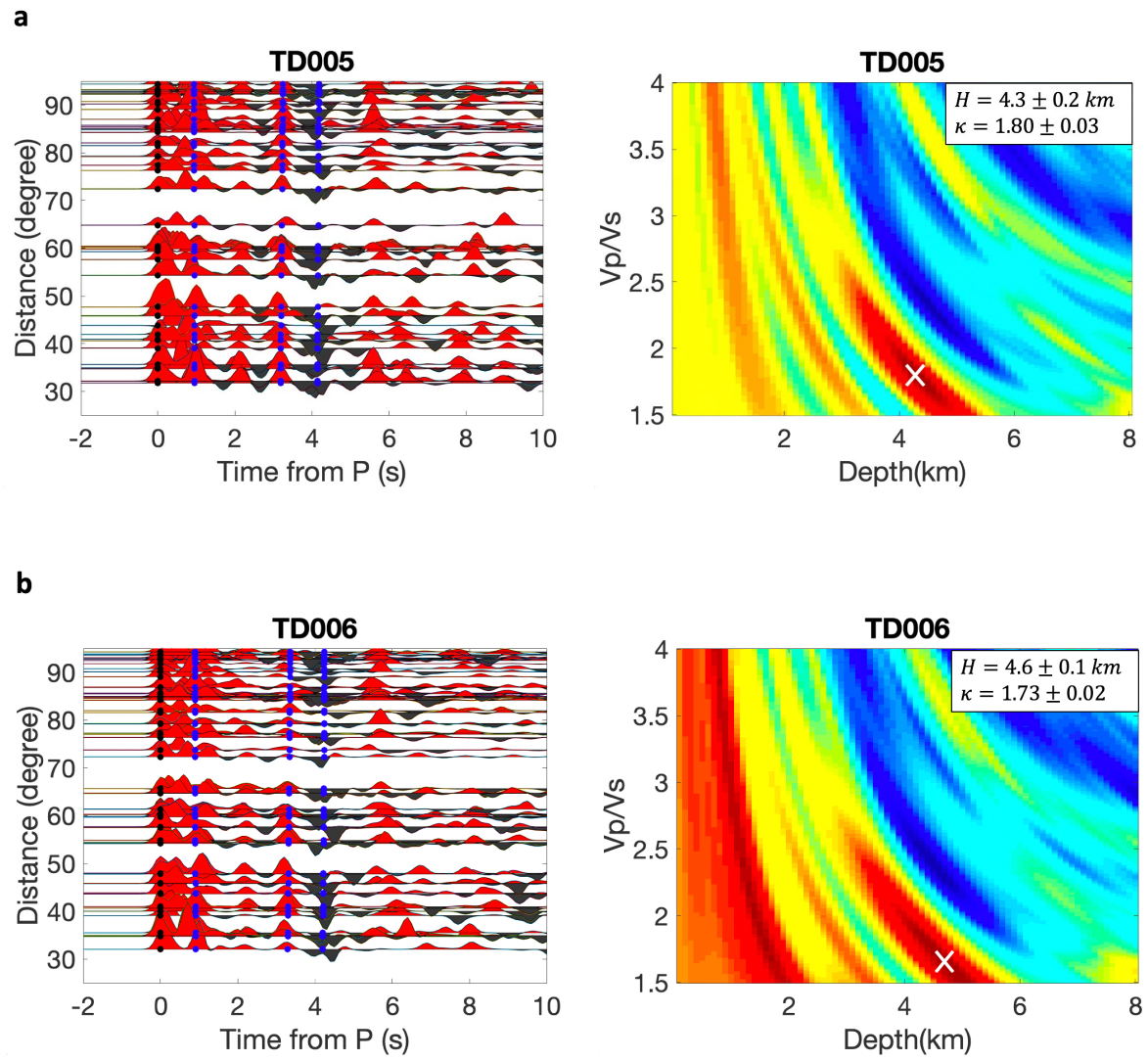

Figure 3.4. **a**. The RFs (left) and *H-κ* stacking (right) diagrams of station TD005. Blue dash lines mark the predicted arrival times of converted phases (0p1s, 2p1s, and 1p2s) from *H-κ* analysis. White cross marks the maximum stacking amplitude. **b**. Same as **a** but for station TD006.

The V_p/V_s ratio shows a relationship between lithology and the distribution of pore and crack shapes (Tatham, 1982). Well-logging data shows that in sedimentary basin the variation of V_p/V_s ratio rangs from 1.7 at deep part to nearly 5 at the surface, but mostly around 2.0, and the ratio decreases along the depth (Tobon, 2012). CRUST 1.0 gives the Poisson's ratio between 1.74 and

1.78, which is an average approximation for the real sedimentary and crustal values. Therefore, V_p/V_s ratio from H-κ analysis is consistent with the data from previous studies.

3.2 Inversion algorithm

Waveform stacking provides a pseudo two-dimensional profile that reflects the depth and geometry of subsurface interfaces. In this thesis, we introduce a RF waveform inversion method to obtain more accurate projections of structural characteristics. The core of the waveform inversion is to translate the information contained in the RFs into a simplified model of the subsurface structures (Ammon et al., 1990). Linear RF inversion in time domain was first introduced by Owens et al. (1984). Further study by Ammon et al. (1990) provided an improved linear RF inversion method and, at the same time, addressed the non-uniqueness of RF inversions due to the velocity-depth trade-offs. The forward problem of the seismic waveform may be described by

$$\boldsymbol{d}_i = F_i[\boldsymbol{m}] \quad i = 1, 2, 3, \cdots, N \ , \tag{3.15}$$

where $\boldsymbol{d}_i$ represents the N data points of the RF observation; $\boldsymbol{F}_i$ is the operation function that produces the RF waveform based on the model $\boldsymbol{m}$; $\boldsymbol{m}$ is a model with M layers, representing by an M-dimensional vector. The relationship in Equation (3.15) is nonlinear. In linear inversion problem, one can expand it into a Taylor series in respect of an initial model $\boldsymbol{m_0}$ that is "close" to the true shear wave velocity model $\boldsymbol{m}$ (Ammon et al., 1990), to further linearize Equation (3.15) into

$$F_i[\boldsymbol{m}] = F_i[\boldsymbol{m_0}] + (\boldsymbol{G}, \Delta\boldsymbol{m})_i + O\|\Delta\boldsymbol{m}^{\mathrm{A}}\| \quad i = 1, 2, 3, \cdots, N \ , \tag{3.16}$$

where $\Delta \boldsymbol{m}$ is the model correction vector between $\boldsymbol{m}$ and $\boldsymbol{m_0}$; $\boldsymbol{G}$ is the first-order partial derivative of operation function F_i at $\boldsymbol{m_0}$; $(\boldsymbol{G},\Delta \boldsymbol{m})$ is the inner product between matrix $\boldsymbol{G}$ and $\Delta \boldsymbol{m}$; $O\|\Delta \boldsymbol{m}^{\mathrm{A}}\|$ is the nonlinear term that is neglected in solving linear inversion problems.

In this thesis, we perform non-linear inversion based on the genetic algorithm (GA) to improve the accuracy of the receiver function inversions. A similar waveform inversion approach was used to analyze P-to-S converted waves (Chen et al., 2015) and SS precursors (Dokht et al., 2016). An overview of this algorithm and detailed inversion procedures are detailed in the following subsections.

3.2.1 Overview of the genetic algorithm in inversions

Nonlinear RF inversion is one of the multi-parameter nonlinear optimization problems. Methods to solve nonlinear optimization can be classed into two groups (Sambridge & Drijkoningen, 1992). The first group is applying techniques that reply on the utilization of local information on the gradients of objective functions to optimize the result upon the given initial model by iteration. One well-known matrix inversion method belonging to this group is the least squares. Conversely the other one does not reply on derivative information, therefore, it avoids the process of a linearization of problems. Core of the second group is to use random processes in realizing optimization. Typical methods that are widely used in this group are Monte Carlo method, simulated annealing method, and genetic algorithm method.

Genetic algorithm is first developed by Holland (1975) and quickly progress and apply in many fields (e.g., Grefenstette, 1987; Goldberg, 1989; Davis, 1990; Beasley et al., 1993; Suman & Giri, 2015; Immanuel & Chakraborty, 2019). It is a search heuristic method generating great interest in the field of Artificial Intelligence (AI). This global optimization approach is originally inspired by Charles Darwin's theory of natural evolution (Haupt & Haupt, 2004). Although the genetic algorithm is related to the simulated annealing algorithm as they both are random search methods

to solve complex optimization problems with multiple minima via the mechanism of chance (Kirpatrick et al., 1983), genetic algorithm exhibits a greater advantage in problem-solving efficiency than simulated annealing technique and the Monte Carlo searching technique therefore wins the priority in solving complex optimization problems(Davis, 1990; Scales et al., 1991; Sambridge & Drijkoningen, 1992).

In natural evolution, the process of natural selection begins with selecting best individuals from a given population, then the selected individuals produce offspring with inherited genes. This new generation with the better genes may have a better chance to survive in the environment thus pass the genes with special characteristics to the next generation. This process keeps on iterating and finally generates one generation with the needed characteristics. In genetic algorithm, large-scale and complex models are represented by binary strings, so that the properties and characteristics of the original model can be reflected by the patterns of the arrangements of 0's and 1's. This algorithm searches the given models to extract their components in order to develop new models by a random manner. Five basic phases considered in a genetic algorithm are initial population, cost function (or fitness function), selection, crossover, and mutation (procedure of traditional genetic algorithm is shown in Figure 3.5).

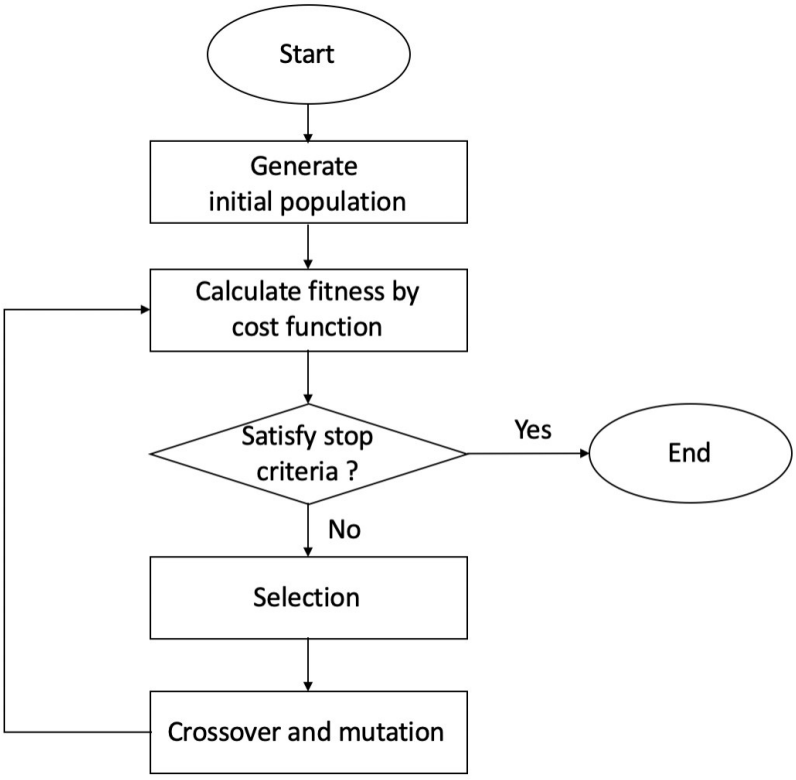

Figure 3.5. Flow chart of the traditional genetic algorithm process.

Initial population

In this algorithm, bits are named genes. A string of genes encoded is defined as a chromosome, which is the individual. A group of individuals is a population (Figure 3.6). The individuals that produce the first generation is called initial population. The size of the initial population is an important issue because the larger is the initial population, the more calculational cost are needed. To reduce the computational cost without affecting the sampling, through multiple tests, we set the initial population as 100 (Figure 3.7).

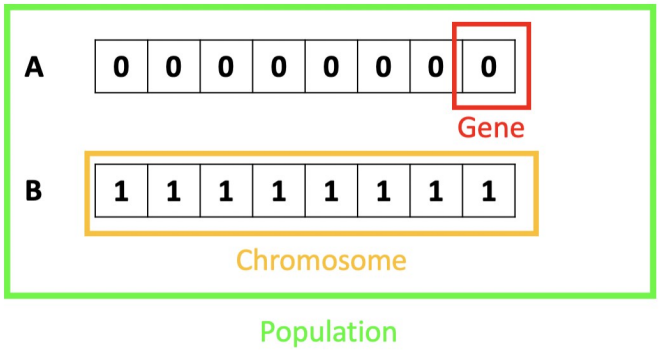

Figure 3.6. A schematic plot of the elements – gene, chromosome, and population – in the genetic algorithm.

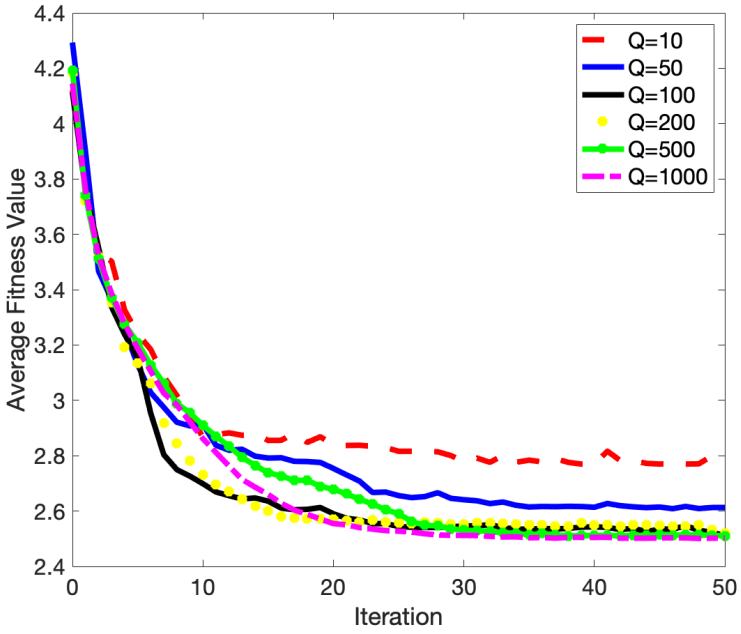

Figure 3.7. Comparison between different initial population sizes in the genetic algorithm. Q represents the only variate - the population size. When the population size is over 100, the optimal outcome is largely improved as the lower average fitness value indicates the better solution. Outcomes calculated by initial population sizes as 100, 200, 500, 1000 are similar. In view of the exponentially increased computational time in respect of the population size, 100 is the best initial population size.

Cost function

The cost function is the core of genetic algorithm. It essentially represents the relationships among different parameters, such as the differences between the observations and the synthetic seismograms in this thesis.

Selection

The purpose of selection is to choose the fittest individuals in order to produce the next generation with target genes. This phase attempts to minimize the cost functions in practical problems.

Crossover and mutation

Crossover and mutation are two operators that introduce new elements into the population. For crossover, during the production of new generation, the offspring models are derived from a mixing of the genes (bits) from two parental models (Figure 3.8a) under the control of a constant value named the probability of crossover. Unlike crossover, mutation that occurs in the offspring models is applied on one or more randomly chosen genes (bits) under the control of a constant value named the probability of mutation (Figure 3.8b). In general, high value of probability of crossover and low value of probability of mutation are routinely used to prevent mis-convergence and insufficient exploration of the parameter space. For small population size, it is better to get the optima through the dynamic increasing of low mutation probability and the simultaneous decreasing of high crossover probability (Hassanat et al., 2019). Mutation probability of 3% and crossover probability of 90% are determined through trial and error in the thesis to optimize the inverted model.

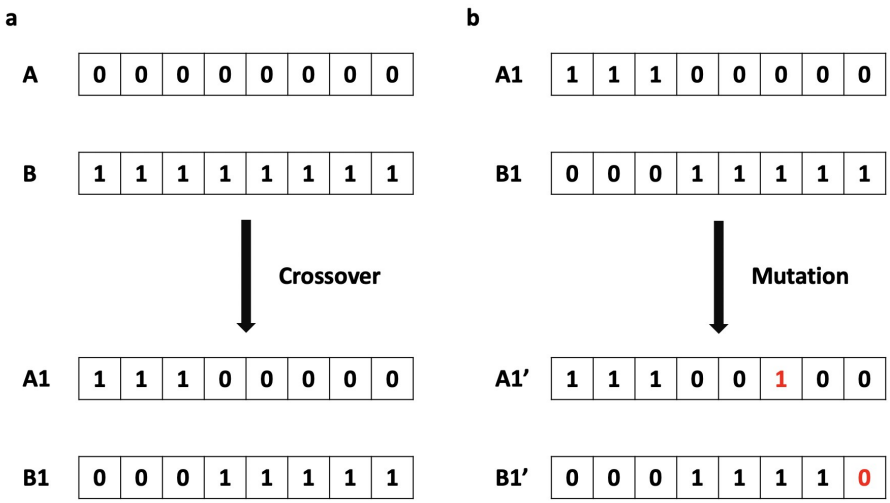

Figure 3.8. A schematic diagram of (**a**) the crossover and (**b**) the mutation in genetic algorithm.

3.2.2 Nonlinear RF inversion

We suppose that one has a model ***m*** with a set of unknowns x_i and a nonlinear cost function $\phi(\boldsymbol{m})$. Each unknown x_i is limited between the given a_i and b_i ($a_i \leq x_i \leq b_i$). To discretize, the interval d_i of x_i is

$$d_{,} = \frac{G_{\%} + H_{\%}}{I_{\%}} \quad i = 1, 2, 3, \cdots, M \ , \tag{3.17}$$

where N_i is the total number of the i-th parameter (x_i). Therefore, all the parameters representing the models ***m*** can be described as

$$x_{,} = a_{,} + nd_{,} \quad n = 1, 2, 3, \cdots, N_{,}; \ i = 1, 2, 3, \cdots, M \ . \tag{3.18}$$

The finite number of all possible models is

$$N_{\mathrm{HJJ}} = \prod_{,}^{\mathrm{K}} {}_{0} N_{,} \quad . \tag{3.19}$$

By calculation, the cost function $\phi(\boldsymbol{m})$ gives a series of (N_{all}) fitness values constrained by a bunch of a_i-s and b_i-s. The minimal value of $\phi(\boldsymbol{m})$ is the optima of one single computation.

In this dissertation, the RF inversion algorithm is programmed on the basis of MATLAB genetic algorithm code (Goldberg, 1989; Conn et al., 1991; Conn et al., 1997), with largely improved accessibility and convenience by encoded GUI (Dokht et al., 2016). Equation (3.16) can be rewritten as

$$(\boldsymbol{G}, \boldsymbol{m})_{,} = \Delta \boldsymbol{d}_{,} + (\boldsymbol{G}, \boldsymbol{m_0})_{,} \quad i = 1, 2, 3, \cdots, N \ , \tag{3.20}$$

where $\Delta \boldsymbol{d}_i$ is the residual vector between $(\boldsymbol{G}, \boldsymbol{m})_{,}$ and $(\boldsymbol{G}, \boldsymbol{m_0})_{,}$; N is the population size. Therefore, the cost function of the inversion is

$$J = \|(\boldsymbol{G}, \boldsymbol{m})_{,} - (\boldsymbol{G}, \boldsymbol{m_0})_{,}\|_{\mathrm{A}}^{\mathrm{A}} + \mu \|(\boldsymbol{D}, \boldsymbol{m_0})_{,}\|_{\mathrm{A}}^{\mathrm{A}} \quad i = 1, 2, \cdots, N \ , \tag{3.21}$$

where μ is a regularization parameter that controls the trade-off between the misfit and the model norm (i.e. the first term and the second term on the right-hand side of this equation, respectively); $\boldsymbol{D}$ is a discrete approximation to the first-order derivative matrix, shown as

$$\boldsymbol{D} = \begin{bmatrix} 1 & -1 & 0 & 0 & \cdots & 0 & 0 \\ 0 & 1 & -1 & 0 & \cdots & 0 & 0 \\ 0 & 0 & 1 & -1 & \cdots & 0 & 0 \\ 0 & 0 & 0 & 1 & \cdots & 0 & 0 \\ \vdots & \vdots & \vdots & \vdots & \cdots & \vdots & \vdots \\ 0 & 0 & 0 & 0 & \cdots & 1 & -1 \\ 0 & 0 & 0 & 0 & \cdots & 0 & 1 \end{bmatrix} . \tag{3.22}$$

To alleviate the non-uniqueness of the RF inversion, we (1) apply a joint inversion by low- and high-frequency RFs to constrain the structures at different waveforms and (2) assign different weights to model with a priori information. Equation (3.21) is subsequently rewritten as

$$J = \mathrm{g}\boldsymbol{W}[(\boldsymbol{G^{joint}}, \boldsymbol{m})_{,} - (\boldsymbol{G^{joint}}, \boldsymbol{m_0})_{,}]\mathrm{g}_{\mathrm{A}}^{\mathrm{A}} + \mu\|(\boldsymbol{D}, \boldsymbol{m_0})_{,}\|_{\mathrm{A}}^{\mathrm{A}} \quad , \tag{3.23}$$
$$i = 1, 2, \cdots, N$$

where $\boldsymbol{W}$ is the weighting matrix; $\boldsymbol{G^{joint}}$ is the $\boldsymbol{G}$ matrix for low- and high-frequency RFs, respectively. In this thesis, we adopt modified CRUST 1.0 by refining the depth increments and Poisson's ratios (see Chapter 4 for details) as the initial model $\boldsymbol{m_0}$, and for each iteration, the system computes synthetic P-to-S converted waveforms through a forward modeling based on the algorithm introduced by Svenningsen and Jacobsen (2007). One example of our inversion result is shown in Figure 3.9, which is the output of the inversion based on genetic algorithm by using the input, including the observed RFs and initial model from CRUST 1.0 (i.e. the shear wave velocities and Poisson's ratios at each depth; Figure 3.10) .

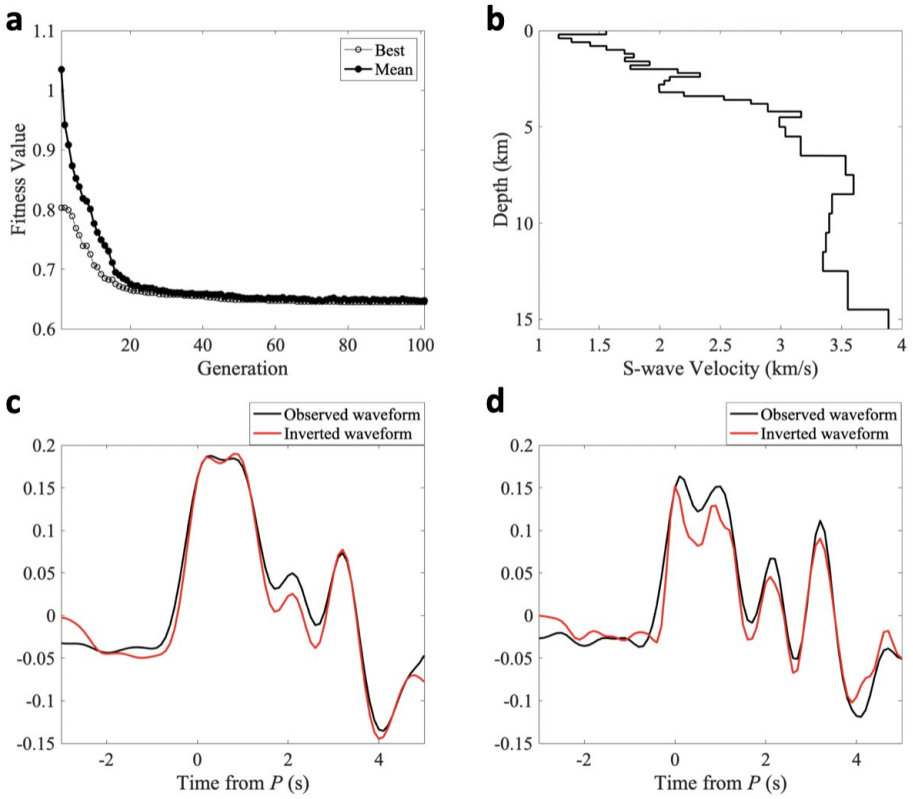

Figure 3.9. An inversion outcome of station TD005. **a**. The convergence of the mean and best fitness values (i.e. the minimum value of the cost function). **b**. Final inverted shear wave velocity model. **c**. A graph of the low frequency observed radial component and the inverted waveform. **d**. A graph of the high frequency observed radial component and the inverted waveform.

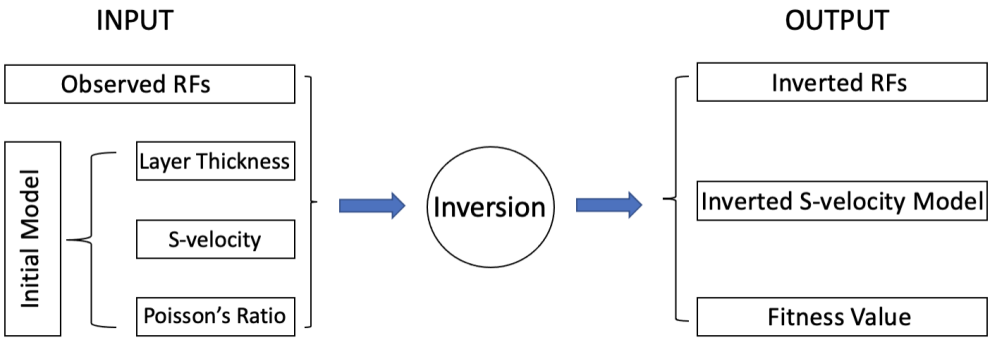

Figure 3.10. A flow chart of the inversion process.

Chapter 4. Recovery of the Alberta Basin sedimentary structures in southern-central Alberta using Nonlinear Inversions of Receiver Functions

4.1 Introduction

The Alberta Basin is a vast sedimentary wedge superimposed on the Precambrian crystalline basement of the western North American Craton. The tectonic backdrop of this basin, the depocenter of the WCSB, provides important clues on the formation of the entire WCSB. This chapter aims to provide new seismic constraints on the sedimentary strata of the Alberta Basin based on continuous waveform data collected from nearly two decades of regional passive seismic deployments. Our goal is to develop integrated shear velocity models of the sediment-basement transition beneath each receiver. The range of depth (0-14 km) of the resulting self-consistent shear velocity models effectively bridges the gap between the vertical scales of well logging (0-6 km) and those of traditional broadband analysis (>10 km) involving RFs and surface waves.

4.2 Data and method

Our dataset comprises of 80 broadband seismic stations from 7 seismic networks in southern-central Alberta and along the cordillera (Figure 4.1). The recorded broadband seismic signals were generated by global earthquakes larger than Mw 5.5 from 2001 to 2018, in the epicentral distance range between 30 and 90 degrees (Rondenay, 2009). Individual station back-azimuths differ slightly from the averages (Figure 4.1b), but generally offer relatively unbiased data coverage. Our test on the effect of azimuth suggests that the inverted models based on arrival angles in different azimuth bins do not differ significantly from the main findings (Figure 4.2). To compute RFs, we first isolate the P wave coda using a 150-seconds time window (i.e., 30 s prior to and 120 s after the direct P wave), and then apply a Butterworth bandpass filter with the corner frequencies of 0.03 and 5 Hz to remove incoherent noise. To ensure sufficient data quality for our analysis, we

further define a signal-to-noise ratio (SNR) criterion as the ratio between the standard deviation of the vertical component of an RF in the time window of 1-25 s after the onset of P (Dziewonski & Anderson, 1981) and that of a noise window of 105-5 s prior to P. For seismograms with an SNR greater than 2, we compute the RFs by deconvolving vertical component seismogram from the radial component with a water-level deconvolution method (Ammon, 1991; Aki & Richards, 2002) and apply a Gaussian filter to minimize high frequency noise. We incorporate two different frequency ranges by setting the Gaussian filter width parameters to 2.5 and 5.0, which correspond to the center frequencies of 1.2 Hz and 2.4 Hz, respectively (Ammon, 1991). As the last step of quality control, we manually select more than 14,000 high-quality RFs for the subsequent processing, with an approximately 100 RFs retained at each station.

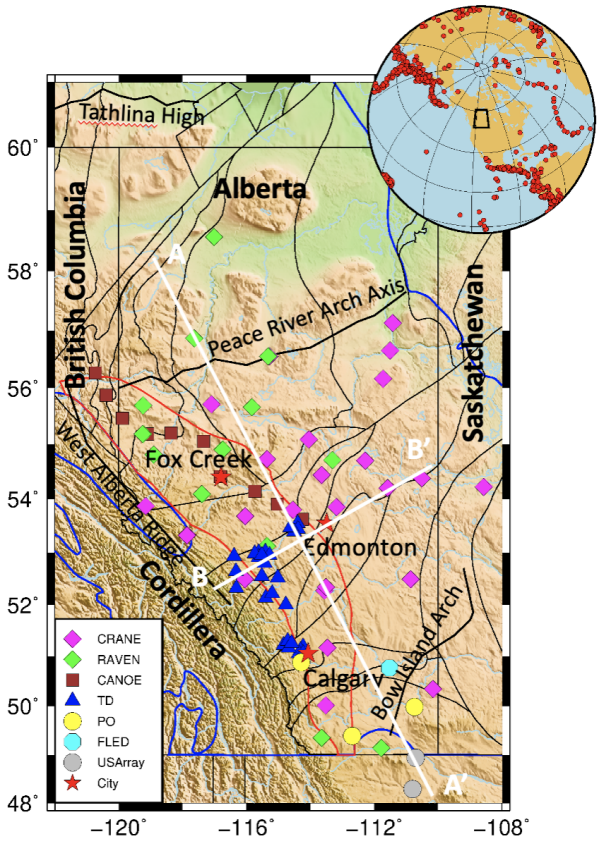

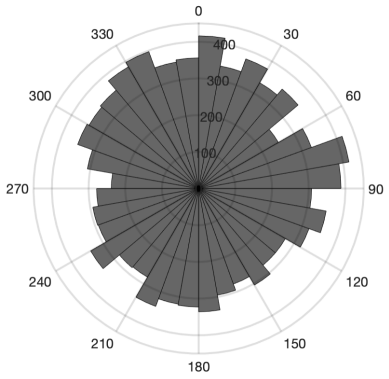

Figure 4.1. a. Station distribution displayed on a regional topographic map. In the inset, the red circles mark all earthquakes analyzed in this study. The blue line delineate the boundary of the WCSB and the red line indicates the depocenter of the Alberta Basin. The two white solid lines AA' and BB' indicate the two cross-sections (see Figure 4.6) from north to south and from west to east, respectively. The black lines indicate the tectonic domains of the Precambrian basement of the WCSB. Abbreviations: Bu, Buffalo Head; H, Hottah; He, Eyehill High; Hl, Loverna Block; MHB, Medicine Hat Block; Ks, Ksituan; L, Lacombe Domain; Ry, Rimbey; STZ, Snowbird Tectonic Zone; T, Taltson; Th, Thorsby; VS, Vulcan Structure; Wa, Wabamun. **b.** A rose diagram showing the distribution of station azimuths.

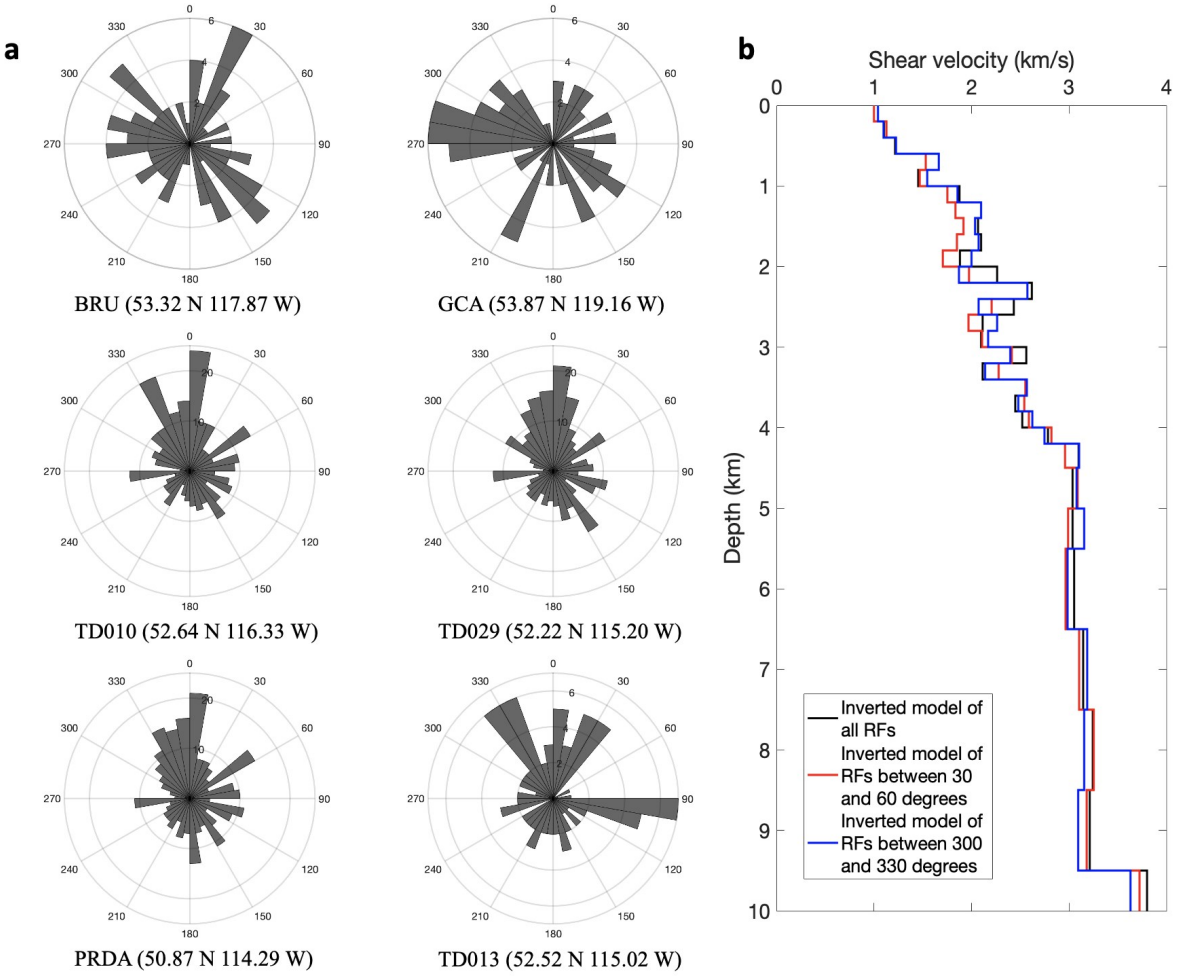

Figure 4.2. a. Rose diagrams showing the distribution of azimuths of several stations at basin margin along the Cordilleran Deformation Front. **b.** Inverted 1D models of station TD013 based on all arrival angles (black) and subsets of arrival angles in different azimuth bins as 30-60 degrees (red) and 300-330 degrees (blue).

To recover the sedimentary structures, we perform non-linear joint inversion based on the genetic algorithm (Chen et al., 2015; Dokht et al., 2016) to match the first 5 s of the continuous waveforms after the onset of P phase. Our inversion is based on the forward modeling approach proposed by Svenningsen and Jacobsen (2007). The cost function of the inversion is

$$J = \mathrm{g}\mathbf{W}(\mathbf{G}^{\mathbf{joint}}\mathbf{m} - \mathbf{G}^{\mathbf{joint}}\mathbf{m_0})\mathrm{g}_{\mathrm{A}}^{\mathrm{A}} + \mu\|\mathbf{D}\mathbf{m_0}\|_{\mathrm{A}}^{\mathrm{A}} \ , \qquad (4.1)$$

where **W** is the weighting matrix; $\mathbf{G}^{\mathbf{joint}}$ is the first-order partial derivative of cost function (for either low- and high-frequency RFs) and the forward operator. In this equation, **D** is a discrete approximation to the first-order derivative matrix, $\mathbf{m_0}$ is the initial model and μ is a regularization parameter that governs the trade-off between misfit and model norm; this parameter is determined by the trade-off curve through trial and error (Figure 4.3). Assuming an average S-wave velocity and P-wave velocity of 2.0 km/s and 4.0 km/s, respectively, for the sedimentary cover, the 5-second inversion window after P is sensitive to S-wave velocities and P-wave velocities as deep as 10 km and 20 km, respectively, considerably greater than the reported basement depth from regional well-logs.

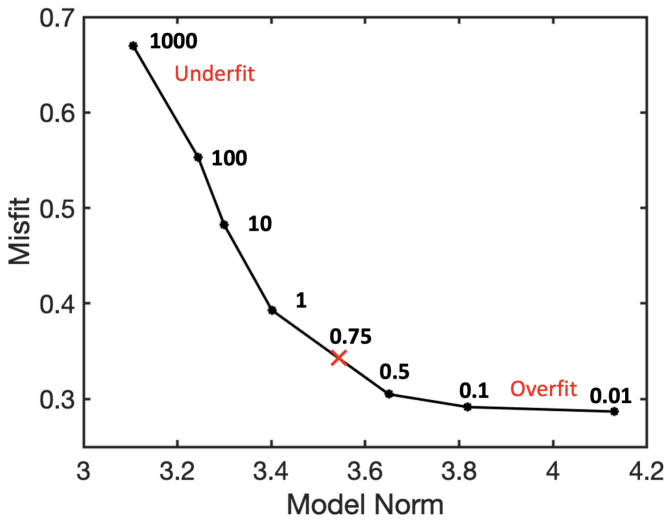

Figure 4.3. To determine an optimal regularization parameter the misfit function has been plotted against model norm for the 50th iteration resulting in a typical L-form. Following a common practice, we choose value of 0.75 at the turning point (red cross).

Necessitated by the complexity of the sedimentary structures, the genetic algorithm (GA, Davis, 1990; Stoffa & Sen, 1991; Haupt & Haupt, 2004; Chen et al., 2015; Dokht et al., 2016) seeks the optimal solutions through a global search. By introducing random perturbations to solutions in each generation, GA is resistant to local minima associated with improper choices of initial models.

Furthermore, by performing joint inversion of RFs from two distinct frequency ranges at each station, our model values are sensitive to layers of variable thicknesses.

To set the initial model for the GA inversion, we adopt the CRUST 1.0 model (Laske et al., 2013) and modify its layer thicknesses and Poisson's ratios to meet the reported sedimentary conditions in the WCSB. Specially, to improve the accuracy of our inversion results, we divide the depth increment into fixed smaller segments that correspond roughly to ~200 m in depth. To improve the reported Poisson's ratios from CRUST 1.0, a relatively coarse global model, we incorporate the lithology and the distribution of pore and crack shapes (Tatham, 1982) by integrating with reported values from well-logging data (Tobon, 2012) to limit the range of V_p/V_s ratios. The reported regional V_p/V_s ratios vary from 1.7 at the top of the basement to ~5 near the free surface in a typical sedimentary basin. According to the following conversion between Poisson's Ratio and V_p/V_s,

$$\nu = \frac{(@_{\#}/@_{(})^{*}+\mathrm{A}}{\mathrm{A}(@_{\#}/@_{(})^{*}+\mathrm{A}} \ , \tag{4.2}$$

where ν represents the Poisson's Ratio. We adopt a linear gradient model in which Poisson's ratio varies by 0.25 at the base of the sedimentary strata to 0.48 at the free surface in corresponding to the V_p/V_s ratios. Within each layer, the velocity perturbation is permitted to deviate from the initial value by up to 15% during inversions. Our final inversion results generally recover over 90% of the amplitude in the observed waveforms (Figure 4.4).

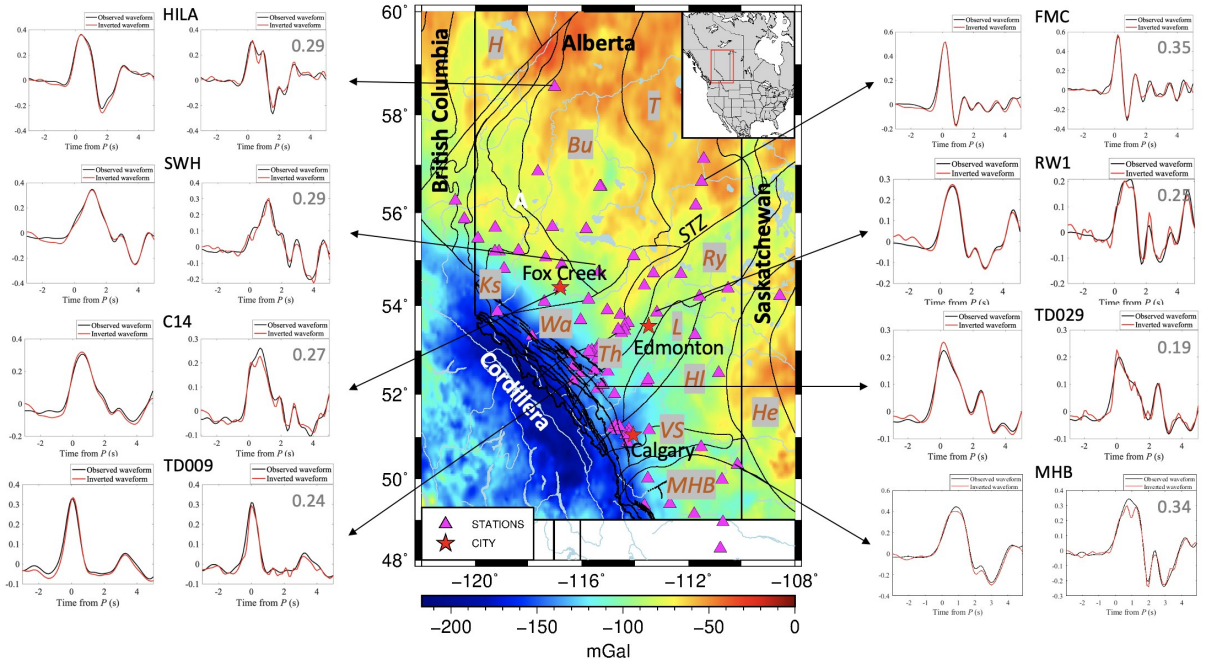

Figure 4.4. Sample waveform inversion results projected on a regional map of the Bouguer gravity anomaly. The black lines in the background mark the tectonic domains of the Precambrian basement of the WCSB. In each plot of inversion results, waveforms show in black and red colors correspond to the observed and inverted RFs, respectively. The numbers indicate the misfits between observations and predictions. Abbreviations: Bu, Buffalo Head; H, Hottah; He, Eyehill High; Hl, Loverna Block; MHB, Medicine Hat Block; Ks, Ksituan; L, Lacombe Domain; Ry, Rimbey; STZ, Snowbird Tectonic Zone; T, Taltson; Th, Thorsby; VS, Vulcan Structure; Wa, Wabamun.

We further adopt *H*-κ stacking, which was first introduced to study the depth of Moho (Zhu & Kanamori, 2000; Gu et al., 2018), to provide added constraints on the properties (i.e., thickness and Vp/Vs ratio) of the sedimentary strata. In this approach, H represents the depth of the basement and k is the V_p/V_s ratio. This algorithm performs a grid search for the most energetic stack of the direct Ps phase as well as the trailing multiple-converted phases on the basis of predicted delays relative to the direct P phase. The stacked amplitude should reach a maximum value when all phases in consideration are stacked coherently with the optimal thickness (H) and V_p/V_s ratio (κ).

4.3 Results

4.3.1 Robustness of inversion results

Based on the inverted models, shear velocities in the sedimentary strata vary between 0.9 and 2.7 km/s (Figure 4.5). The average value is 1.84 km/s, which agree reasonably well with an earlier estimate of 1.9 km/s for Cretaceous sandstone in southeastern Alberta based on sonic well-logging data (Xie, 2014). Collectively, 45 out of 80 inverted velocity profiles contain a thin (~0.2 km) layer near surface with an anomalous high shear velocity of ~2.0 km/s (Figure 4.5a). To ascertain the existence and robustness of this layer, we perform forward simulations where a 0.2-km thick layer of high velocity (1 km/s increment) is inserted into the starting model at small depth increments within the top 1 km of the strata (Figure 4.5b). The resulting waveforms from forward simulations are nearly identical for cases with and without this layer (Figure 4.5c), which suggests that the presence of near-surface artefacts due to limited vertical resolution is most likely responsible. Therefore, we fix the velocity of this abnormal layer in later results.

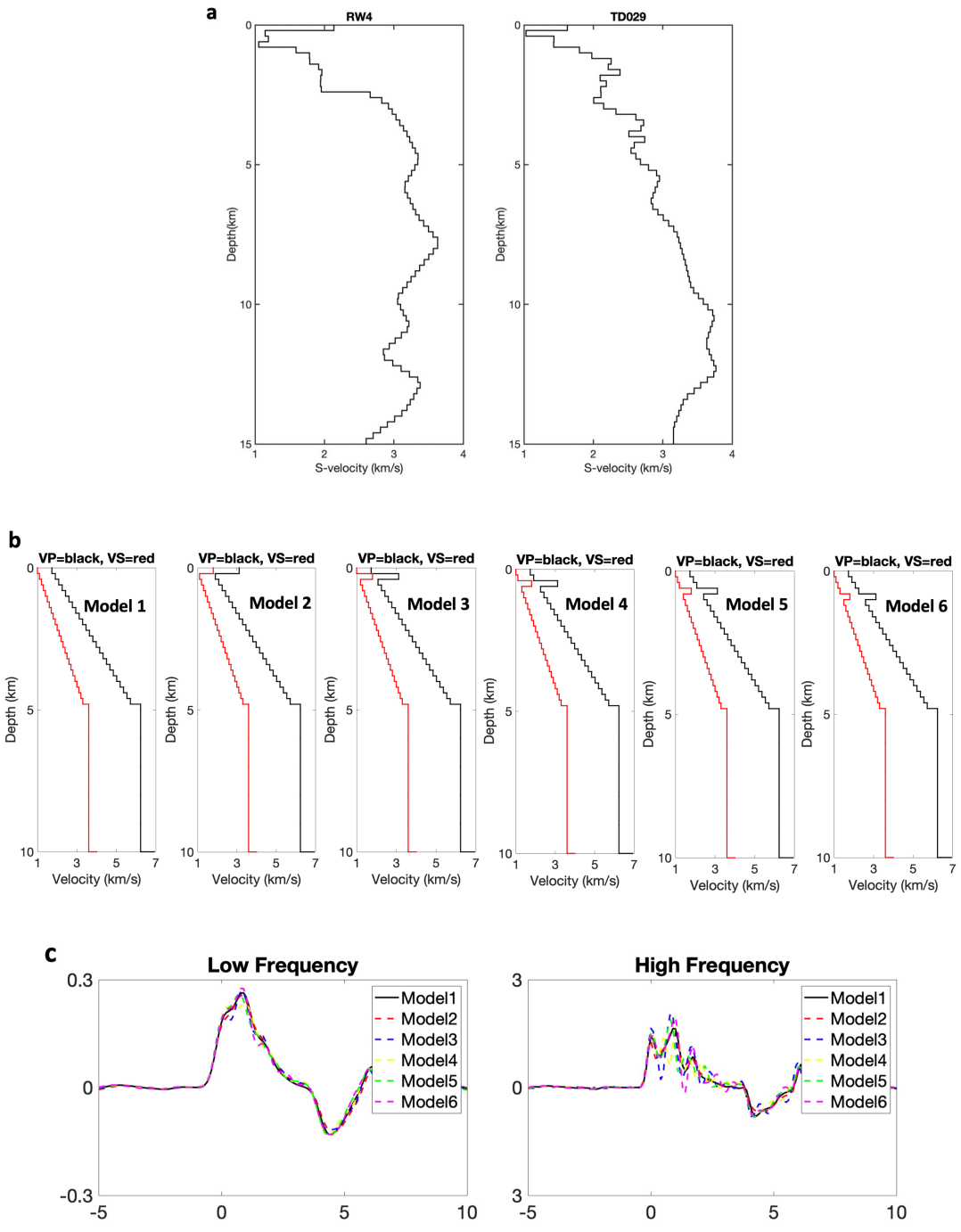

Figure 4.5. **a**. Two recovered models for stations RW4 and TD029 (located in the *Wabamun* and *Rimbey* tectonic domains, respectively), showing anomalously high velocity at the surface. **b**. Five models with and without a 0.2-km thick high velocity layer. Model 1 contains no high velocity layer, whereas Models 2-6 contain a high velocity layer from the surface down to depth of 1 km. Red and black lines indicate the shear and compressional velocities, respectively. **c**. Low- and high- frequency RFs computed from Model 1 to Model 6.

4.3.2 Depth of the crystalline basement

The inverted waveforms, factoring the inherent noise embedded in the data, are sufficient to resolve horizontal stratifications with thicknesses greater than 200 m, especially the depths of the sediment and the shear velocity structures in the shallow basement. To assist the analysis of lateral changes in structures, we plot cross-sections of interpolated shear wave velocities from north to south and from west to east, respectively, with both profiles clearly revealing the boundaries between the sedimentary basin and the upper crust (Figure 4.6a). Shear wave velocities increase with depth from 0.5 km/s to 4.2 km/s. Abnormally high S-velocity in the upper crust may be cause by (1) a high velocity zone known as Winagami reflection sequence (WRS) in the Alberta basin between the depths of 6.5 and 16.5 km, caused by the presence of mafic sill complex intrusion (Ross & Eaton, 1997; Welford & Clowes, 2006); or (2) inversion artifacts induced by the mid-crustal LVZ between 11 and 28 km resulting a relic of partial melting zone (Chen et al., 2015). The westward dipping sedimentary strata continue laterally, showing 4-6 layers with cumulative thicknesses of ~6 km beneath the cordillera and 3-4 km beneath the Alberta basin. This coherent trend is consistent with that from the Alberta Geological Survey (AGS) based on well-logs (dots in Figure 4.6a, Branscombe et al., 2018).

Furthermore, the S-wave velocity at the basement is ~2.7 km/s, which falls within the reported range of CRUST 1.0 (2.59 - 2.74 km/s in Alberta). To ascertain our inversion results, we compute the gradients of the velocity-depth curves in cross-sections AA' and BB' (Figure 4.6b). A strong positive gradient is evident on each cross-section, providing evidence for a sharp interface at variable depths. This interface roughly coincides with the S-velocity contour of ~2.7 km/s (black lines in Figure 4.6b), which is interpreted as the top of the crystalline basement by AGS (red dots in Figure 4.6b).

To improve the accuracy of basement boundary depth estimations, we introduce a modified H-κ stacking method based on an earlier published algorithm of Gu et al. (2018) derived from Zhu and Kanamori (2000), which was routinely used in delineating the Moho interface (Zhu & Kanamori,

2000; Yeck et al., 2013). This modified method is more stable and flexible than the original algorithm due to a ray tracing-based approach (Niu et al., 2007) and a multilayer global crustal model. We then adopt the sedimentary structure model of CRUST 1.0 (Laske et al., 2013; Pasyanos et al., 2014) and calculate the most energetic stacks of both the direct Ps phase and the later multiple converted phases (i.e. PpPs and PpSs+PsPs). Because of a relatively weak converted phase resulting from the Precambrian crystalline boundary, as well as scattering and defocusing caused by sharply dipping interfaces and sedimentations, the *H-κ* stacking results are particularly accurate in resolving the depth and elasticity of relatively flat interfaces (Figure 4.6c).

From the computation, V_p/V_s ratio of the focus is ~1.75 with uncertainties in the range between 0.01 and 0.06, which overlaps with the range provided by well-logging data (1.7-2.0; Tobon, 2012), and the uncertainties of basement depth are less than 0.4 km.

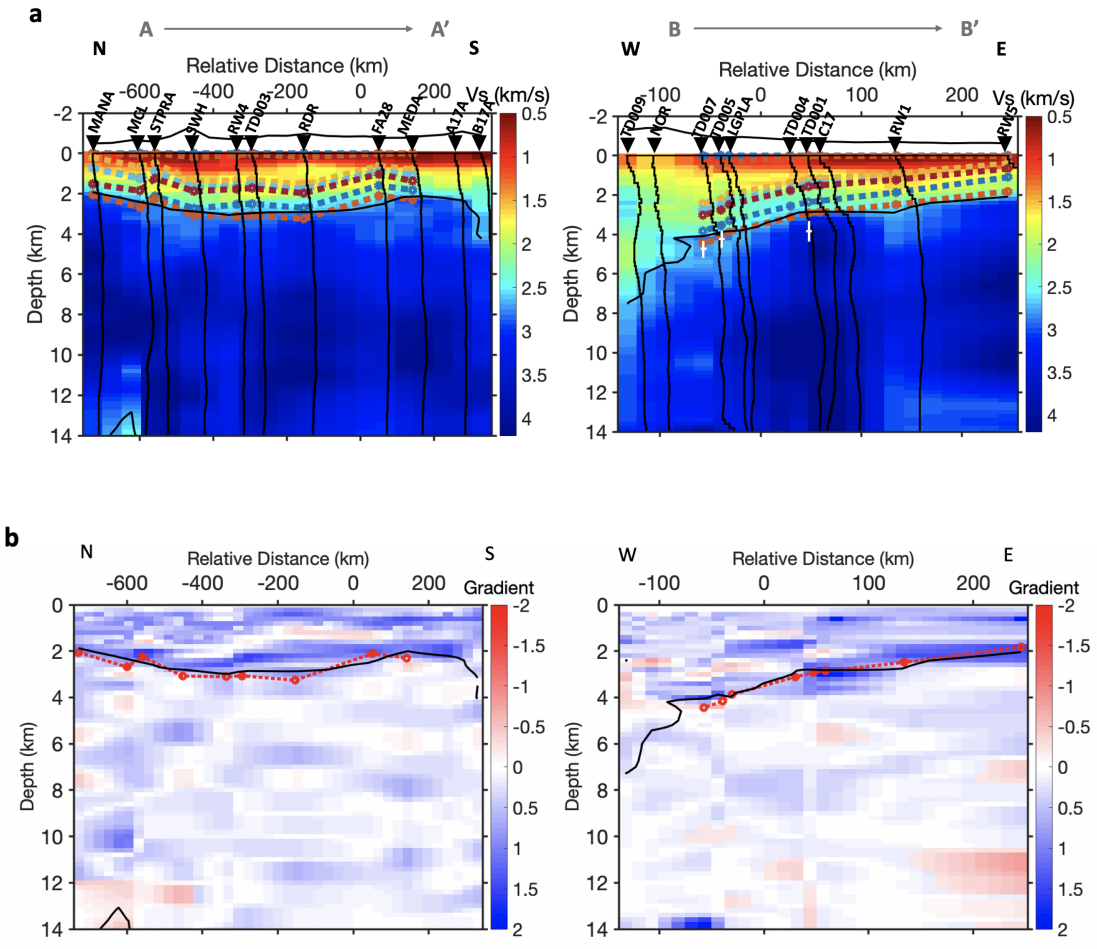

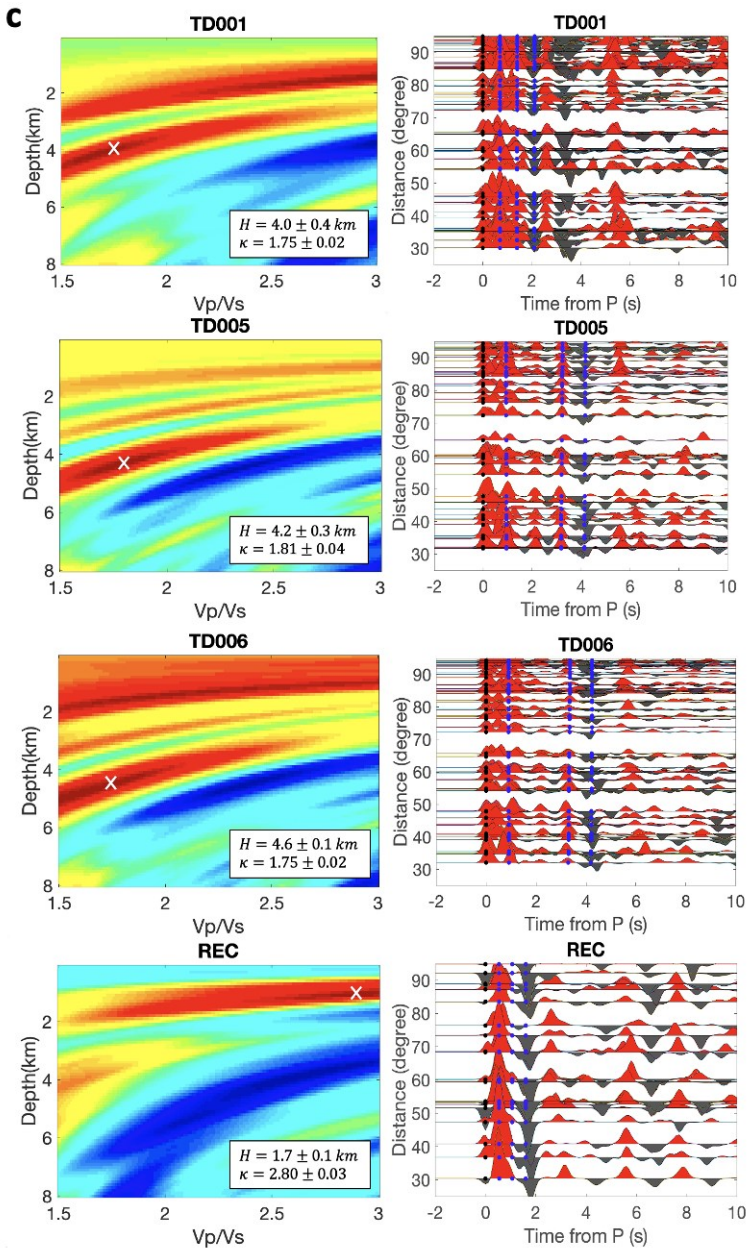

Figure 4.6. **a**. North-to-South and West-to-East cross-sections of interpolated velocities from receiver function inversions. The multicolored circles mark the proposed depths (Branscombe et al., 2018, Open-file report, AGS) of the sedimentary stratigraphic sections with different ages, which, starting from the surface, indicates Quaternary, Neogene to Paleogene, upper Cretaceous, lower Cretaceous, Jurassic to Permian, Devonian, and Ordovician to Cambrian. The vertical black lines show the S-velocity models from receiver function inversions. The horizontal black lines indicate the depth at which the S-velocity is 2.7 km/s. **b**. Vertical gradients of the velocity-depth curves in North-to-South and West-to-East cross-sections. The depth of a significant increase of gradient according to AGS (red dots). Black lines indicate the depth where the S-velocity is 2.7 km/s. **c**. *H-κ* stacking results and waveforms of four selected stations. White crosshairs mark the optimal *H-κ* values. The warm colors mark regions of high stacking energy. Black dot-lines in waveform plots indicate the direct P wave, and the blue dot-lines indicate the Ps, PpPs and PpSs+PsPs phases, respectively. The positive polarized phases between 5 and 6 s are Moho converted phases induced by Moho at the depth of 35-40 km in the Alberta basin (Bouzidi et al., 2002; Pasyanos et al., 2014; Gu et al., 2018). The depths of the basement beneath stations TD001, TD005, TD007 (computed by *H-κ* stacks) are indicated by the white crosshairs in the right-hand-side cross-section in **a**, and the length of the crosshairs represent the relative depth.

Due to sedimentary structural complexities, a number of stations in our study show multiple energy foci in the H-κ domain (i.e. non-single H-κ maxima; e.g., stations TD001 and TD006; Figure 4.6c). In general, basement depths and V_p/V_s ratios computed from the H-κ stacking generally overlap with those of CRUST 1.0, showing large V_p/V_s ratios in the relatively shallow crystalline basement (e.g., at station REC in northern Alberta; Figure 4.6c). We then use the H-κ results to fix the basement depth from RF inversion, and for stations with multiple H-κ maxima we allow the inversion to determine the optimal depth. Our model of the Precambrian basement shows higher regional resolution than CRUST 1.0 (Figure 4.7a). In comparison with the available well-logging data (Figure 4.7b), our modeled basement depths at the majority of the stations are within 20% of the earlier reported values (Figure 4.7d). The uncertainty of the depth of the boundary between the sedimentary basin and upper crust increases towards the CDF however, which may be caused by the complex sedimentary structures along the fold-and-thrust belt.

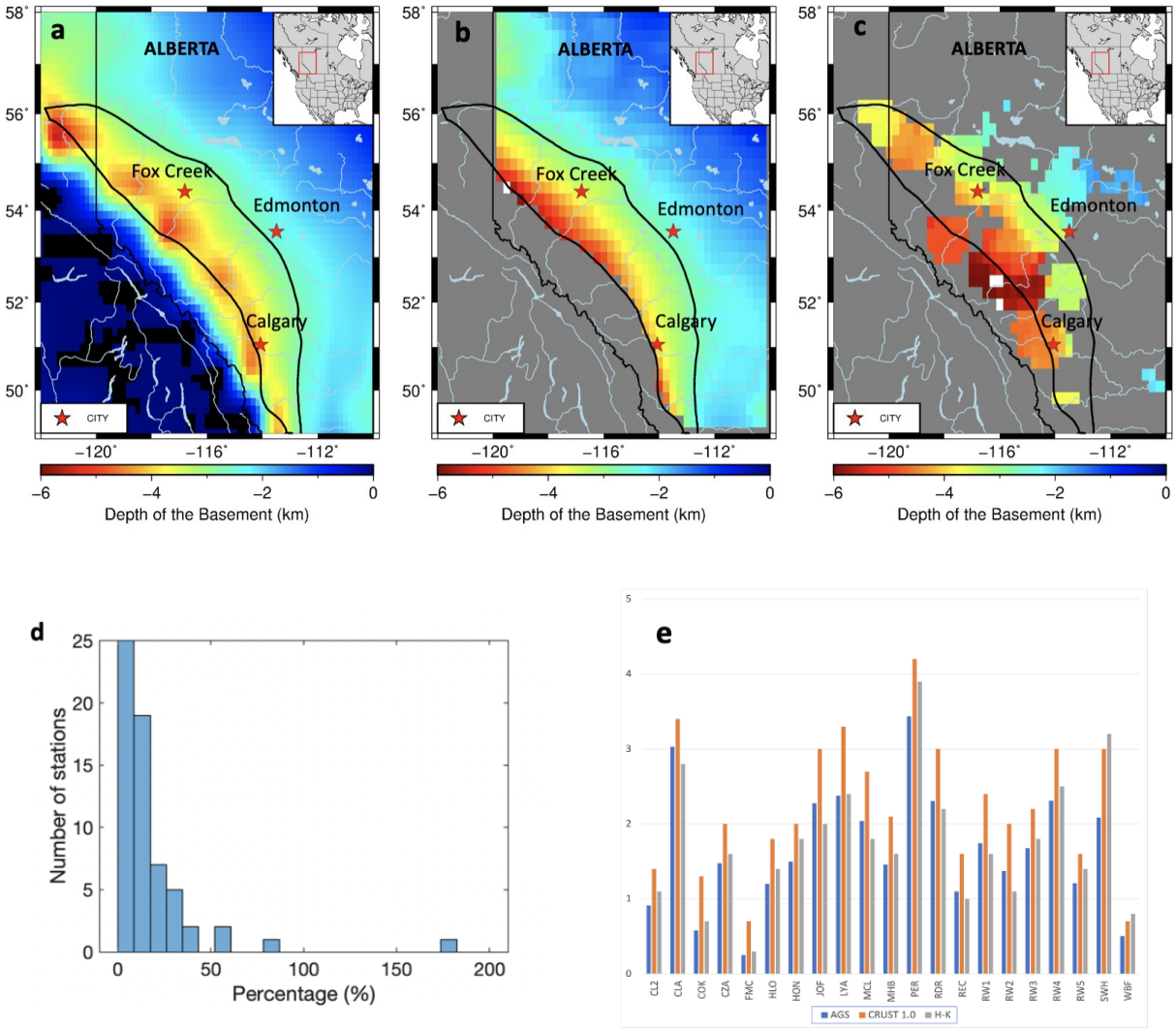

Figure 4.7. A comparison of the basement models among (**a**) CRUST 1.0, (**b**) the result from AGS by well-logs, and (**c**) the result from our study by RF inversion and *H-κ* stacking. Black contours mark the boundaries of the Alberta Basin. **d**. A histogram showing the basement depth difference between this and previous studies. The percentage on the x-axis is calculated by the ratio of the absolute differences between our results and earlier data (normalized by the latter, i.e., ratio = |depth difference| /previous depth data). The majority of the stations show reasonable consistency (<25% difference). **e.** A comparison of the basement depth of stations in CRANE network among AGS, CRUST 1.0, and this study.

4.4 Conclusion

Understanding the formation of the WCSB (concentrate on the Alberta Basin in this research) is crucial for both geophysical research and mineral resources exploration. In this chapter we introduce RF imaging, an independent, more cost-effective means than seismic exploration and well-logging efforts, to recover the geophysical properties of the sedimentary strata. Using earthquakes from hundreds of kilometers away, we are able to determine both the depth of the basement and the shear velocities within and below the sedimentary strata. Through imaging and inversions, we are able to recover the sedimentary layers buried between 1.7-4.3 km depths near the wedge-top and southeastern foredeep depozones. The basement depth model derived from RF inversion and H-κ stacking has greatly improved resolution than CRUST 1.0, and meets the depth range from AGS by multiple well-logging results. This result verifies the capability of our method by combining the RF inversion with H-κ stacking to discern the complex sedimentary layers. This also offers a new idea on the study of complex subsurface structures. This relatively high-resolution shear velocity model provides supported materials for future study in this area. Further findings based on our model will be revealed and interpreted in Chapter 5.

Chapter 5. Applications of the Receiver Function Imaging: abnormal velocity zones and the subsidence history of the Alberta Basin

5.1 Introduction

Anomalous shear velocity zones, including low velocity zones (LVZs) and high velocity zones (HVZs), have been widely reported by active and passive seismic observations from a lot of disciplines. Pioneering studies offer a number of plausible mechanisms depends on the genesis and evolution of the resident tectonic provinces to the formation of these anomalous velocity zones (Ross & Eaton, 2002; Li et al., 2003; Welford & Clowes, 2006; Ward et al., 2013; Yang et al., 2012; Chen et al., 2015).

Sedimentary LVZs are generally in relation to the tectonic deformation and the existence of mineral resources. Tectonic deformation usually induces a fault zone which is seismically characterized as a LVZ (Zion & Aki, 1990; Chester et al., 1993; Evans & Chester, 1995; Ben-Zion & Shi, 2005; Dor et al., 2006; Yang & Zhu, 2010). Study of the LVZs is important to understanding the evolution of fault systems (Li et al., 1998; Vidale & Li, 2003; Yang & Zhu, 2010). The other possible genesis of the sedimentary LVZs is the low density of the mineral resources comparing with the surroundings according to the Snell's law that the soft media induce low velocities during the wave transmission (Aki & Richards, 2002; Shearer, 2019). Discovery of mineral resources is of great significance to the development of human society.

Crustal LVZs generally relate to the presence of magma body (Chmielowski et al., 1999; Chen et al., 2015) or partial melting in thickened crust (Yuan et al., 1997). Reduction of the shear wave velocities is caused by not only the magma intrusion or partial melting, but the aquifer layers and fluid-filled cracks because of metamorphic dehydration (Stern et al., 2007; Yang et al., 2012), and large-scale serpentinite in the forearc mantle wedge (Bezacier et al., 2010) or serpentine channels on the top of slabs (Abers, 2005). LVZs in crust are normally shown as by-product of collisional

tectonics during the subduction of oceanic crust (Yuan et al., 2000) as well as the continental convergence forming broad mountain ranges like the Himalaya-Karakoram-Tibetan Orogen (St-Onge et al., 2006). They also offer debatable evidence for the formation of the Precambrian crust during the tectonomagmatism (James et al., 2003) such as researches of the Trans-Hudson Orogen (THO) in North America (Ross et al., 1995; Corrigan et al., 2009).

Crustal HVZ has been widely documented from the upper to the lower crust and dominantly believed as the indication of mafic structures. Previous studies mainly focus on two positions of the HVZs. The first one is atop the Moho discontinuities at the lower crust, formed via various mechanisms including underplating during rifting (Kay et al., 1989; Funck et al., 2000), crustal melting and magmatic differentiation (Wolf & Wyllie, 1993; Jagoutz & Kelemen, 2015), subduction or collision process (Dilek & Furnes,2014), and crustal root densifications (Fountain et al., 1994; Fischer, 2002). The second one locates in the upper-middle crust, for example, the well documented Winagami reflection sequence (WRS) at the depth of 9 - 24 km in the northwestern Alberta (Ross & Eaton, 1997), which is equivalently referred to as the Winagami sill complex (Welford & Clowes, 2006) and firstly identified by Lithoprobe 2-D multichannel seismic reflection lines. The forensic mafic dominated sill complex extends through several Precambrian basement tectonic domains, centering on the Wabamun and the Chinchaga domains to the north of Snowbird Tectonic Zone. The emplacement of the WRS is believed to postdates the assembly of these tectonic domains and to be the contemporary with tectonism associated with the opening and closing of the Throsby domain. Its formation is suggested as a representation of a magmatic addition into the crust (Welford & Clowes, 2006).

5.2 Data and method

Our dataset comes from 80 broadband seismic stations locating in the central and southern Alberta and along the cordillera (Figure 5.1). The recorded seismic signals are induced by earthquakes

larger than Mw 5.5 from 2001 to 2018, in the epicentral distance range from 30 to 90 degree (Rondenay, 2009).

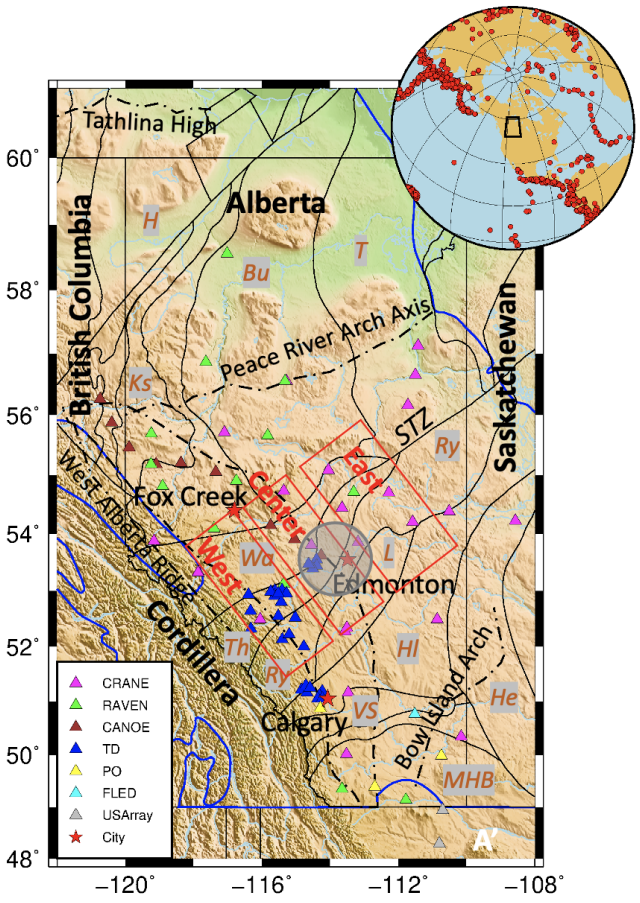

Figure 5.1. Station distribution displayed on a regional topographic map. In the inset, the red circles mark all earthquakes analyzed in this study. The blue line indicates the boundary of the WCSB and the red line indicates the depocenter of the Alberta Basin. Three red rectangles highlight the clusters of stations from west to east. The shaded circle marks the cluster of stations used in the calculations of basement subsidence (see Figure 5.). The black lines indicate the tectonic domains of the Precambrian basement of the WCSB. Abbreviations: Bu, Buffalo Head; H, Hottah; He, Eyehill High; Hl, Loverna Block; MHB, Medicine Hat Block; Ks, Ksituan; L, Lacombe Domain; Ry, Rimbey; STZ, Snowbird Tectonic Zone; T, Taltson; Th, Thorsby; VS, Vulcan Structure; Wa, Wabamun.

We perform a non-linear joint inversion based on genetic algorithm to recover the structures from sediments to upper-middle crust (see Chapter 3 & Chapter 4.2 for more details).

5.3 Results

5.3.1 Sedimentary low velocity zone (LVZ) revealed by the RF inversion

In view of the various changes of the strata from west to east in WCSB, we choose three clusters consisted of relatively concentrated stations with similar structures below in southwestern, central, and eastern Alberta (red rectangles in Figure 5.1). Average shear velocity maps of the three clusters (Figure 5.2) are concordant with the west-to-east cross-section (see Figure 4.6 in Chapter 4 for details). We flag a boundary when the inverted velocity exhibits a sharp increase if (1) the gradient is within the depth range of the boundary of two layers from previous well-logging data, and (2) the S velocity is generally consistent with previous lithological records (Branscombe et al., 2018). Finally, we divide our inverted models into 5 to 6 layers in the sedimentary strata. Notable layers identified in the sedimentary strata are a thick (> 1.5 km) Cretaceous layer and an apparent Devonian layer. In comparison, layers derived from other geological times such as the Jurassic, Triassic, and Permian are difficult to discern, which may reflect both lateral structural complexities and the resolution limit of RF imaging. Within each stratum, shear velocities exhibit significant similarities within each of the three clusters. A notable exception is the high shear velocities in the upper Cretaceous layer in the western part of the study region, which is locally supported by the abundant shale and mudstone deposited during the middle of the late Cretaceous (AGS, 2019). As the upper Cretaceous layer thins towards central and eastern Alberta, this high velocity structure diminishes as the RF inversion begins to reach its resolution limit.

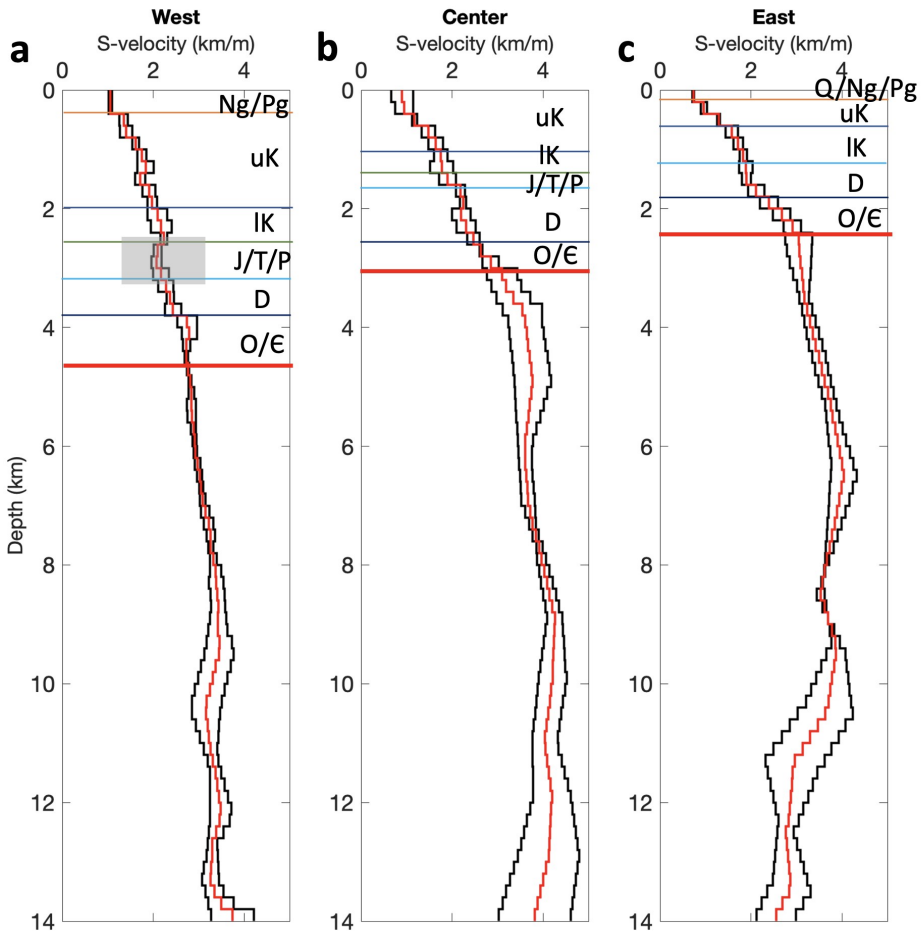

Figure 5.2. Three average shear velocity models of our inversion results at the (**a**) southwestern, (**b**) central, and (**c**) eastern Alberta. The locations of these three clusters are marked as red rectangles in Figure 5.1. In each panel the red curves show the average velocity models while the black curves mark the 1 standard deviation of the average velocity down to 14 km depth. Multicolored horizontal lines indicate the interpreted boundaries between different geological strata based on the velocity gradients, the horizontal bold lines mark the basement depth derived from inversion and *H-κ* stacking. The grey shade indicates the LVZ. Symbols: Q, Quaternary; Ng, Neogene; Pg, Paleogene; uK, upper Cretaceous; lK, lower Cretaceous; J, Jurassic; T, Triassic; P, Permian; D, Devonian; O, Ordovician; Є, Cambrian.

In southwestern Alberta, we observe a thin, low-velocity layer at the depth of ~2.7 km in the formation of the Jurassic/Triassic/Permian (grey shade in Figure 5.2a) in the average shear-velocity model. To verify the existence of this layer and quantify potential model biases, we perform several hypothesis tests based on forward waveform simulations using the Reflectivity Method (Bernasconi & Drufuca, 1990; Pirera & Zanzi, 1993). We also add random noises with

the value of ~40% of the signal, which is much larger than the ratio of noises (<20%) from the actual observation, to further verify the capability of RF inversion to discern LVZ in sediments. In the first test, we generate synthetic RFs by a simple gradient model. The RFs are subsequently subjected to the same inversion process detailed earlier. The shear velocities of the recovered model are ~4% slower than the initial model near to the boundary depth between sedimentary strata and upper crust. The extent of the recovery is reasonable, especially in view of the absence of notable artefacts surrounding the LVZ within the sedimentary layers of the inverted model (Figure 5.3a). In general, our inversions recover ~90% of the peak energy of the input waveforms and the majority of the peaks and troughs of the simulated data are properly resolved (Figures 5.3b and 5.3c).

In the second test, we introduce a 400 m thick low-velocity layer at the depth of 2.8 km. Presumed shear velocity and spatial scale of the low-velocity layer resemble those of observed profiles beneath stations in the western cluster (see Figure 5.2a). The inversion result from a variable shear wave velocity initial model successfully recovers the low velocity layer (to ~90% maximum amplitudes), showing nearly identical shear velocity and spatial scales as the input (Figure 5.3d) with an overall correlation coefficient of 0.90 (Press et al., 1992; Figures 5.3e and 5.3f). Since RF is more sensitive to velocity contrasts rather than absolute velocity (Ammon et al., 1990), we perform other inversions using two different initial models with constant S-velocity of 1.5 km/s and 2.5 km/s in the second test. The optimal solution models from 30 inversions (Figure 5.3d, blue and green lines) are capable of recovering the main features with acceptable differences (~7%).

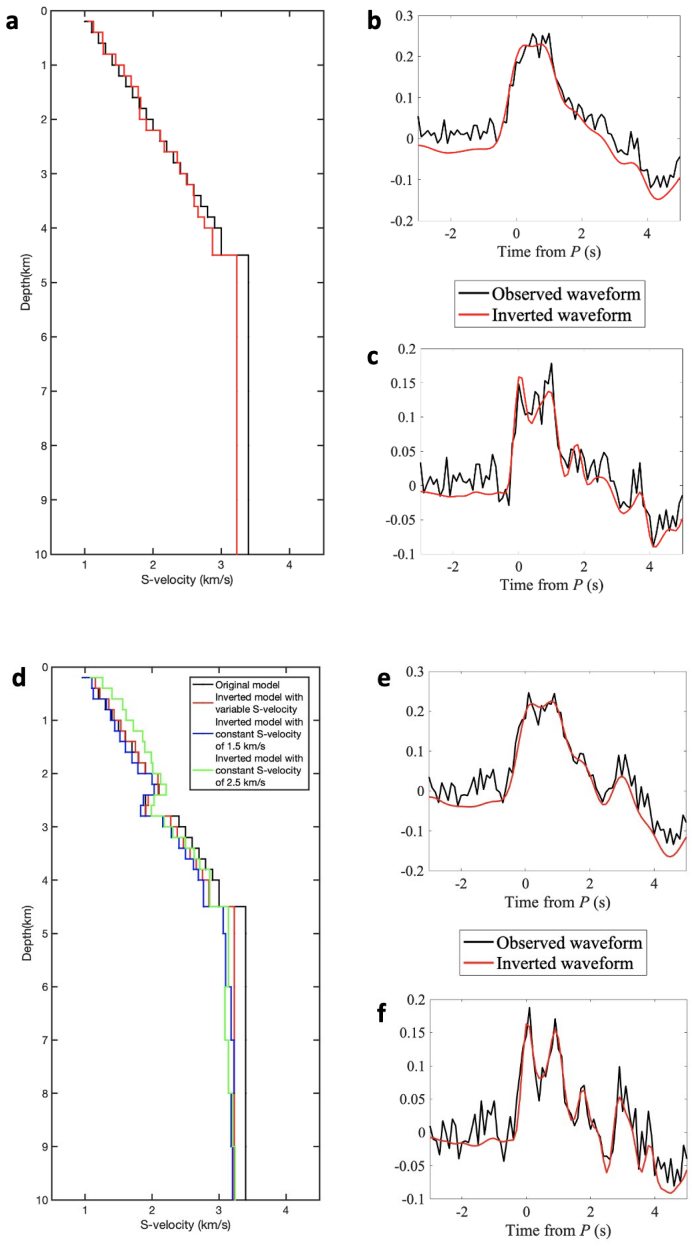

Figure 5.3. Results of waveform simulations and the correspondent non-linear inversion outcomes. **a**. A model showing gradational structures (black) and the recovered optimal model (red). **b**. The waveform fitting result of the low-frequency RF. The black line represents the RF by forward modeling, and the red line represents the inverted RF. **c**. The waveform fitting result of the high-frequency RF. **d**. A model showing a thin low velocity layer in the sedimentary strata (black) and the recovered optimal model with different initial models of variable (red) and constant (1.5 km/s, blue, and 2.5 km/s, green) S-velocity. **e** and **f**. The waveform fitting results of the low- and high- frequency RFs.

We also conduct more robustness tests with different scale and position of LVZ. The test result demonstrates that our non-linear inversion has the capability of discerning LVZ in sediments (Figure 5.4).

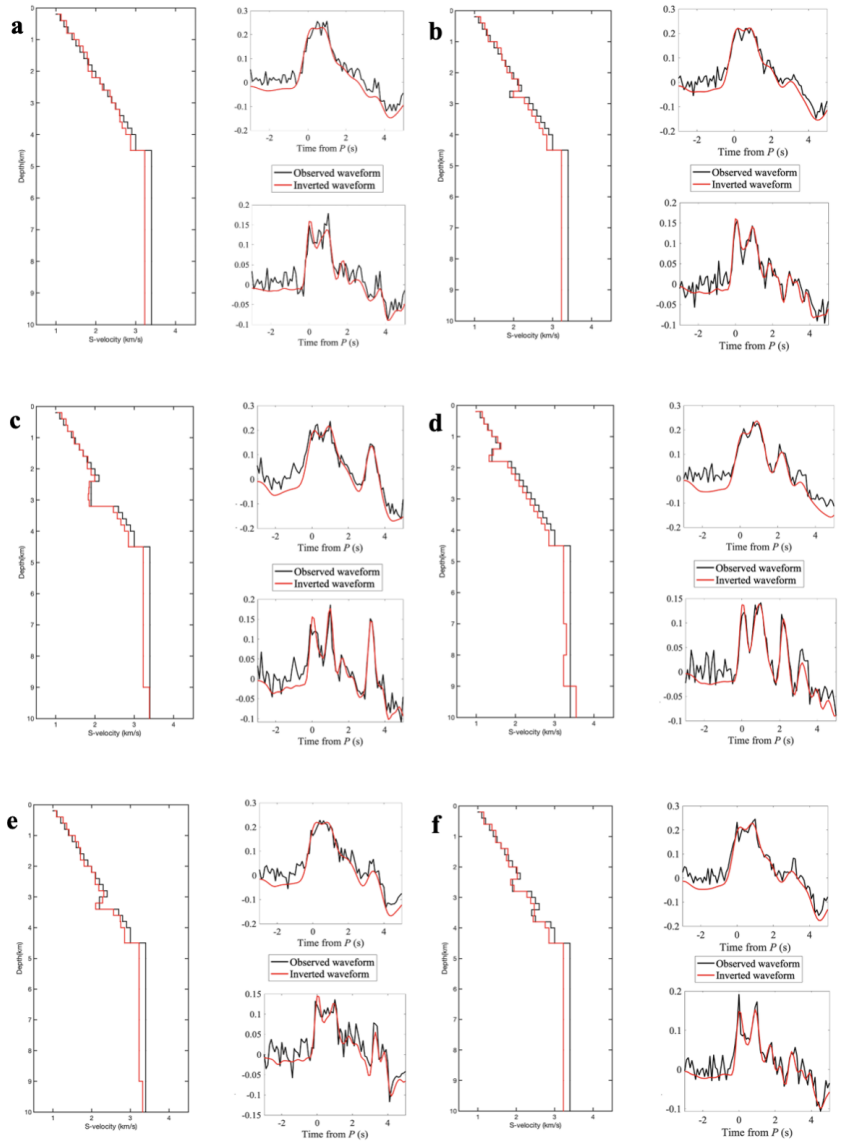

Figure 5.4. Results of waveform simulations and the correspondent non-linear inversion. **a.** A model showing gradational structures (black) and the recovered optimal model (red), as well as the correspondent observed waveforms with random noises (black) and the inverted waveforms (red) of low-frequency RFs (upper) and high-frequency RFs (lower). **b.** A model showing a thinner LVZ (200 m) and the correspondent results. **c.** A model showing a thicker LVZ (800 m) and the correspondent results. **d.** A model showing a shallow LVZ at the depth of 1.4 km and the correspondent results. **e.** A model showing a deep LVZ at the depth of 3.0 km and the correspondent results. **f.** A model showing two LVZs and the correspondent results. The value of random noises in the simulations is set to ~40% of the signals, which is much larger than the ratio of noises (<20%) from our observations of all stations.

To validate the robustness of the vertical resolution in our inversion, we also perform inversions based on different depth intervals (from 100 m to 800 m, Figure 5.5a and 5.5b) on model with 400-m LVZ of the second simulation test. The optimal inverted models from 20 inversions demonstrate that the model, especially the LVZ, can be fully recovered by using the selected layer thicknesses between 200 and 400 m (Figure 5.5b). According to the recorded well-logging data, the thickness of sedimentary strata is much thinner than 200 m. The finer details are beyond the vertical resolution limit of the RF inversions and may introduce artefacts to the outcomes. Further inversions of the stations in the southwestern cluster (Figure 5.2a) using depth increments of 200 and 400 m (Figure 5.5c and 5.5d) confirm the existence of the LVZ, but the output model with 400-m depth interval exaggerates the LVZ thickness by ~30%, thus suggesting that the optimal depth interval is ~ 200 m.

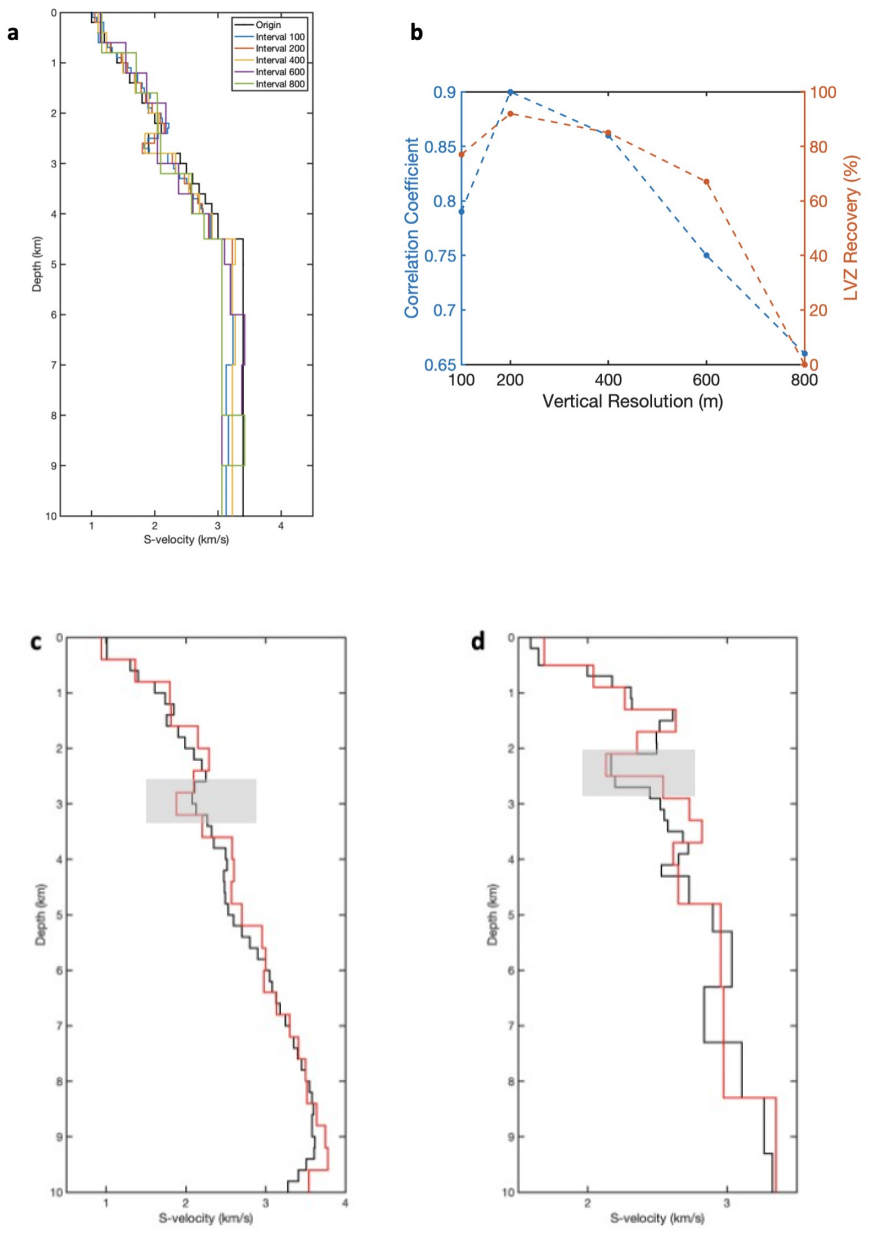

Figure 5.5. a. Optimal results from 30 inversions based on different depth intervals from 100 m to 800 m. The original model is highly recovered by using the layer thickness between 200 and 400 m. **b.** Correlation coefficients and the percentages of LVZ recovery of the inversions of the second simulation model by using different depth intervals (100, 200, 400, 600, and 800 m, respectively). **c.** Averaged S-velocity models of the southwestern cluster by using the depth intervals of 200 (black) and 400 m (red), respectively. Two models show the same trend with the difference of ~10%, as well as the fully recovered LVZ (grey shade). **d.** Two inverted models of station TD016 based on the depth increments of 200 (black) and 400 m (red), respectively. Shades indicate the potential range of LVZ.

Further analyses of waveform characteristics at broadband stations in our study reveal discrete thin low-velocity layers between 1.7 and 4.3 km in the sedimentary structures in the southwest corner of the WCSB, which is adjacent to the eastern edge of the cordillera (i.e. CDF, Figure 5.6a). The thicknesses of the low-velocity layers range between 200 and 600 m. In the average recovered model of stations underlain by LVZs, the depths of the shallow and deep sedimentary LVZs are between 1.7 and 2.8 km, and between 3.8 and 4.3 km, respectively (Figure 5.6b).

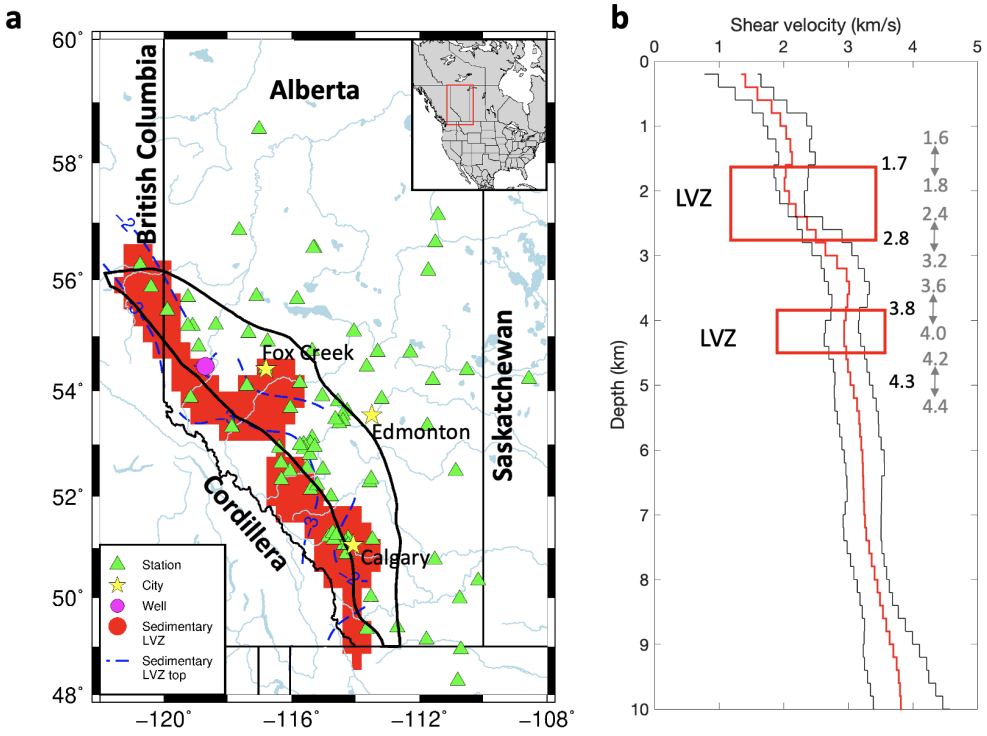

Figure 5.6. a. A map showing the distribution of sedimentary LVZ. Red shades represent the range of the sedimentary LVZ in our study. Blue dash lines delineate the depth of the top of interpolated low velocity layers. The black contour indicates the Alberta Basin, and the magenta circle marks the location of Well 11-27-64-5W6. **b.** The average shear wave velocity model (red) for stations underlain by LVZs. The red rectangles highlight the depths of the two LVZs. The numbers in black mark the average upper and lower boundaries of the LVZs. The numbers in gray denote the upper and lower boundaries of the LVZs from the selected stations. Black curves indicate the 1 standard deviation of the average velocity at each depth.

Inversion records indicate the inverted LVZs locate within the area of better fitness (Figure 5.7a, lower misfit values indicate the better inversions). Models of stations with and without LVZ also show clear differences (Figure 5.7b).

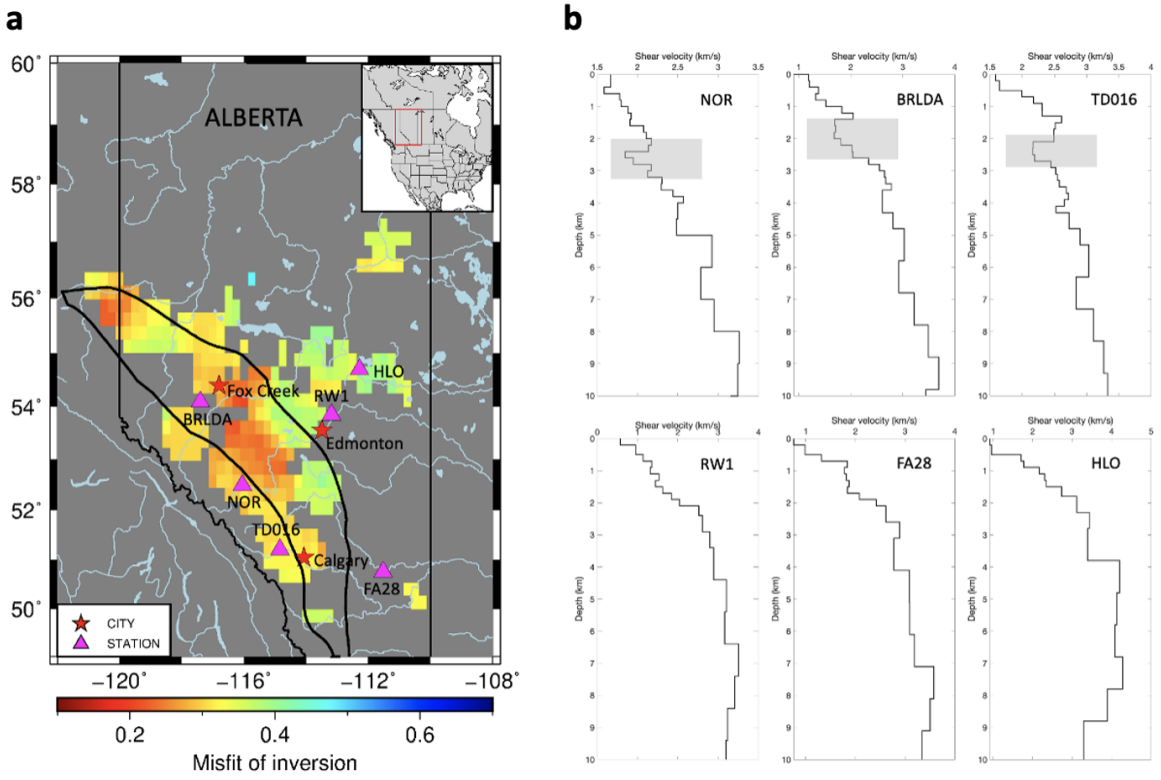

Figure 5.7. a. A map showing the values of misfit of inversion. Low misfit values (reddish) indicate good fitness of the inversion outcomes. High misfit values (bluish) indicate bad fitness of the inversion outcomes. **b**. Some inverted models of stations with (upper) and without (lower) LVZ. Shades indicate the potential range of LVZ.

5.3.2 Anomalous velocity zones in the upper-middle crust of the Western Laurentia

Our inversion results show obvious abnormal velocity zones in crustal structures from the central Alberta to the southwest, including a high velocity zone in the upper crust (Figure 5.8a) and a low velocity zone in the middle crust (Figure 5.8b). Stations with HVZ generally locate around the northwest of our study region and the stations with LVZ span from the northeast to the southwest of the Alberta Basin.

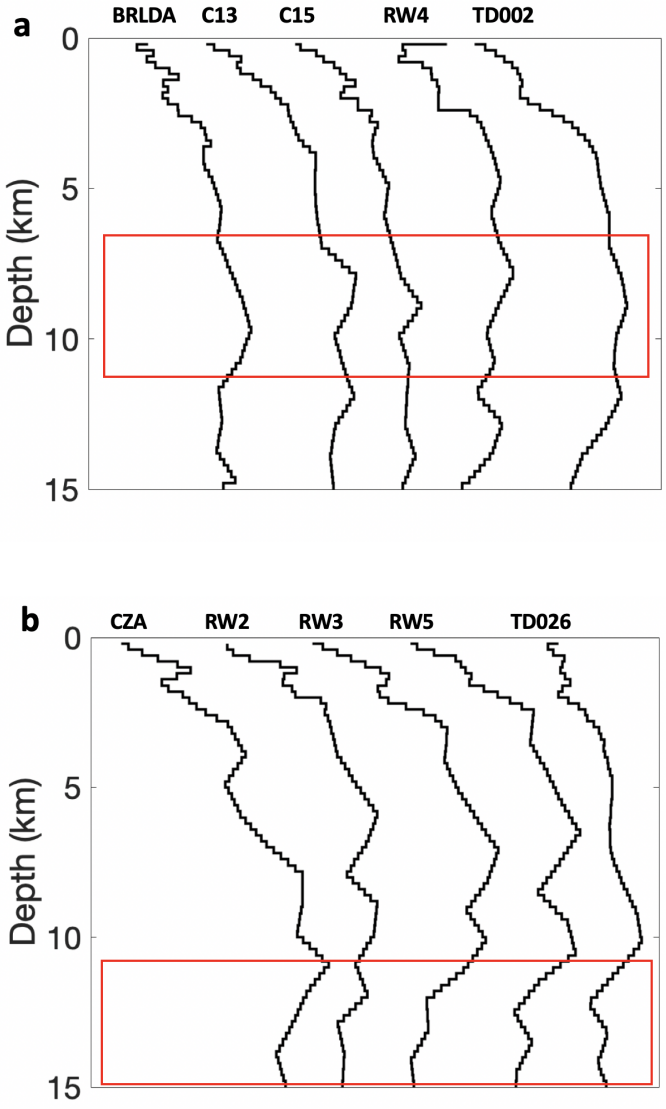

Figure 5.8. Inversion models (i.e. shear velocity models) of stations showing abnormal high (**a**) and low (**b**) shear velocity zones. Red rectangles roughly show the area of abnormal shear velocities.

Non-uniqueness is a well-documented characteristic of linear inversion of RFs. An inadequate initial model has significant influence on the solution of the inversion procedure, where an improper choice by machine may lead to a totally wrong local minimum (Ammon et al, 1990; Chen et al., 2015). To minimize the influence of the non-uniqueness, we performed non-linear inversion based on genetic algorithm, which is a global solution research technique aiming at reducing the effect of non-uniqueness.

A general LVZ exists beneath most stations at the depth of >12 km (Figure 5.8) with a relatively thin HVZ overlying this LVZ. This inevitable raises questions about the relationship between HVZ and LVZ and the reliability of our inverted models. To further verify our results, we performed some hypothesis tests on the basis of forward waveform simulation to quantify model biases as well as constrain HVZ and LVZ.

Firstly, we generate synthetic RFs by a simple gradient model with the depth from 0 to 20 km (the depth is zoomed in from 0 to 14 km in Figure 5.9). These RFs are subsequently subjected to the same inversion process as the actual observations. The shear velocities of the recovered model (Figure 5.9a) are ~0.16 km/s slower than the initial model at the crust. The extent of the recovery is reasonable, especially in view of the absence of notable artefacts of the crustal layers. The inverted model also preserves the main features of the initial model.

In the second test, we introduce a gradient model with a 3 km thick LVZ (0.3 km/s decrement of S-wave velocity) at the depth of 11 km (Figure 5.9d). Presumed shear velocity and spatial scale of the low-velocity layer resemble those of observed profiles beneath stations (see Figure 5.8b). In general, our inversion recovers ~92% of the peak energy of the input waveforms and the majority of the peaks and troughs of the simulated waveforms are properly resolved (Figure 5.9e and 5.9f). The inversion result from a variable shear wave velocity initial model as the first test successfully recovers the LVZ, which shows a ~0.26 km/s decrement of the shear wave velocity surrounding the LVZ in the given model. Our inverted model shows nearly identical shear velocity and spatial scales as the input and an overall correlation coefficient of 0.85 in spite of a relatively shallower

LVZ than our initial model. Furthermore, a relatively thin anomalous HVZ show as the artefacts overlies the recovered LVZ, even though no HVZ exists in the given model. Further tests on the existence of HVZ are conduct in Figure 5.12 and Figure 5.13.

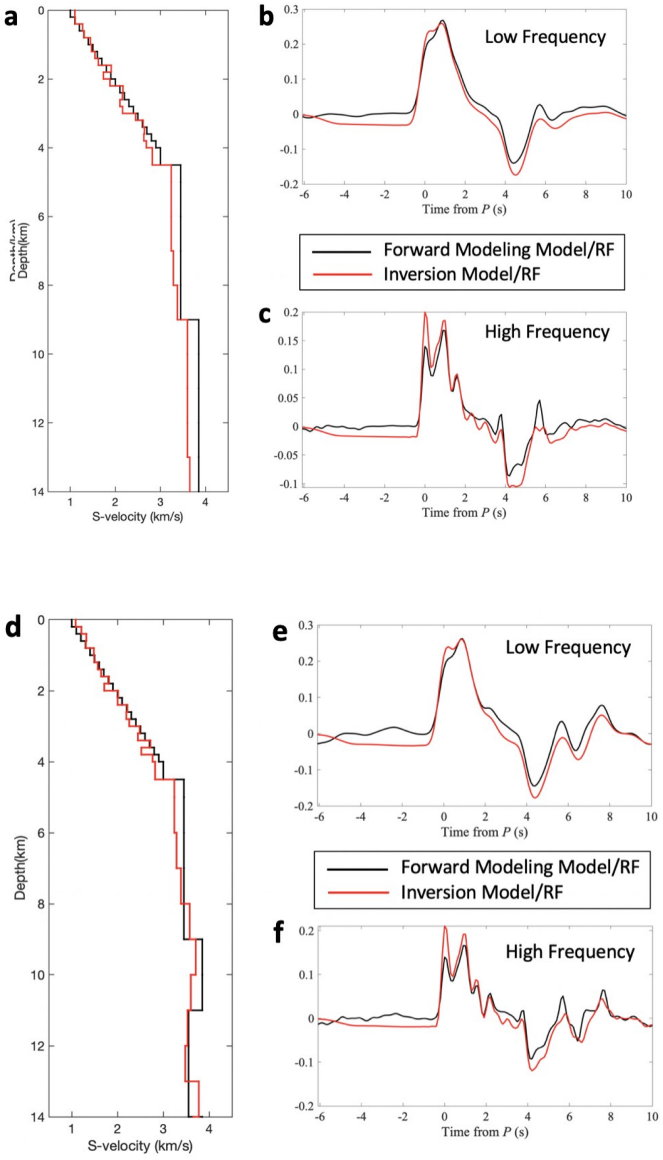

Figure 5.9. Results of waveform simulations and correspondent non-linear inversion outcomes. **a**. A model showing gradational structures (black) and the recovered optimal model (red). **b**. The waveform fitting result of the low frequency RF. The black line represents the RF by forward modeling, the red line represents the inverted RF. **c**. The waveform fitting result of the high frequency RF. **d**. A model showing LVZ exists at upper/middle crust (black) and the recovered model (red). **e** and **f**. The waveform fitting results of the low- and high- frequency RFs.

To further verify the robustness of our inversion results, we introduce a suite of models and compute the correspondent high frequency RFs (i.e. RFs with the Gaussian's factor as 5.0), aiming to assess the influence of different position and scales of LVZs on the simulated waveforms. Focusing on the changes of the crust, we set the sedimentary structures as a simple two-layer model with constant S-wave velocities. In the first simulation, we introduce a 3-km low-velocity layer with the decrement of 0.5 km/s in shear wave velocity at the depth of 10 km (Figure 5.10a Model 2). Phase 2 and phase 4 of the synthetic RF from Model 2 show obvious troughs and higher amplitudes than the simple gradient Model 1 (Figure 5.10b Model 2), which relates to the reduced consumption of energy by the LVZ. We further introduce another model (Figure 5.10a Model 3) with the decrement of S-velocity as 0.2 km/s (Figure 5.10a Model 3). Phase 2 and phase 4 of the synthetic RF from Model 3 still have higher amplitude than the synthetic RF from Model 1 but show relatively lower energy than the synthetic RF from Model 2. In the third simulation, we use one model with a LVZ with variable velocities (Figure 5.10a Model 4) at the same depth as Model 2 and Model 3. The amplitudes of phase 2 and phase 4 of the synthetic RF from Model 4 are between these phases from Model 2 and Model 3 (Figure 5.10b Model 4). In the last simulation test, we use a model with thinner LVZ (1 km) (Figure 5.10a Model 5) but the same decrement of velocity as Model 2. Waveform of the synthetic RF from Model 5 is similar to those from Model 2, Model 3 and Model 4, but the time difference between phase 2 and phase 1 is much closer, which is in consistency with the existence of thinner LVZ that leads to the decrease of the travel time between the upper and lower boundaries of this LVZ.

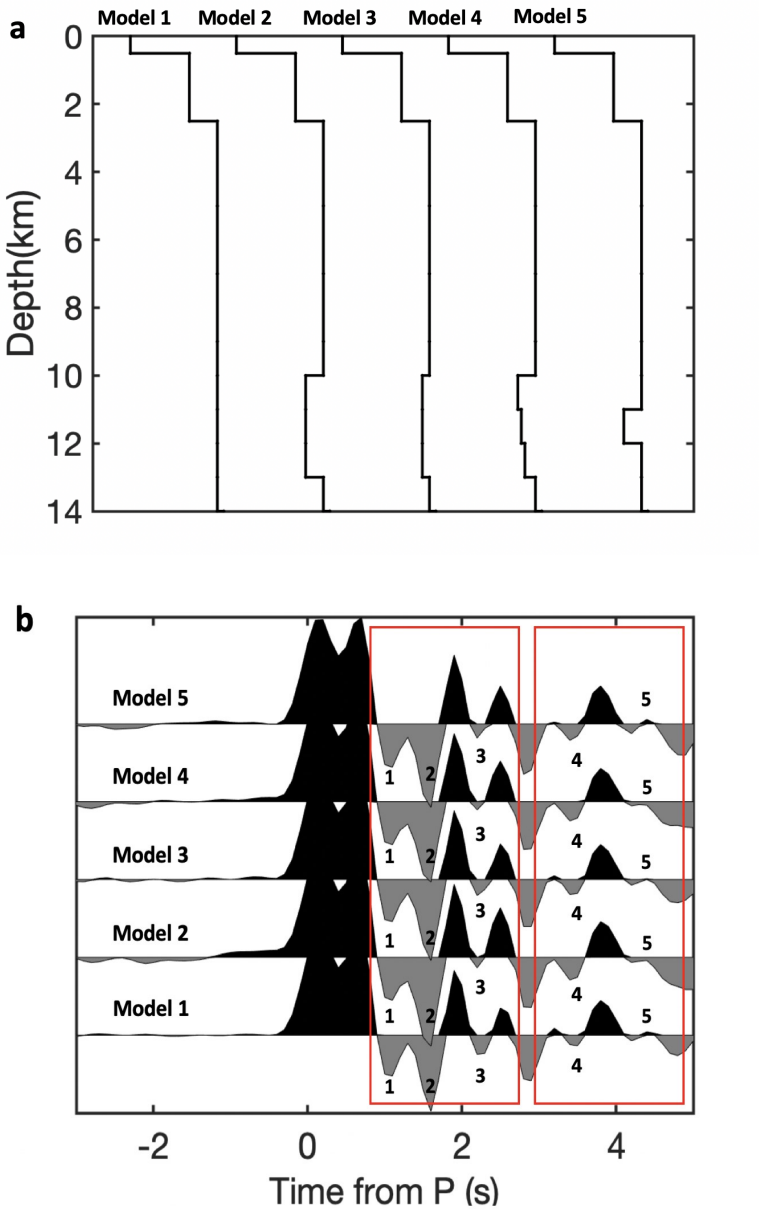

Figure 5.10. **a**. Input models with or without LVZs. Model 1 is a simple gradient model. Model 2 contains a LVZ with a relatively large-scale decrement. Model 3 contains a LVZ with a relatively small-scale decrement. Model 4 contains a LVZ with variable velocities. Model 5 contains a relatively thin LVZ. **b**. Five high-frequency RFs computed from the given models in **a**. The red rectangles show the significant differences of the waveforms from the 5 given models. Numbers (1, 2, 3, 4 and 5) indicate the phases that show changes.

In our study, the recorded high-frequency RFs are in consistency with the forward simulation tests to a great extent (Figure 5.11). Recorded high-frequency RFs from Station CZA, HON, PRDA, RW2, RW3 and RW5 show significant troughs at ~2-3 sec, suggesting the existence of LVZs. Disappearance of these phases on the waveform from station LYA may be caused by the existence of a LVZ with small decrement of shear wave velocity.

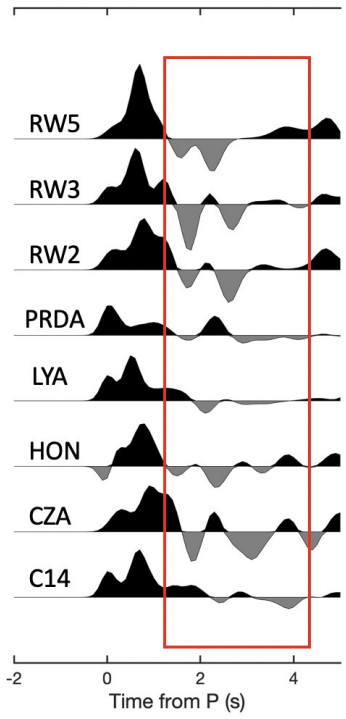

Figure 5.11. Stacked high frequency RFs of selected stations. Inverted model of station C14 does not show the presence of LVZ, the inverted models of the rest stations (CZA, HON, LYA, PRDA, RW2, RW3, RW5) show the presence of LVZ. The red rectangle indicates the phases showing differences.

To identify the existence of HVZ that overlie the confirmed LVZ, we perform forward simulations to further assess the necessity of the existence of HVZ in the upper crust, as well as its influence on the RFs. Similarly with the forward simulation tests for the existence of LVZ, firstly, we introduce a model without HVZ and compute the corresponding synthetic RF (Figure 5.12a and 5.12b Model 1). Subsequently, we introduce one model with a 3-km LVZ at the depth of 10 km

(the same one as Model 2 in Figure 5.10a) and another model with a 2-km HVZ (with the increment of 0.3 km/s) at the depth of 7 km (Figure 5.12a Model 2 and Model 3). Forward simulation results show that phase 2 and phase 4 dip more when LVZ exists (Figure 5.12b Model 2), however, amplitudes of these two phases decrease and phase 5 shows up when HVZ exists. This demonstrates the relatively contrary effects of LVZ and HVZ on RFs and indicates the possibility of the existence of HVZ.

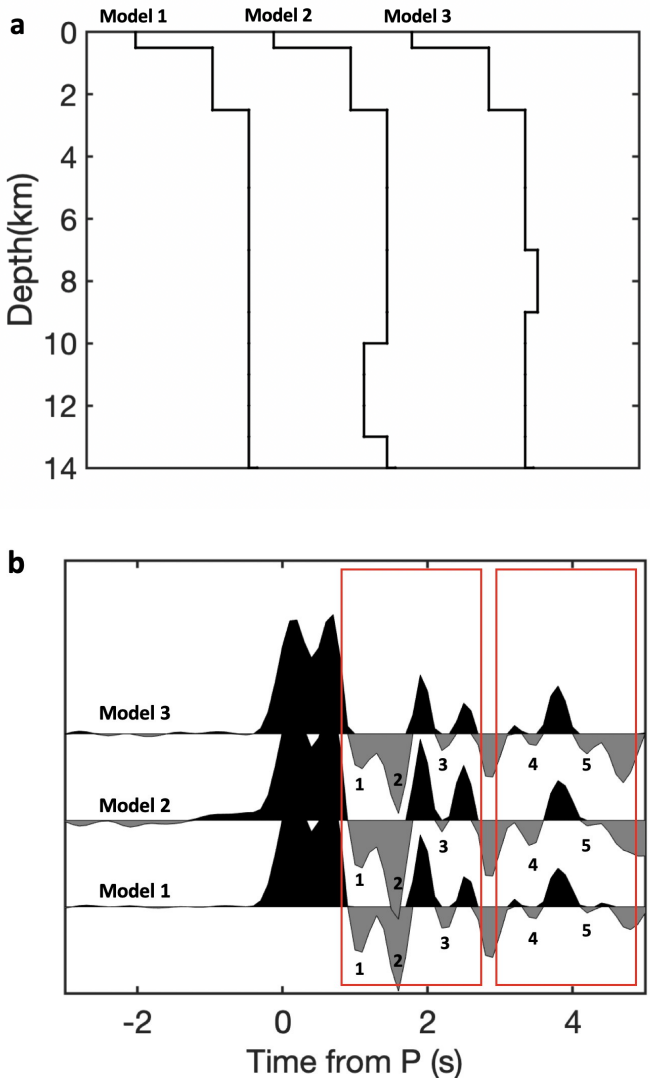

Figure 5.12. **a**. Three input models with LVZ or HVZ. Model 1 is a simple gradient shear wave velocity model. Model 2 contains a LVZ. Model 3 contains a HVZ. **b**. Correspondent high-frequency RFs computed from the models in **a**. Red rectangles show the significant differences of the waveforms from the 3 given models. Numbers (1, 2, 3, 4 and 5) indicate the phases showing changes.

To further verify the existence of HVZ, we perform several simulation tests on the position and scale of the HVZ. When a HVZ with 0.3 km/s increment of shear velocity is added in the upper crust at the depth of 7 km (Figure 5.13a Model 2), the absolute value of the amplitudes of phase 1 and 2 of the synthetic RF decreases but the amplitude of phase 5 of this RF increases (Figure 5.13b Model 2). We reduce the shear velocity increment of the HVZ to 0.15 km/s in Model 3 (Figure 5.13a). Changes of the amplitudes of phase 1, 2 and 5 of the simulated waveform from Model 3 comparing with the synthetic RF from Model 1 are much less than that from Model 2 (Figure 5.13b Model 3). If we introduce a thinner HVZ (1 km, Figure 5.13a Model 4), the corresponded synthetic RF shows a significant increase of the amplitude of phase 5 than previous models (Figure 5.13b Model 4). Finally, we introduce one model with a HVZ overlying a LVZ (Figure 5.13 Model 5), which resemble those of observed profiles beneath stations. The simulated waveform shows a decrease of the amplitude of phase 1 and an increase of the amplitude of phase 2. The arrival time of phase 2 and 4 is slightly advanced. The trend and shape of the synthetic RF of the last model with a HVZ overlying a LVZ are generally in consistency with the majority of the recorded RFs from our stations.

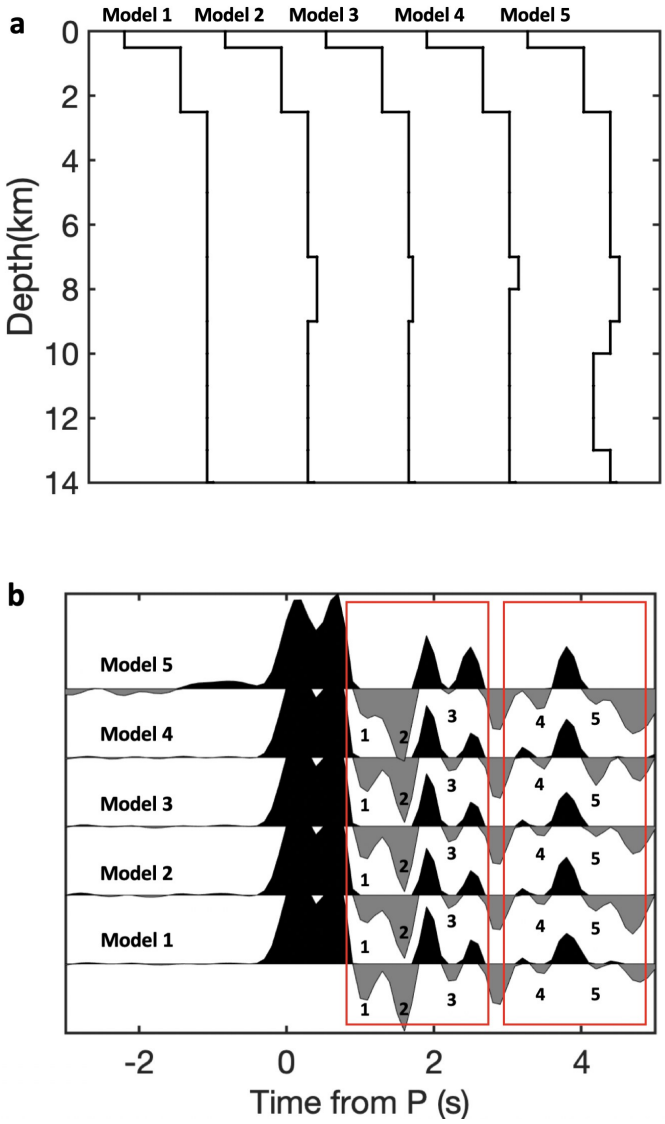

Figure 5.13. **a**. Input models with or without HVZs. Model 1 is a simple gradient model. Model 2 contains a HVZ with a relatively large-scale increment. Model 3 contains a HVZ with a relatively small-scale increment. Model 4 contains a relatively thin HVZ. Model 5 contains a HVZ overlying a LVZ. **b**. Five high frequency RFs computed from the given models in **a**. The red rectangles show the significant differences of the waveforms from the 5 given models. Numbers (1, 2, 3, 4 and 5) indicate the phases showing changes.

In the average recovered model of all stations, the depth of the crustal HVZ is between 7 and 11 km with the S-wave velocity over 3.5 km/s. When the depth is deeper than 11 km, our velocity profiles show a sharply negative gradient, indicating the existence of crustal LVZ (Figure 5.14a). In the average recovered model of stations underlain by crustal LVZs the depth of crustal LVZ

with a velocity decrement of ~0.5 km/s is between 10.9 and 14 km (Figure 5.14b). The thickness of the crustal LVZ is reported as 12 km by Chen et al. (2015). But because of the limit of the depth scale in our study, we are not able to recover crustal features deeper than 14 km. In the average recovered model of stations underlain by crustal HVZs, the depth of crustal HVZ with the S-wave velocity up to 3.9 km/s is between 7 and 10.7 km.

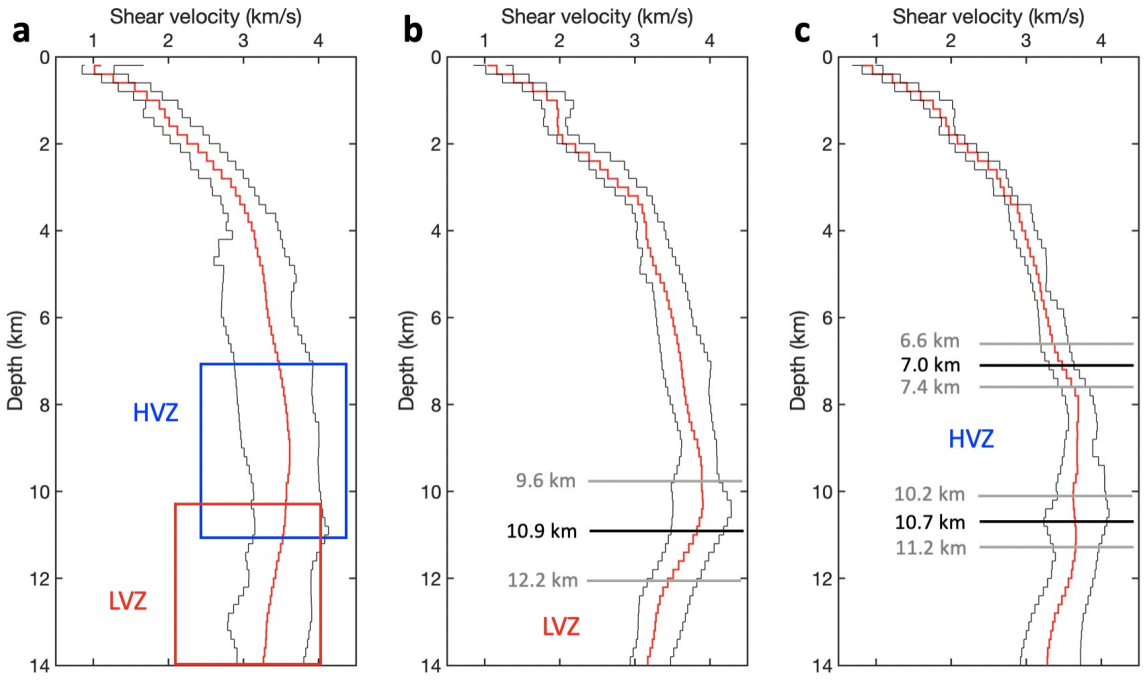

Figure 5.14. **a**. The average shear velocity model (red) of all broadband stations used in this study. Thin black curves indicate the 1 standard deviation of the average velocity at each depth. Blue and red rectangles indicate the positions of the HVZ and LVZ. **b**. The average shear wave velocity model (red) for stations underlain by LVZs. Horizontal black line marks the upper boundary of the LVZ. Gray lines mark the upper and lower boundaries of the top of LVZ. **c**. The average shear wave velocity model (red) for stations underlain by HVZs. Horizontal black line marks the upper and lower boundaries of the HVZ. Gray lines denote the upper and lower boundaries of HVZs from selected stations.

5.4 Discussion

5.4.1 Existence of sedimentary LVZs

The RFs recorded by broadband seismic networks shed new light on the sedimentary strata beneath southern-central Alberta. Among the key findings, the RF data reveal a distinctive low velocity structure along the Cordilleran Deformation Front (CDF). It is tempting to link this observation to the Cordilleran orogeny and development of the thrust-and-fold belt, where the presence of extensive networks of large-scale cracks and faults (Price, 1994) would lead to reduced seismic velocities (Yang & Zhu, 2010). However, the earlier-reported large-scale faults (Price, 1994) are mostly confined within the fold-and-thrust belt and do not extend eastward beyond the CDF where the LVZ resides. Furthermore, these faults consistently dip westward at high angles, whereas the LVZ in our models exhibits a significantly shallower (by 0.5 deg) dip.

Data from regional petroleum industry offers a more favorable explanation than collisional tectonics for the existence of the observed LVZs. According to the lithological data from AGS, Triassic, Permian and Devonian formations in southern-central Alberta (Figures 5.2a) are mainly composited of sandstone, limestone and dolostone, whereas middle Cretaceous and late Jurassic formations are dominated by shale and mudstone (Gradstein et al., 2004; Pana & Elgr, 2013; Prior et al., 2013). The inverted shear wave velocities of the LVZs range between 1.7 km/s – 2.6 km/s, which contrasts sharply with the those of the overlying cap rock (2.3 km/s to 3.3 km/s). The abundance of shale (2.3-3.7 km/s) and sandstone (1.3- 2.5 km/s) (Earle, 2015) could be responsible for the observed variations in velocity. Also, these sequences are evidence for a system involving a cap over a reservoir, which indicating the possible relation between the sedimentary LVZs and the oil and gas deposits. Previous well-logging results show that high total organic carbon content (TOC) exists in the depth range between 1.9 and 3.0 km (Well 11-27-64-5W6; Passey et al., 1990), at the same location of the observed LVZ (at 2-3 km depth) from RF inversions. Regional potential field observations lend further support for the inverted seismic velocities. For instance, the sedimentary LVZs revealed by RF inversions overlap with areas of known oil and natural gas

deposits, which commonly exhibit reduced density (shown as lower gravity, Figure 5.15a) and greater geomagnetic field while the subtle magnetic changes may be caused by the presence of extensive faults and cracks (Figure 5.15b).

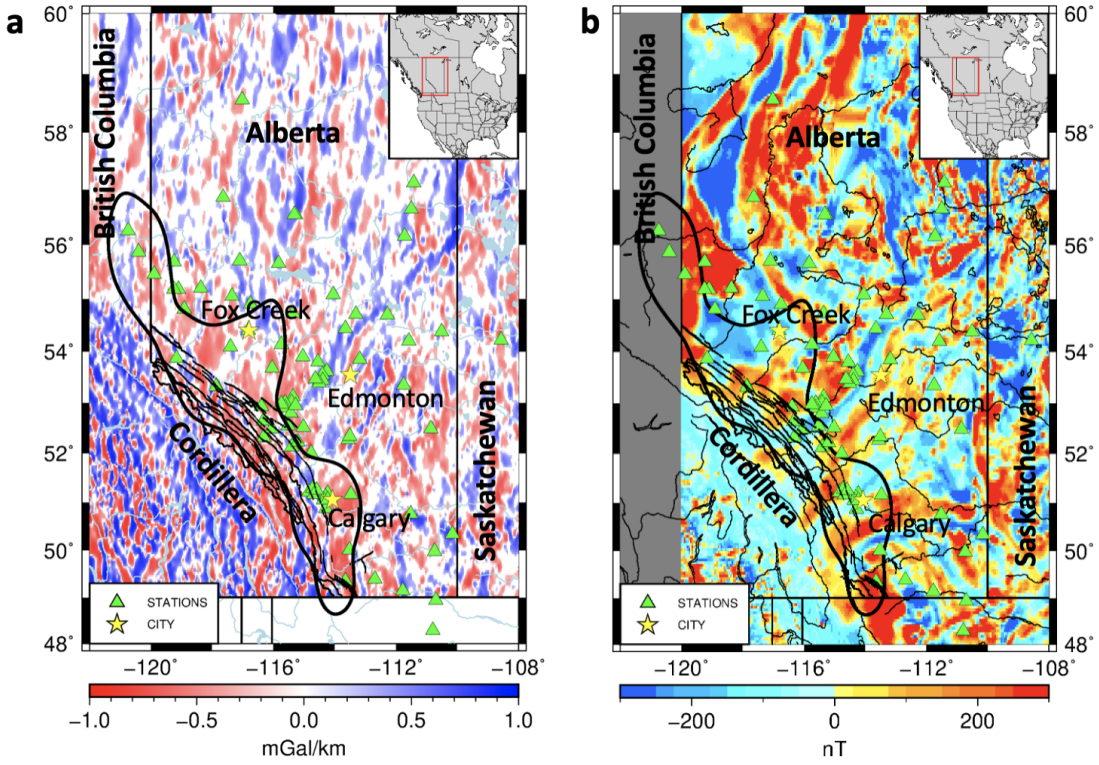

Figure 5.15. a. A map of horizontal gradient Bouguer gravity (modified from the data of NRCan). The thick black contour marks the boundaries of the sedimentary LVZs in our recovered models. Thin black lines along the cordillera mark the deformation front. **b**. A map of aeromagnetic data.

5.4.2 Existence of HVZ and LVZ in upper-middle crust

Seismic data recorded by broadband stations enable us to recover the structures beneath the central to southern WCSB. By RF imaging, we find distinctive low- and high- velocity structures in upper-mid crust.

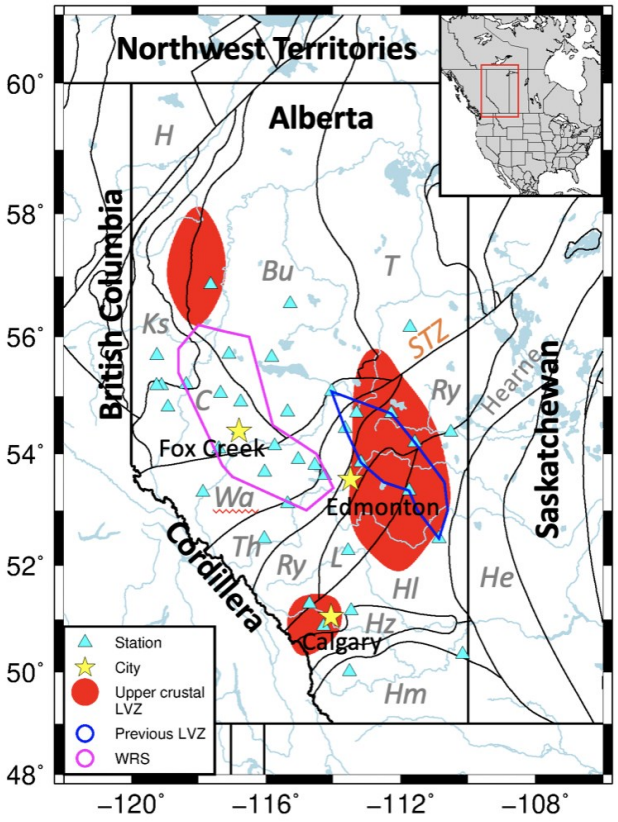

Figure 5.16. A map showing the distribution of crustal LVZ. Red shades represent the crustal LVZ in our study. The blue polygon indicates the LVZ location in previous studies. The magenta polygon indicates the Winagami reflection sequence (WRS). Thin black lines mark the tectonic domains. Abbreviations: Bu, Buffalo Head; C, Chinchaga; H, Hottah; He, Eyehill High; Hl, Loverna Block; Hm, Medicine Hat Block; Hz, Matzhiwin High; Ks, Ksituan; L, Lacombe Domain; Ry, Rimbey; STZ, Snowbird Tectonic Zone; T, Taltson; Th, Thorsby; Wa, Wabamun.

The continuous LVZ is along the depth from ~10.9 km to the lower boundary (14 km) of our models. Previous study by Chen et al. (2015) indicates that the mid-crustal LVZ is ~12 km thick from ~13.16 km to ~25.96 km, with one standard deviation of the upper boundary between 9.97 and 16.34 km, which is in consistency with our result that the upper boundary of mid-crustal LVZ is between 9.6 and 12.2 km. Meanwhile, the location of our crustal LVZ overlaps with that of previous discovered LVZ (Figure 5.16). A great deal of research has reported the existence of

crustal LVZ in the Alps (Mueller & Landisman, 1966), the Tibetan Plateau (Kind et al., 1996), the North China craton (Zheng et al., 2009), eastern-central Alberta in WCSB (Chen et al., 2015), and so forth. These discovered low velocity structures in crust with comparable scales in tectonic provinces provide hints of the tectonic history of western Laurentia. Four mechanisms for the possible generation of crustal LVZs in Alberta have been detailed by Chen et al. (2015), including the partial melting of the crust (Nelson et al., 1996), the serpentinization related with subduction (Eaton & Cassidy, 1996), the anisotropy (Zorin et al., 2002), and the granite intrusion (Masson et al., 1998; Bogdanova et al., 2006). Evidence suggests the intrusion of crystallized granite bodies is the plausible source for the existence of crustal LVZ. Our recovered velocity profiles further support this theory. According to the regional radiogenic heat flow distribution, our recovered crustal LVZs generally reside in high heat flow (>60 mW/m^2) regions in eastern-central Alberta, while stations without obvious crustal LVZs locate in low heat flow (<50 mW/m^2) regions (Figure 5.17). It has long been suggested that the spatial variation of heat flow could reflect variable degrees of granite intrusion into the basement (Bachu, 1988), which is further supported by the discovery of abundant granite-granitoids in drill core samples along the Rimbey magnetic arc (Ross et al., 1991). Further analysis about the granite-granitoids shows that the average shear velocity of this rock is ~3.596 km/s at the depth from 10 to 20 km, which is well within the uncertainties of average shear wave velocity values (3.50±0.30 km/s) of the observed LVZ from our inversion results. Analogues of this discovery of our study are the granite crustal LVZ discovered in the Variscan orogenic zone of southwest Ireland (Masson et al., 1998) and granitic rocks formed by the remelting of the upper crust discovered in the East European craton (Bogdanova et al., 2006).

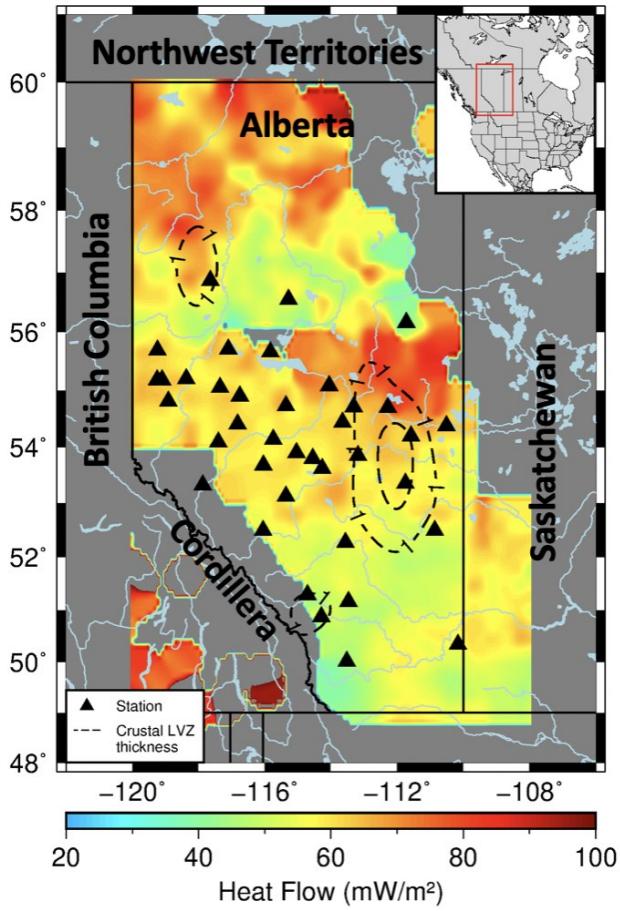

Figure 5.17. The upper crustal LVZ superimposed on a regional heat flow map (Majorowicz, 2018). The dash-line contours mark the thickness (in km) of the LVZ in our recovered models.

Based on previous studies on the crustal LVZ, granitic bodies in the crust beneath eastern-central Alberta is supported by the heat flow, the comparable shear wave velocity, and the ideal dual-subduction process for the generation of partial melting (Chen et al., 2015). Figure 5.18 shows the process of the formation of crustal LVZ. The middle crust underwent partial melting, and it could be enlarged further. Then the molten crust would crystalize and eventually form a granite crustal LVZ.

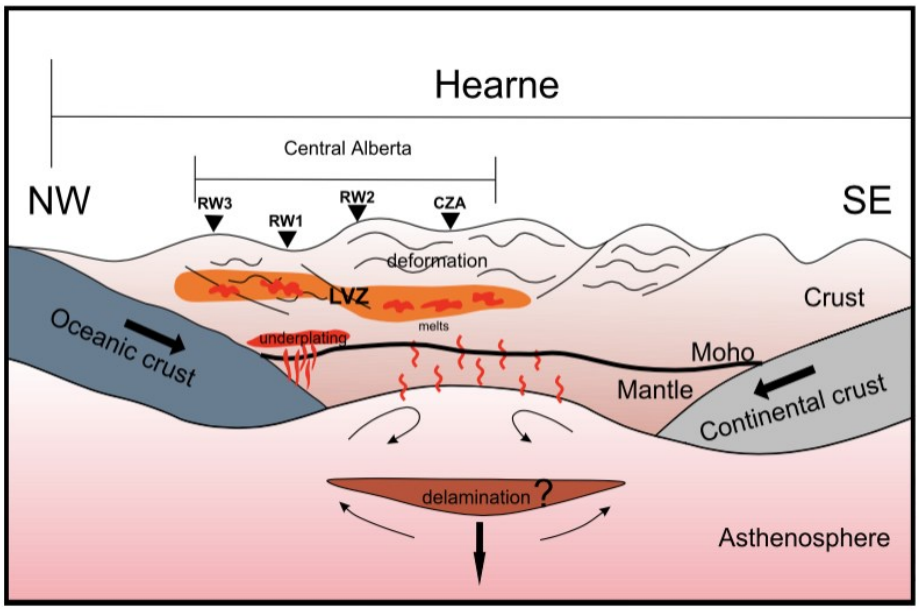

Figure 5.18. A schematic diagram demonstrating the major tectonic process that contributes to the presence of the crustal LVZ at eastern-central Alberta (Chen et al., 2015).

Differ from the discovered crustal LVZ, the HVZ overlying the crustal LVZ shows the characteristic of discreteness along the depth. Analysis of the location of discovered HVZ from our inverted models indicates the HVZ generally overlaps the well-known Winagami reflection sequence (WRS, Ross & Eaton, 1997; Welford & Clowes, 2006). Unlike gradational structures in simplified regional models (Bouzidi et al., 2002), the shear wave velocity in the average recovered model of stations underlain by HVZs exceeds 3.52 km/s between 7.0 and 10.7 km in the upper crust, which is in consistency with the reported WRS, then it shows a relatively sharp negative gradient to the lower boundary of our inverted models (14 km, Figure 5.14c). The shear wave velocity of the crustal HVZ in the average model of stations underlain by HVZs is ~0.45 km/s higher than the velocity at the same depth of the average model of stations underlain by LVZs. Stations underlain by discrete HVZs in upper crust generally reside in the Wabamun, Chinchaga and Ksituan domains (Figure 5.19). A mafic sill complex intrusion offers the explanation of the existence of HVZs in Wabamum and Chinchaga domains (Ross & Eaton, 1997; Welford & Clowes, 2006). The intrusions of numerous subhorizontal sills with dolerites can increase the bulk velocity and form high velocity structures (Welford & Clowes, 2006). A regional extensive magmatism mostly evidenced as vertical dyke intrusions during the convergence of the Slave and Rae

provinces (Ross & Eaton, 1997) is also likely responsible for the existence of HVZs. Our estimates of the depth of observed HVZs are highly consistent with the depth range of the WRS (6.5-16.5 km) proposed by Ross and Eaton (1997). Surficial projection of the crustal LVZ and HVZ suggests a related position that the HVZ partially covers the LVZ. This geometry indicates the consequence of horizontal and vertical intrusions during the magmatism and subsequently partial melting in the crust.

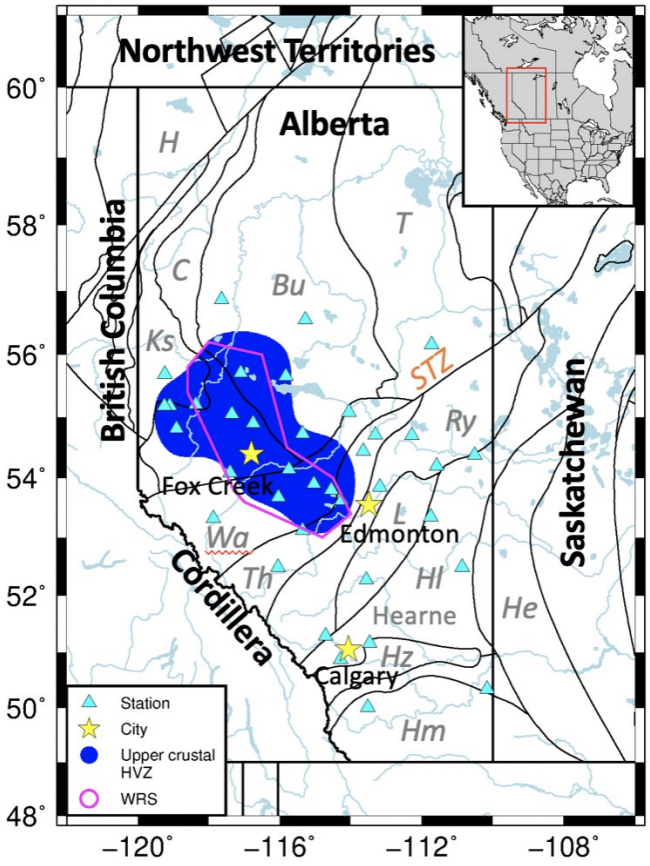

Figure 5.19. A map showing the distribution of crustal HVZ. The blue shade represents the crustal HVZ in our study. The magenta polygon indicates the location of the WRS. Thin black lines mark the tectonic domains. Abbreviations: Bu, Buffalo Head; C, Chinchaga; H, Hottah; He, Eyehill High; Hl, Loverna Block; Hm, Medicine Hat Block; Hz, Matzhiwin High; Ks, Ksituan; L, Lacombe Domain; Ry, Rimbey; STZ, Snowbird Tectonic Zone; T, Taltson; Th, Thorsby; Wa, Wabamun.

5.4.3 Reconstruction of sedimentary structures

The Precambrian crystalline basement of the WCSB is characterized by a gentle southwestward dip from 3-4 km beneath central Alberta to ~6 km beneath the foothill, the latter of which was caused by the compression and thickening of the near-surface part of the continental margin during the Cordilleran orogeny. The morphology of the sedimentary strata is direct evidence for the convergence between the accreted terranes and the North American craton. Specifically, the weight of compressed and thickened parts of the Cordillera and sediments during the orogeny induced the subsidence of the WCSB, gradually forming an east-tapering wedge (Figure 5.20).

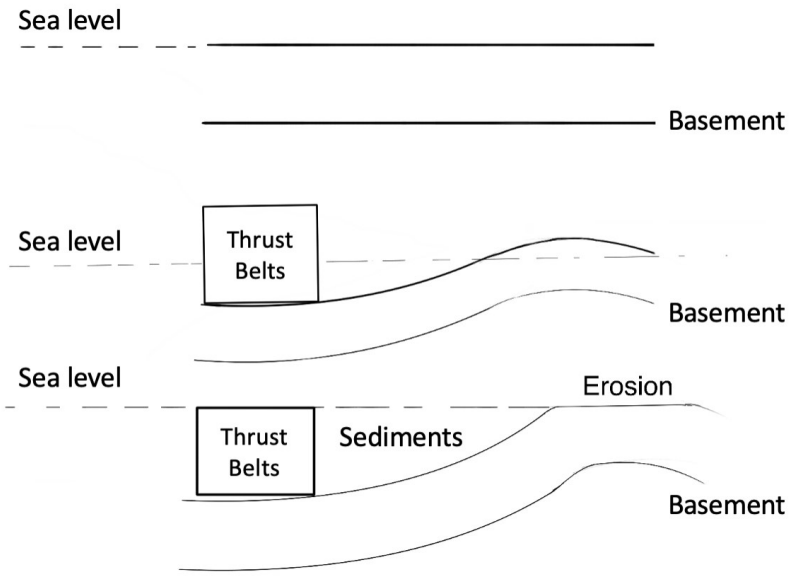

Figure 5.20. A schematic west-to-east cross-section showing the deformation of the Precambrian crystalline basement in the WCSB during the evolution process.

The RF imaging by broadband seismic networks provide further supports for the recovery of sedimentary structures. Since the vertical dimension (defined by basement depth) is much smaller than the lateral extent of the West-to-East cross-section (see Figure 4.6a in Chapter 4), we make a simplifying assumption that changes near the surface (i.e., erosion and weathering) have only minor influences on the tectonic process. We then adopt a 'stripping-away' method (Zheng et al.,

2005) to reconstruct the geometry of the strata from Precambrian to Quaternary (Figure 5.21), as well as the historical basement subsidence (Figure 5.22a), by extracting the geological implications from our west-to-east shear velocity profile. When we focus on one stratum, we strip away the layers above it by applying an S-velocity threshold from previous models (Figure 5.2) derived from well-logs and our inversions, which is to remove the profile with velocity less than the threshold; this approach effectively takes a snapshot of the velocities at a certain geological time. Through multiple peeling processes, we are able to provide a quantitative, 'frame-by-frame' reconstruction of tectonic evolution of the WCSB.

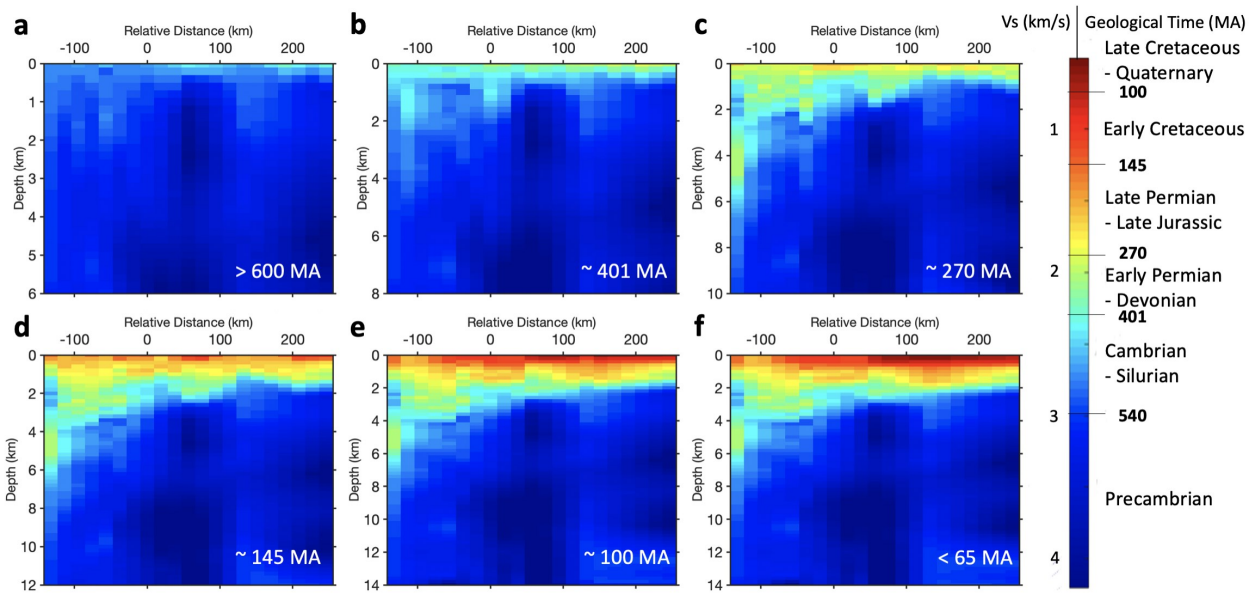

Figure 5.21. West-to-east cross-sections of shear wave velocity reformed to reconstruct the geometry features belonging to different strata from ~600 Ma to the present. The X-axis of each plot represents the relative distance at the same spatial scales as those of Figure 4.6a in Chapter 4.

First, as the main driving force, the tectonic subsidence of the WCSB made major impact on the evolution of the Cordillera (Rohais, et al., 2018). From the Precambrian to the Silurian, the shear velocity profile shows parallel deposits and a slight depression (Figure 5.21a and 5.21b, Figure

5.22aI), which could be attributed to Cambrian-Silurian rifting and the formation of a passive margin. Moving forward in time, from the late Cambrian to early Permian (~401 – ~270 Ma), the Devonian extension and the subsequent convergence from the Pennsylvanian to early Permian initiated the eastward-dipping subduction (Price, 1994; Monger & Price, 2002), showing both a westward dip in the shear velocity cross-section (Figure 5.21c) and a high average rate of the basement depth increase (Figure 5.22aII). Meanwhile, the retro-arc foreland basin to the east of the Cordillera began to develop. In the late Jurassic, nearly flat curve on the historical basement subsidence map (Figure 5.22aIII) suggests extensive horizontal surficial deposition and an uplift of the basement (Figure 5.21d), mainly in response to the Farallon subduction and the ensuing isostatic rebound (Murphy et al., 2006; Liu et al., 2008; Rohais et al., 2018). From the late Jurassic to Eocene, the WCSB experiences the foreland basin stage. According to our reconstructed models (Figure 5.21e and 5.21f), wedge-top and foredeep depozones initiated during this period and eventually formed the two significant depozones of the foreland basin system. The weight of the displaced and tectonically thickened structures above the crust induced the subsidence of the retro-foreland basin (Beaumont, 1981) and the basement subsidence curve shows accelerated dipping rates (Figure 5.22aIV-V). Interestingly, deposits during the foreland basin stage, which took place less than 160 Ma ago, are notably absent from the interpreted geological time sequence in our reconstructed models. Possible causes are (1) detachment and (2) extrusion and erosion of older deposits, which eventually integrated into the younger deposits (Price, 1994).

Our RF-based reconstruction of the historical basement subsidence curve is consistent with the buried history curves of Well 8-17-53-21W4 in the Alberta Basin (Nurkowski, 1985; Kalkreuth & McMechan, 1988; Osadetz et al., 1990; Wright et al., 1994; Figure 5.22). To facilitate comparison, we compute the depths by averaging the cluster (Figure 5.1. round grey shade) closest to Well 8-17-53-21W4. Despite minor differences, likely affected by the resolution limit of the RFs, the subsidence rates, depths and trends of these two approaches reach an outstanding correlation coefficient of 0.92. The consistency between the basement subsidence curve derived from the RF inversion and that from well-logs shows a glimpse of the outstanding potential of multiple-station RF inversions in future basement evolution modeling (Figure 5.22c). While well-logging data remain ‘ground-truths’, our new seismologically based approach is substantially more cost-effective in the investigation of the spatiotemporal evolution of sedimentary basins worldwide.

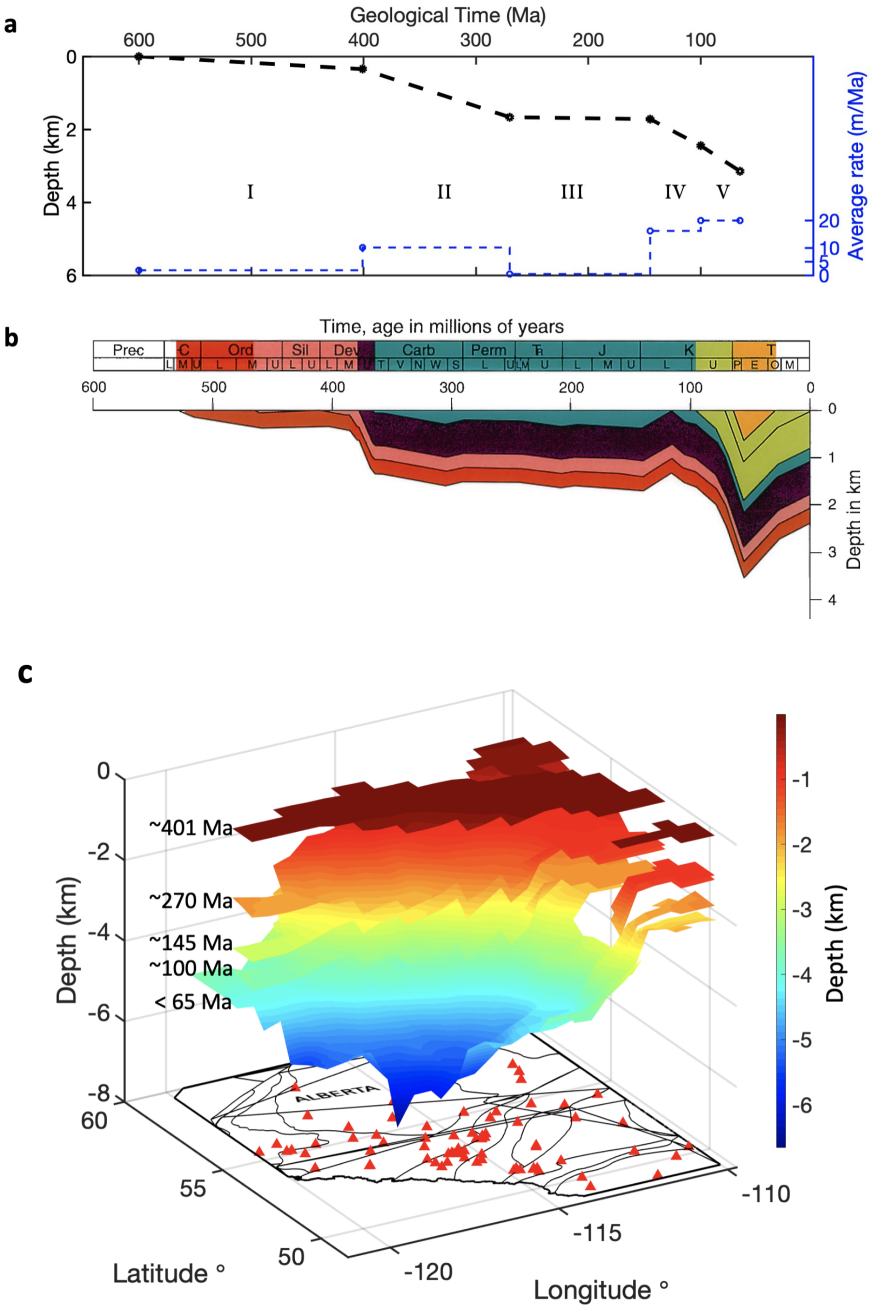

Figure 5.22. a. Basement subsidence curve of the Alberta Basin derived from 'stripping-away' method. The black dash line indicates the general trend of the basement subsidence depth changes, and the blue dash line shows the average rate of the subsidence process between different geological times. **b**. Burial history curves of the Alberta Basin based on Well 8-17-53-21W4 (Wright et al., 1994). **c**. 3D model of the subsidence process of the Alberta Basin. Black lines on the bottom plate delineate the province border and tectonic domains. Red triangles represent the stations.

5.5 Conclusion

The recovery of anomalous velocity bodies and the understanding of tectonic history of the WCSB are crucial for both geophysical and geological research. In this chapter, we adopt the RF imaging introduced in Chapter 4 to model the sedimentary and upper crustal features. Using global earthquakes, we are able to recover the abnormal shear wave velocity structures in the sedimentary strata and upper-middle crust (in connection with tectonic deformation, crustal chemistry and lithology). The sedimentary LVZs are interpreted as abundant sandstones and limestones in Triassic, Permian and Devonian formations in southern-central Alberta and/or oil and natural gas deposits. The crustal LVZ relates to the granite intrusion during the dual-subduction process for the generation of partial melting and underplating. The crustal HVZs generally overlap the WRS, which is long believed to be caused by mafic sill complex intrusion. Our inversions further constrain the positions of the crustal abnormal velocity bodies to reveal the consequence of horizontal and vertical intrusions during the magmatism and subsequently partial melting in the crust. Our findings also enable us to reconstruct the tectonic history of the Precambrian basement. This study sheds new light on the initiation and evolution of the WCSB, and provides further supports for the discovered tectonic features in the WCSB.

Chapter 6. Conclusions

Sedimentary and crustal structures of the WCSB are prime examples of the complex tectonic history of the evolution of North America. Their retrieval has both scientific and practical importance, as structural understanding have direct implications for the exploration and development of fossil fuel resources. In this thesis we adopt the passive seismic survey and use RFs, which are highly sensitive to subsurface and crustal changes in impedance, depth and V_p/V_s ratio. Seven broadband seismic station networks were used to map the seismic structures of shallow parts at different depth levels in the Alberta Basin. The imaging approach based on RFs have been one of the backbones in the seismological community in the past 30+ years in mapping the interior structures and dynamics of the Earth. The list below summarizes the observations and interpretations based on our studies in each chapter.

Chapter 4 provides constraints for the basement between the sedimentary strata and upper crust by combination RF analysis and the *H*-κ stacking. We introduce a joint non-linear inversion based on genetic algorithm to minimize the non-uniqueness effects. By qualitative and quantitative tests, we verify the consistency and robustness of our model and offer an updated map with largely improved resolution than CRUST 1.0, which also meets the Precambrian basement map from AGS by well-loggings and explorations. The improved shear velocity profiles provide further supports for future study in this area.

Chapter 5 details the findings derived from our RF-based inversions and develops a basin formation model. Our inversions reveal thin and discrete low-velocity layers in southwestern Alberta at depths between 1.7 and 4.3 km. Explanations of the genesis of the sedimentary LVZ focus on (1) cracks and faults caused by deformation along the thrust-and-fold belt of the cordillera and (2) the formation of sedimentary strata and the existence of organic carbon content, which is preferred in our study. Our inversion also provides further supports for the existence of anomalous velocity zones in the upper crust. Robust observations in our study shows the presence of relatively thin and discrete HVZs in the upper crust, corresponding to the reported WRS by Ross and Eaton

(1997) as a mafic sill intrusion, as well as the presence of a broad upper-middle crustal LVZ, corresponding to the reported mid-crustal LVZ by Chen et al. (2015) as a granite intrusion. Both anomalies suggest the tectonic process of extensive subduction, orogenesis, magmatism and metamorphism, and crustal melting during the Precambrian assembly of the North American craton. Finally, we introduce a "layer-stripping" method to reconstruct the sedimentary strata based on RF inversion, which shed new light on more recent evolutionary history of the WCSB.

In conclusion, key findings of my studies are: (1) the recovery of both the basement depth and the S-velocities within the sedimentary strata and upper crust, and the establishment of a new S-velocity model of the Alberta Basin with improved resolution; (2) the recovery and explanation of abnormal velocity bodies from the sedimentary strata to the crust; (3) the reconstruction of the tectonic history of the Precambrian basement. The resolved range of depths (0-14 km) effectively bridges the gap between the vertical scales of well-logging (0-6 km) and those of traditional broadband analysis (>10 km) involving receiver functions and surface waves.

Our studies on the shallow parts of WCSB provide a different perspective on the research of the supracrustal structures in large scale rather than the exploration seismic survey and well-drilling. The newly built shear velocity model with largely improved resolution of the Alberta Basin can provide detailed information of the supracrustal structures for future studies. A community model of the integration of results from body waves, surface waves, anisotropic variations, compressional and shear wave velocities, exploration seismic data, and general geophysical data (i.e. gravity, magnetic, and electric data) can greatly improve the understanding of regional tectonics and contribute to the industrial production of fossil resources. Dataset analyzed in our studies, as well as shear velocity models of the sedimentary and upper crustal structures, are significant and integral components of this community model of the tectonic development of the western North American continent.

In this dissertation, I discussed my studies on the seismic imaging of the sedimentary and crustal structures of the Alberta Basin in the WCSB by introducing a method combining the joint RF

inversion based on GA and the *H*-κ stacking. This method largely improves the capability of RF inversions in discerning and constraining subsurface layers. It sheds new light on the studies focusing on the shallow part of the Earth (i.e. sedimentary strata), especially some areas that are short of data from well-loggings and seismic explorations. Although our method has improved stability and flexibility of recovering the shallower subsurface structures, the limited resolution of RF inversions, the sensitivity of Poisson's ratios (or Vp/Vs ratios) to rock's properties, the selection of initial models, and the complex fault and crack systems in the CDF (i.e. fold-and-thrust belt) still have significant influence on the efficiency of the inversions and cause uncertainties of our final S-velocity model. To solve these problems, future studies could focus on two aspects: (1) the improvement of the Poisson's ratio and the RF inversion resolution to discern thinner sedimentary layers, for instance, we could adopt more sonic logging data to construct a more accurate initial model for the inversions; and (2) the improvement of the RF inversion by introducing a method to inverting the subsurface slopes rather than horizontal interfaces, in order to fully map the complex structures in the CDF of the Rocky Mountains.

Bibliography

Abers, G. A. (2005). Seismic low-velocity layer at the top of subducting slabs: Observations, predictions, and systematics, Phys. Earth Planet. Inter., 149(1), 7–29.

Abt, D. L., Fischer, K. M., French, S. W., Ford, H. A., Yuan, H., & Romanowicz, B. (2010). North American lithospheric discontinuity structure imaged by Ps and Sp receiver functions. Journal of Geophysical Research: Solid Earth, 115(B9).

Agius, M., Rychert, C. A., Harmon, H., & Laske, G. (2017). Mapping the mantle transition zone beneath Hawaii from Ps receiver functions: Evidence for a hot plume and cold mantle downwellings. Earth and Planetary Science Letters, 474, 226-236.

Aki, k., & Lee, W. H. K. (1976). Determination of three-dimensional velocity anomalies under a seismic array using first P arrival times from local earthquakes: 1. A homogeneous initial model. Journal of Geophysical Research, 81, 4381-4399.

Aki, K., & Richards, P. G. (2002). Quantitative Seismology, Second Edition. University Science Books.

Allen, P. A., Homewood, P., & Williams, G. (1986). Foreland Basins: An Introduction. International Association of Sedimentologists, 3–12.

Ammon, C. J. (1991). The isolation of receiver effects from teleseismic P waveforms. Bulletin of the Seismological Society of America, 81(6), 2504 – 2510. https://doi.org/10.1785/BSSA0810062504

Ammon, C. J., Randall, G. E., & Zandt, G. (1990). On the nonuniqueness of receiver function inversions. Journal of Geophysical Research, 95(B10), 15303-15318. http://doi.org/10.1029/JB095iB10p15303

Bachu, S. (1993). Basement heat flow in the Western Canada sedimentary basin. Tectonophysics, 222(1), 119-133.

Backus, G. E., & Gilbert, J. F. (1967). Numerical applications of a formalism for geophysical inverse problems. Geophysical Journal International, 13(1-3), 247-276. https://doi.org/10.1111/j.1365-246X.1967.tb02159.x

Backus, G. E., & Gilbert, J. F. (1968). The resolving power of gross earth data. Geophysical Journal International, 16(2), 169-205. https://doi.org/10.1111/j.1365-246X.1968.tb00216.x

Bally, A. W., Gordy, P. L., & Stewart, G. A. (1966). Structure, seismic data and orogenic evolution of the southern Canadian Rockies. Bulletin of Canadian Petroleum Geology, 14, 337-381.

Baltzer, F., & Purser, B. H. (1990). Moden alluvial fan deltaic sedimentation in a foreland tectonic setting: the lower Mesopotamian Plain and the Arabian Gulf. Sediment. Geol., 67, 175-197.

Bao, X., & Eaton, D. W. (2015). Large variations in lithospheric thickness of western Laurentia: Tectonic inheritance or collisional reworking? Precambrian Research, 266, 579–586. http://hdl.handle.net/1880/51113

Bao, X., Eaton, D. W., & Gu, Y. J. (2016). Rayleigh wave azimuthally anisotropic phase velocity maps beneath western Canada. Journal of Geophysical Research: Solid Earth, 121(3), 1821–1834. https://doi.org/10.1002/2015JB012453

Bastow, I., Stuart, G., Kendall, J., & Ebinger, C. (2005). Upper-mantle seismic structure in a region of incipient continental breakup: northern Ethiopian rift. Geophys. J. Int., 162, 479-493.

Beasley, D., Bull, D. R. & Martin, R. R. (1993). An overview of Genetic Algorithms: Pt1, Fundamentals. University Computing archive 15 (1993), 58-69.

Beaumont, C. (1981). Foreland basins. Geophysical Journal of the Royal Astronomical Society, 65(2), 291 – 329.

Beck, S. L., & G. Zandt, G. (2002). The nature of orogenic crust in the central Andes. Journal of Geophysical Research: Solid Earth (1978-2012), 107(B10), ESE-7.

Ben-Zion, Y., & Aki, K. (1990). Seismic radiation from an *SH* line source in a laterally heterogeneous planar fault zone. *Bulletin of the Seismological Society of America*, 80 (4), 971–994.

Bernasconi, G., & Drufuca, G. (1990). Rays and reflectivity: an intermediate approach. SEG Annual Meeting 1990, 1012. https://doi.org/10.1190/1.1889894

Bezacier, L., Reynard, B., Bass, J. D., Sanchez-Valle, C., & Van de Moortele, B. (2010). Elasticity of antigorite, seismic detection of serpentinites, and anisotropy in subduction zones. Earth an Planetary Science Letters, 289(1-2), 198-208.

Boerner, D. E., Kurtz, R. D., Craven, J. A., Ross, G. M., & Jones, F. W. (2000). A synthesis of electromagnetic studies in the Lithoprobe Alberta Basement Transect: constraints on Paleoproterozoic indentation tectonics. Canadian Journal of Earth Sciences, 37(11), 1509–1534. https://doi.org/10.1139/e00-063

Bogdanova, S., et al. (2006). EUROBRIDGE: new insight into the geodynamic evolution of the East European Craton. Geological Society, London, Memoirs. 32. 599-625.

Boschi, L., Becker, T. W., & Steinberger, B. (2007). Mantle plumes: Dynamic models and seismic images. Geochemistry, Geophysics, Geosystems, 8(10).

Bostock, M. G. (1996). A seismic image of the upper mantle beneath the North American craton. Geophysical Research Letters, 23(13), 1593-1596.

Bostock, M. G. (2013). The Moho in subduction zones. Tectonophysics, 609, 547–557. https://doi.org/10.1016/j.tecto.2012.07.007

Bouzidi, Y., Schmitt, D. R., Burwash, R. A., & Kanasewich, E. R. (2002). Depth migration of deep seismic reflection profiles: crustal thickness variations in Alberta. Canadian Journal of Earth Sciences, 39(3), 331–350. https://doi.org/10.1139/e01-080

Boyer, S. E., & Elliott, D. (1982). Thrust systems. Bull. Am. Ass. Petrol. Geol., 66, 1196-1230.

Bradley, D. C., & Kusky, T. M. (1986). Geologic evidence for rate of plate convergence during the Taconic arc-continent collision. J. Geol., 94, 667–681.

Branscombe, P., MacCormack, K. E., Corlett, H., Hathway, B., Hauck, T. E., & Peterson, J. T. (2018). 3D Provincial Geological Framework Model of Alberta, version 1 (dataset, multiple files). Alberta Energy Regulator, AER/AGS Model 2017-03.

Broome, J. (1990). Generation and interpretation of geophysical images with examples from the Rae province, northwestern Canada Shield. Geophysics, 55, 977-997.

Burdick, L. J., & Langston, C. A. (1977). Modeling crustal structure through the use of converted phases in teleseismic body-wave forms, Bulletin of the Seismological Society of America, 67(3), 677--691.

Burgess, P. M., Gurnis, M., & Moresi, L. (1997). Formation of sequences in the cratonic interior of North America by interaction between mantle, eustatic, and stratigraphic processes. GSA Bull., 108 (12), 1515–1535.

Burwash, R. A., & Culbert, R. R. (1976). Multivariate geochemical and mineral patterns in the Precambrian basement of western Canada. Canadian Journal of Earth Sciences, 13, 1-18. https://doi.org/10.1139/e76-001

Burwash, R. A., & Krupricka, J. (1969). Cratonic reactivation in the Precambrian basement of western Canada, I: Deformation and chemistry. Canadian Journal of Earth Sciences, 6, 1381-1396. https://doi.org/10.1139/e69-140

Burwash, R. A., & Krupricka, J. (1970). Cratonic reactivation in the Precambrian basement of western Canada, II: Metasomatism and isostacy. Canadian Journal of Earth Sciences, 7, 1275-1295. https://doi.org/10.1139/e70-120

Burwash, R. A., Krupicka, J., Basu, A. R., & Wagner, P. A. (1985). Resetting of Nd and Sr whole-rock isochrons from polymetamorphic granulites, northeastern Alberta. Canadian Journal of Earth Science, 22, 992-1000.

Burwash, R. A., Krupricka, J., & Wijbrans, J.R. (2000): Metamorphic evolution of the Precambrian basement of Alberta. Canadian Mineralogist, 38, 423–434.

Burwash, R. A., McGregor, C. R., & Wilson, J. (1994). Precambrian Basement Beneath the Western Canada Sedimentary Basin, Geological atlas of the Western Canada Sedimentary Basin. Compiled by GD Mossop and I. Shetsen. Canadian Society of Petroleum Geologists and Alberta Research Council, Calgary, Alta, 49 – 56.

Burwash, R. A., & Power, M. A. (1991). Trout Mountain anomaly, northern Alberta: its role in the northwest foreland of the Trans-Hudson orogen. Geological Survey of Canada, Special Paper, 37, 301-311.

Cant, D. J., & Stockmal, G. S. (1989). The Alberta foreland basin: relationship between stratigraphy and Cordilleran terrane-accretion events. Canadian Journal of Earth Sciences, 26(10), 1964–1975.

Carpenter, E. (1965). A historical review of seismometer array development. Proc IEEE, 53, 1816-1821.

Cassidy, J. F. (1992). Numerical experiments in broadband receiver function analysis. Bulletin of the Seismological Society of America, 82(3), 1453-1474.

Catuneanu, O. (2004). Retroarc foreland systems—evolution through time. Journal of African Earth Science, 38, 225-242.

Chacko, T., De, S. K., Creaser, R. A., & Muehlenbachs, K. (2000). Tectonic setting of the Taltson magmatic zone at 1.9-2.0 Ga: a granitoid-based perspective. Canadian Journal of Earth Sciences, 37(11), 1597–1609.

Chen, L., & Ai, Y. (2009). Discontinuity structure of the mantle transition zone beneath the North China Craton from receiver function migration. Journal of Geophysical Research: Solid Earth, 114(B6).

Chen, Y., Gu, Y. J., Dokht, R. M. H., & Sacchi, M. D. (2015). Crustal imprints of Precambrian orogenesis in western Laurentia. Journal of Geophysical Research: Solid Earth, 120(10), 6993 – 7012. https://doi.org/10.1002/2014JB011353

Chen, Y., Gu, Y. J., & Hung, S. H. (2017). Finite-frequency P-wave tomography of the Western Canada Sedimentary Basin: Implications for the lithospheric evolution in Western Laurentia. Tectonophysics, 698, 79–90. https://doi.org/10.1016/j.tecto.2017.01.006

Chen, Y, Gu, Y. J. & Hung, S.-H. (2018). A new appraisal of lithospheric structures of the Cordillera-craton boundary region in western Canada, Tectonics,37(9), 3207-3228.

Chen, Y., Gu, Y. J., Heaman, L., Wu, L., Saygin, E., & Hung, S.-H. (2020). Reconciling seismic structures and Late Cretaceous kimberlite magmatism in northern Alberta, Canada. Geology, 48.

Chester, F., Evans, J. & Biegel, R. (1993). Internal Structure and Weakening Mechanisms of the San-Andreas Fault. Journal of Geophysical Research. 98. 771-786.

Chmielowski, J., Zandt, G., & Haberland, C. (1999). The Central Andean Altiplano-Puna magma body, Geophys. Res. Lett., 26(6), 783–786.

Christopher, J. E. (1990). Notes on the Sweetgrass Arch – Mesozoic tectonics and sedimentation. University of Alberta, extension Department, Banff Earth Science Conference.

Clayton, R. W., & Wiggins, R. A. (1976). Source shape estimation and deconvolution of teleseismic bodywaves. Geophysical Journal of the Royal Astronomical Society, 47(1), 151-177.

Clitheroe, G., Gudmundsson, O., & Kennett, B. L. N. (2010). Sedimentary and upper crustal structure of Australia from receiver functions. Australian Journal of Earth Sciences, 47(2), 209-216. https://doi.org/10.1046/j.1440-0952.2000.00774.x

Clowes, R. M. (2010). Initiation, development, and benefits of Lithoprobe - Shaping the direction of Earth science research in Canada and beyond. Canadian Journal of Earth Sciences. 47. 291-314. https://doi.org/10.1139/E09-074

Clowes, R. M., Burianyk, M. J., Gorman, A. R., & Kanasewich, E. R. (2002). Crustal velocity structure from SAREX, the Southern Alberta Refraction Experiment. Canadian Journal of Earth Sciences, 39(3), 351–373. https://doi.org/10.1139/e01-070

Clowes, R. M., Zelt, C. A., Amor, J. R., & Ellis, R. M. (1995). Lithospheric structure in the southern Canadian Cordillera from a network of seismic refraction lines. Canadian Journal of Earth Sciences, 32(10), 1485–1513.

Coakley, B. J., & Watts, A. B. (1991). Tectonic controls on the development of unconformities: the North Slope, Alaska. Tectonics, 10, 101-130.

Collerson, K. D., Van Schmus, R. W., Lewry, J. F., & Bickford, M. E. (1988). Buried Precambrian basement in south-central Saskatchewan: provisional results from Sr-Nd model ages and U-Pb zircon geochronology. Saskatchewan Energy and Mines, Miscellaneous Report, 88(4), 142-150.

Coney, P. J., Munoz, J. A., McClay, K. R., & Evenchick, C. A. (1996). Oligocene syntectonic burial and Miocene posttectonic exhumation of the southern Pyrenees foreland fold-thrust belt. J. geol. Soc., 153(1), 9-16.

Conn, A. R., Gould, N. I. M. & Toint, Ph. L. (1991). A Globally Convergent Augmented Lagrangian Algorithm for Optimization with General Constraints and Simple Bounds. SIAM Journal on Numerical Analysis, 28(2), 545-572.

Conn, A. R., Gould, N. I. M. & Toint, Ph. L. (1997). A Globally Convergent Augmented Lagrangian Barrier Algorithm for Optimization with General Inequality Constraints and Simple Bounds. Mathematics of Computation, 66(217), 261-288.

Corrigan, D., Pehrsson, S., Wodicka, N., & de Kemp, E. (2009). The Palaeoproterozoic Trans-Hudson Orogen: a prototype of modern accretionary processes. Geological Society, London, Special Publications, 327(1), 457–479.

Covey, M. (1986). he evolution of foreland basins to steady state: evidence from the western Taiwan foreland basin. Spec. Publ. Int. Ass. Sed., 8, 77–90.

Crampton, S. L., & Allen, P. A. (1995). Recognition of forebulge unconformities associated with early stage foreland basin development: Example from the North Alpine Foreland Basin. AAPG Bulletin, 79 (10), 1495–1514.

Creaney, S., & Allan, J. (1990). Hydrocarbon generation and migration in the Western Canada Sedimentary Basin. Classic Petroleum Provinces. J. Brooks (ed.). Special Publication of the Geological Society, Blackwell Scientific.

Creaney, S., Allan, J., Cole, K. S., Fowler, M. G., & Brooks, P. W. (1994). Petroleum Generation and Migration in the Western Canada Sedimentary Basin. Geological atlas of the Western Canada Sedimentary Basin. Compiled by GD Mossop and I. Shetsen. Canadian Society of Petroleum Geologists and Alberta Research Council, Calgary, Alta, 455-468.

Currie, B. S. (1994). 'Back-bulge' to foredeep evolution of the Late Jurassic-Early Cretaceous Cordilleran foreland basin: Evidence from the Morrison and Cedar Mountain Formations, central-eastern Utah. Abst. Progs. Geol. Soc. Am. 26, no. 6.

Davis, G. A., Monger, J. W. H., & Burchfiel, B. C. (1978). Mesozoic construction of the Cordilleran "collage", central British Columbia to central California. Mesozoic paleogeography of the western United States. Pacific Coast Paleogeography Symposium 2. D. G. Howell and K. A. McDougall (eds.). Pacific Section, Society of Economic Paleontologists and Mineralogists, 1-32.

Davis, L. (1990). Genetic algorithm and simulated annealing. London: Pitman.

Davis, W. J., Berman, R., Kjarsgaard, B., & Ross, G. M. (1995). U–Pb geochronology and isotopic studies of crustal xenoliths from the Archean Medicine Hat block, northern Montana and southern Alberta: Paleoproterozoic reworking of Archean crust. In Alberta Basement Transects Workshop: Lithoprobe Report, 47, 330–335.

DeCelles, P. G. (1994). Late Cretaceous-Paleocene synorogenic sedimentation and kinematic history of the Sevier thrust belt, northeast Utah and southwest Wyoming. Bull. Geol. Soc. Am., 106, 32-56.

DeCelles, P. G., & Burden, E. T. (1992). Non-marine sedimentation in the overfilled part of the Jurassic-Cretaceous Cordilleran foreland basin: Morrison and Cloverly Formations, central Wyoming, USA. Basin Res., 4, 291–314.

DeCelles, P. G., & Giles, K. (1996). Foreland Basin Systems. Basin Research, 8(2), 105-123.

DeCelles, P. G., & Hertel, F. (1989). Petrology of Fluvial Sands, from the Amazonian Foreland Basin, Peru and Bolivia. Geological Society of American Bulletin, 101(12), 1552-1562.

Dewey, J. F., & Bird, J. M. (1970). Mountain belts and the new global tectonics, J. Geophys. Res., 75, 2625-2647.

Dickinson, W. R. (1974). Plate tectonics and sedimentation. Geol. Paleont., 22, 1-27.

Dickinson, W. R. (1976). Sedimentary basins developed during evolution of Mesozoic-Cenozoic arc- trench system in western North America, Can. J. Earth Sci., 13, 1268-1287.

Dickinson, W. R. (2004). Evolution of the North American Cordillera. Annual Review of Earth and Planetary Sciences, 32(1), 13–45.

Dickinson, W. R., & Suczek, C. A. (1979). Plate tectonics and sandstone compositions. American Association of Petroleum Geologists' Bulletin, 63, 2164-2182.

Dilek, Y., & Furnes, H. (2014). Ophiolites and Their Origins. Elements, 10, 93-100.

Dods, S. D., Teskey, D. J., & Hood, P. J. (1989). Magnetic anomaly map of Canada. Geological Survey of Canada, Canadian Geophysical Altas, Map 11, Scale 1:10000000.

Dokht, R. M. H., Gu, Y. J., & Sacchi, M. D. (2016). Waveform inversion of SS precursors: An investigation of the northwestern Pacific subduction zones and intraplate volcanoes in China. Gondwana Research, 40, 77-90. https://doi.org/10.1016/j.gr.2016.07.006

Dor, O., Rockwell, T.K. & Ben-Zion, Y. (2006). Geological Observations of Damage Asymmetry in the Structure of the San Jacinto, San Andreas and Punchbowl Faults in Southern California: A Possible Indicator for Preferred Rupture Propagation Direction. Pure appl. geophys., 163, 301–349.

Dueker, K. G., & Sheehan, A. F. (1997). Mantle discontinuity structure from midpoint stacks of converted P to S waves across the Yellowstone hotspot track. Journal of Geophysical Research: Solid Earth (1978-2012), 102(B4), 8313-8327.

Duan, Y., Tian, X., Liang, X., Li, W., Wu, C., Zhou, B., & Iqbal, J. (2017). Subduction of the Indian slab into the mantle transition zone revealed by receiver functions. Tectonophysics, 702, 61-69.

Dziewonski, A. M., & Anderson, D. L. (1981). Preliminary reference Earth model. Physics of the earth and planetary interiors, 25(4), 297 – 356. https://doi.org/10.1016/0031-9201(81)90046-7

Earle, S. (2015). Physical Geology. BCcampus.

Eaton, D. W., & Cassidy, J. F. (1996). A relic Proterozoic subduction zone in western Canada: New evidence from seismic reflection and receiver function data. Geophysical Research Letters, 23(25), 3791–3794. https://doi.org/10.1029/96GL03619

Eaton, D. W., Ross, G. M., & Clowes, R. M. (1999). Seismic-reflection and potential- field studies of the Vulcan structure, western Canada: A Paleoproterozoic Pyrenees? Journal of Geophysical Research, 104(B10), 23255. https://doi.org/10.1029/1999JB900204

Eaton, D. W., Ross, G. M., & Hope, J. (1999). The rise and fall of a cratonic arch: A regional seismic perspective on the Peace River Arch, Alberta. Bulletin of Canadian Petroleum Geology, 47(4), 346–361.

Ekstrom, G., & Dziewonski, A. M. (1998). The unique anisotropy of the Pacific upper mantle. Nature, 394, 168-172.

Evan, J. P., & Chester, F. M. (1995). Fluid-rock interaction and weakening of faults of the San Andreas System: interfaces from San Gabriel fault-rock geochemistry and microstructures. Journal of Geophysical Research, 100(B7), 13007-13020.

Evenchick, C. A. (1991). Geometry, evolution, and tectonic framework of the Skeena fold belt, north – central British Columbia. Tectonics, 10, 527-546. https://doi.org/10.1029/90TC02680

Ewing, T. E. (1980). Paleogene tectonic evolution of the Pacific Northwest. Journal of Geology, 88, 619-638. https://doi.org/10.1086/628551

Fischer, K. M. (2002). Waning buoyancy in the crustal roots of old mountains. Nature, 417(6892), 933-936.

Flemings, P. B., & Jordan, T. E. (1989). A synthetic stratigraphic model of foreland basin development. J. geophys. Res., 94, 3851–3866.

Fountain, D.M., Boundy, T.M., Austrheim, H. & Rey, P. (1994). Eclogite facies shear zones—deep crustal reflectors. Tectonophysics, 232, 411–424.

Frederiksen, A. W., Bostock, M. G., & Cassidy, J. F. (2001). S-wave velocity structure of the Canadian upper mantle. Physics of the Earth and Planetary Interiors, 124(3-4), 175–191.

Funck, T., Louden, K. E., & Reid, I. D. (2000). Wide-angle seismic imaging of a Mesoproterozoic anorthosite complex: the Nain Plutonic Suite in Labrador, Canada. Journal of Geophysical Research: Solid Earth, 105(B11), 25693-25707.

Gaherty, J. & Revenaugh, J. (2003). Collaborative Research: Canadian Northwest Seismic Experiment [Data set]. International Federation of Digital Seismograph Networks. https://doi.org/10.7914/SN/XN_2003

Gao, S. S., & Liu, K. H. (2014). Mantle transition zone discontinuities beneath the contiguous United States. Journal of Geophysical Research: Solid Earth, 119(8), 6452–6468.

Gerhard, L. C., Anderson, S. B., & Fischer, D. W. (1990). Petroleum geology of the Williston Basin. American Association of Petroleum Geologists, 51, 507-559.

Gilbert, H. (2012). Crustal structure and signatures of recent tectonism as influenced by ancient terranes in the western United States. Geosphere, 8(1), 141–157.

Giles, K. A., & Dickinson, W. R. (1995). The interplay of eustasy and lithospheric flexure in forming stratigraphic sequences in foreland settings: an example from the Antler foreland, Nevada and Utah. Spec. Publ. SEPM, 52, 187–211.

Goldberg, D. E. (1989). Genetic algorithms in search, optimization and machine learning. Addison-Wesley Longman Publishing C., Inc.

Gradstein, F. M., & Ogg, J. G. (2020). A Geologic Time Scale 2004. Cambridge Univ. Press, 589.

Grefenstette, J. J. (1987). Genetic algorithms and their applications. Psychology Press.

Gu, Y. J. (2010). Arrays and array methods in global seismology. Springer, Netherland.

Gu, Y. J., Chen, Y., Dokht, R. M. H., & Wang, R. (2018). Precambrian Tectonic Discontinuities in Western Laurentia: Broadband Seismological Perspectives on the Snowbird and Great Falls Tectonic Zones. Tectonics, 37(5), 1411 – 1434.

Gu, Y. J., Dziewonski, A. M., Su, W., & Ekström, G. (2001). Models of the mantle shear velocity and discontinuities in the pattern of lateral heterogeneities, J. Geophys. Res., 106, 11169-11199.

Gu, Y. J., Okeler, A., Shen, L., & Contenti, S. (2011). The Canadian Rockies and Alberta Network (CRANE): New constraints on the Rockies and western Canada sedimentary basin [Data set]. Seismological Research Letters, 82(4), 575–588. https://doi.org/10.1785/gssrl.82.4.575

Gu, Y. J., & Shen, L. (2015). Noise correlation tomography of Southwest Western Canada Sedimentary Basin. Geophysical Journal International, 202(1), 142–162. https://doi.org/10.1093/gji/ggv100

Gu, Y. J., Zhang, Y., Sacchi, M. D., Chen, Y., & Contenti, S. (2015). Sharp mantle transition from cratons to Cordillera in southwestern Canada. Journal of Geophysical Research: Solid Earth, 120(7), 5051–5069.

Gurnis, M. (1992). Rapid continental subsidence following the initiation and evolution of subduction. Science, 255, 1556–1558.

Gurrola, H., & Minster, J. B. (1998). Thickness estimates of the upper-mantle transition zone from bootstrapped velocity spectrum stacks of receiver functions, Geophysical Journal International, 133(1), 31–43.

Hanssen, P. (2011). Passive seismic methods for hydrocarbon exploration. 73 EAGE Conference and Exhibition incorporating SPE EUROPEC 2011.

Hassanat, A., Almohammadi, K., Alkafaween, E., Abunawas, E., Hammouri, A., & Prasath, V. B. S. (2019). Choosing mutation and crossover ratios for genetic algorithms – a review with a new dynamic approach. Information 2019, 10, 390.

Haupt, R. L., & Haupt, S. E. (2004). Practical Genetic Algorithm. Second edition. John Wiley & Sons, New Jersey.

Heaman, L. M., Kjarsgaard, B. A., & Creaser, R. A. (2004). The temporal evolution of North American kimberlites. Lithos, 76(1–4), 377–397.

Herbaly, F. L. (1974). Petroleum geology of the Sweetgrass Arch, Alberta. American Association of Petroleum Geologists Bulletin, 58, 2227-2245.

Hoffman, P. F. (1988). United Plates of America, The Birth of a Craton: Early Proterozoic Assembly and Growth of Laurentia. Annual Review of Earth and Planetary Sciences, 16(1), 543–603.

Hoffman, P. F. (1989). Precambrian geology and tectonic history of North America. The Geology of North America, A, 447–512. https://doi.org/10.1130/DNAG-GNA-A.447

Holland, J. H. (1975). Adaption in natural and artificial system. The MIT Press.

Holt, W. E., & Stern, T. A. (1994). Subduction, platform subsidence, and foreland thrust loading: the late Tertiary development of Taranaki basin, New Zealand. Tectonics, 13, 1068–1092.

Hope, J., & Eaton, D. (2002). Crustal structure beneath the Western Canada sedimentary basin: Constraints from gravity and magnetic modelling. Canadian Journal of Earth Sciences, 39(3), 291–312. https://doi.org/10.1139/e01-060

Hopper, E., & Fischer, K. M. (2015). The meaning of midlithospheric discontinuities: A case study in the northern US craton. Geochemistry, Geophysics, Geosystems, 16(12), 4057–4083.

Immanuel, S. D. & Chakraborty, U. K. (2019). Genetic Algorithm: An Approach on Optimization. 2019 International Conference on Communication and Electronics Systems (ICCES), 701-708.

Ingersoll, R. V., Graham, S. A., & Dickinson, W. R. (1995). Remnant ocean basins. In: Tectonics of Sedimentary Basins (Ed. by C. J. Busby & R. V. Ingersoll). Blackwell Science, Oxford, 363–393.

IRIS Transportable Array. (2003). USArray Transportable Array [Data set]. International Federation of Digital Seismograph Networks.

Jacobi, R. D. (1981). Peripheral bulge-a causal mechanism for the Lower Ordovician unconformity along the western margin of the northern Appalachians. Earth Plan. Sci. Let., 56, 245–251.

Jagoutz, O., & Kelemen, P. B. (2015). Role of arc process in the formation of continental crust.Annu. Rev. Earth Planet. Sci. 2015, 43, 363-404.

James, D. E., Niu, F., & Rokosky, J. (2003). Crustal structure of the Kaapvaal craton and its significance for early crustal evolution. Lithos, 71(2), 413-429.

Jordan, T. E. (1981). Thrust loads and foreland basin evolution, Cretaceous, western United States. Bull. Am. Ass. petrol. Geol., 65, 2506–2520.

Jordan, T. E. (1995). Retroarc Foreland and Related Basins, Tectonics of Sedimentary Basins. Blackwell Scientific Publications, 331-362.

Kalkreuth, W., & McMechan, M. E. (1988). Burial history and thermal maturity, Rocky Mountain Front Ranges, Foothills and Foreland, east-central British Columbia and adjacent Alberta, Canada. American Association of Petroleum Geologists, Bulletin, 72, 1395-1410. https://doi.org/0.1306/703c99b0-1707-11d7-8645000102c1865d

Karner, G. D., & Watts, A. B. (1983). Gravity anomalies and flexure of the lithosphere at mountain ranges. J. geophys. Res., 88, 10449–10477.

Kay, S. M., Ramos, V. A., Mpodozis, C., & Sruoga, P. (1989). Late Paleozoic to Jurassic silicic magmatism at the Gondwana margin: Analogy to the Middle Proterozoic in North America? Geology, 17(4), 324–328.

Kent, D. M. (1987). Paleotectonic controls on sedimentation in the Northern Williston Basin, Saskatchewan. AAPG Rocky Mountain Section meeting, 67(8).

Kent, D. M., & Christopher, J. E. (1994). Geological history of the Williston Basin and Sweetgrass Arch, Geological atlas of the Western Canada Sedimentary Basin. Compiled by GD Mossop and I. Shetsen. Canadian Society of Petroleum Geologists and Alberta Research Council, Calgary, Alta, 421-429.

Kennett, B. L. N., Engdahl, E. R., & Buland, R. (1995). Constraints on seismic velocities in the Earth from traveltimes. Geophysical Journal International, 122(1), 108-124.

Kind, R., Ni, J., Zhao, W., Wu, J., Yuan, X., Zhao, L., Sandvol, E., Reese, C., Nabelek, J., & Hearn, T. (1996). Evidence from earthquake data for a partially molten crustal layer in southern Tibet. Science, 274(5293), 1692-1694.

Kind, R., Yuan, X., & Kumar, P. (2012). Seismic receiver functions and the lithosphere-asthenosphere boundary. Tectonophysics, 536, 25–43.

Kirkpatrick, S., Gelatt, C. D., & Vecchi, M. P. (1983). Optimization by simulated annealing. Science, 220, 671-680.

Krueger, H. E., Gama, I., & Fischer, K. M. (2021). Global patterns in cratonic mid-lithospheric discontinuities from Sp receiver functions. Geochemistry, Geophysics, Geosystems, 22(6).

Landes, M., Ritter, J., O'Reilly, B., Readman, P., & Do, V. (2006). AN-S receiver function profile across the Variscides and Caledonides in SW Ireland. Geophysical Journal International, 166(2), 814-824.

Langston, C. A. (1979). Structure under Mount Rainier, Washington, inferred from teleseismic body waves, Journal of Geophysical Research: Solid Earth (1978-2012), 84(B9), 4749-4762.

Laske, G., Masters, G., Ma, Z., & Pasyanos, M. (2013). Update on CRUST1.0 - A 1-degree global model of Earth's crust. In Geophys. Res. Abstr, 15, 2658.

Laubscher, H. P. (1978). Foreland folding. Tectonophysics, 47, 325-337.

Lawrence, J. F., and Shearer, P. M. (2006). A global study of transition zone thickness using receiver functions, Journal of Geophysical Research: Solid Earth (1978--2012), 111(B6).

Lawton, T. F., & Trexler, J. H. (1991). Piggyback basin in the Sevier thrust belt, Utah: implications for development of the thrust wedge. Geology, 19, 827-830.

Lefever, R. D., Thompson, S. C., & Anderson, D. B. (1987). Earliest Paleozoic history of the Williston Basin in North Dakota. Saskatchewan Geological Society Special Publication, 9, 22-36.

Lekić, V., & Fischer, K. M. (2014). Contrasting lithospheric signatures across the western United States revealed by Sp receiver functions. Earth and Planetary Science Letters, 402, 90–98.

Lemieux, S., Ross, G. M., & Cook, F. A. (2000). Crustal geometry and tectonic evolution of the Archean crystalline basement beneath the southern Alberta Plains, from new seismic reflection and potential-field studies. Canadian Journal of Earth Sciences, 37(11), 1473–1491. https://doi.org/10.1139/e00-065

Li, A., Fischer, K. M., Wysession, M. E., & Clarke, T. J. (1998). Mantle discontinuities and temperature under the North American continental keel. Nature, 395(6698), 160.

Li, X., Kind, R., Priestley, K., Sobolev, S. V, Tilmann, F., Yuan, X., & Weber, M. (2000). Mapping the Hawaiian plume conduit with converted seismic waves. Nature, 405(6789), 938.

Li, X., Yuan, X., & Kind, R. (2007). The lithosphere-asthenosphere boundary beneath the western United States, Geophysical Journal International, 170(2), 700–710.

Li, Y.G., Vidale, J.E., Oglesby, D.D., Day, S.M., & Cochran, E. (2003). Multiple-fault rupture of the M7.1 Hector Mine, California, earthquake from fault zone trapped waves. J. geophys. Res., 108(B3).

Liu, L., & Gao, S. S. (2018). Lithospheric layering beneath the contiguous United States constrained by S-to-P receiver functions. Earth and Planetary Science Letters, 495, 79–86.

Liu, l., Klemperer, S. L., & Blanchette, A. R. (2021). Western Gondwana imaged by S receiver-functions (SRF): New results on Moho, MLD (mid-lithospheric discontinuity) and LAB (lithosphere-asthenosphere boundary). Gondwana Research, 96, 206-218.

Liu, L., Spasojević, S., & Gurnis, M. (2008). Reconstructing Farallon plate subduction beneath North America back to the Late Cretaceous. Science, 322(5903), 934–938.

Lyon-Caen, H., & Molnar, P. (1985). Gravity Anomalies, Flexure of the Indian Plate, and the Structure, Support, and Evolution of the Himalaya and Ganga Basin. Tectonics, 4, 513-538.

Lyon-Caen, H., & Molnar, P. (1989). Constraints on the deep structure and dynamic processes beneath the Alps and adjacent regions from an analysis of gravity anomalies. Geophys. J. Int., 99(1), 19-32.

MacKay, P., & Pedersen, P. K. (2022). The Western Canada Sedimentary Basin: A confluence of science, technology, and ideas. AAPG Bulletin, 106(3), 655-676.

Majorowicz, J., & Grasby, S. E. (2010). Heat flow, depth--temperature variations and stored thermal energy for enhanced geothermal systems in Canada. Journal of Geophysics and Engineering, 7(3), 232.

Masson, F., Jacob, A., Prodehl, C., Readman, P., Shannon, P., Schulze, A., & Enderle, U. (1998). A wide-angle seismic traverse through the Variscan of southwest Ireland. Geophysical Journal International, 134(3), 689-705.

McGregor, C. R. (1986). Subsurface Precambrian of southwestern Manitoba. Mineral Resource Division, Preliminary Map No. 1986 C-1.

McGregor, C. R., Bezys, R. K., & McCabe, H. R. (1990). Subsurface Precambrian structure of the Grand Rapids and Wekusko Lake area. Manitoba Mineral Resources Division, Preliminary Map 1990 M-2.

Meijer Drees, N. C. (1994). Devonian Elk Point Group of the Western Canada Sedimentary Basin, Geological atlas of the Western Canada Sedimentary Basin. Compiled by GD Mossop and I. Shetsen. Canadian Society of Petroleum Geologists and Alberta Research Council, Calgary, Alta, 129 – 147.

Mercier, J., Bostock, M. G., Audet, P., Gaherty, J. B., Garnero, E. J., & Revenaugh, J. (2008). The teleseismic signature of fossil subduction: Northwestern Canada. Journal of Geophysical Research: Solid Earth, 113(B4).

Mercier, J. P., Bostock, M. G., Cassidy, J. F., Dueker, K., Gaherty, E. J., Garnero, E. J., Revenaugh, J., & Zandt, G. (2009). Body-wave tomography of western Canada. Tectonophysics, 475(3–4), 480–492.

Miall, A. D. (1981). Alluvial sedimentary basins: tectonic setting and basin architecture. Spec. Pap. geol. Ass. Can., 23, 1–33.

Monger, J. W. H., & Price, R. A. (1979). Geodynamic evolution of the Canadian Cordillera – progress and problems. Canadian Journal of Earth Sciences, 16, 770-791. https://doi.org/10.1139/e79-069

Monger, J. W. H., & Price, R. A. (2002). The Canadian Cordillera: Geology and Tectonic Evolution. CSEG Recorder. 17.

Montagner, J. P., & Kennett, B. (1996). How to reconcile body-wave and normal-mode reference Earth models. Geophysical Journal International, 125(1), 229-248.

Mueller, S., & Landisman, M. (1966). Seismic studies of the Earth's crust in continents I: Evidence for a low-velocity zone in the upper part of the lithosphere*, Geophys. J. R. Astron. Soc., 10(5), 525–538.

Murphy, D. C., Mortensen, J. K., Piercey, S. J., Orchard, M. J., & Gehrels, G. E. (2006). Mid-Paleozoic to early Mesozoic tectonostratigraphic evolution of Yukon-Tanana and Slide Mountainterranes and affiliated overlap assemblages, Finlayson Lake massive sulphide district, southeastern Yukon. In Paleozoic Evolution and Metallogeny of Pericratonic Terranes at the

Ancient Pacific Margin of North America, Canadian and Alaskan Cordillera. Edited by M. Colpron and J.L. Nelson. Geological Association of Canada Special Paper, 45: 75-105.

Naghizadeh, M., Smith, R., Rubingh, K., Sherlock, R., Ayer, J., Lafrance, B., Cheraghi, S., Snyder, D., Vergne, J., Hollis, D., & Mordret, A. (2022). Active and passive seismic imaging of the central Abitibi Greenstone Belt, Larder Lake, Ontario. Journal of Geophysical Research: Solid Earth, 127(2).

Nelson, K. D., et al. (1996). Partially molten middle crust beneath southern Tibet: Synthesis of project INDEPTH results. Science, 274(5293), 1684-1688.

Nieuwenhuis, G., Unsworth, M. J., Pana, D., Craven, J., & Bertrand, E. (2014). Three- dimensional resistivity structure of Southern Alberta, Canada: Implications for precambrian tectonics. Geophysical Journal International, 197(2), 838–859. https://doi.org/10.1093/gji/ggu068

Niu, F., Bravo, T., Pavlis, G., Vernon, F., Rendon, H., Bezada, M., & Levander, A. (2007). Receiver function study of the crustal structure of the southeastern Caribbean plate boundary and Venezuela. Journal of Geophysical Research: Solid Earth, 112(B11). https://doi.org/10.1029/2006JB004802

Nurkowski, J. R. (1985). Coal quality and rank variations within Upper Cretaceous and Tertiary sediments, Alberta Plains region. Alberta Research Council, Earth Sciences Report, 85(1), 42.

O'Connell, S. C., & Bell, J. S. (eds.). (1990). Geology of the Peace River Arch. Bulletin of Canadian Petroleum Geology, 38(A).

Olugboji, T. M., Park, J., Karato, S.-I., & Shinohara, M. (2016). Nature of the seismic lithosphere-asthenosphere boundary within normal oceanic mantle from high-resolution receiver functions. Geochemistry, Geophysics, Geosystems, 17(4), 1265-1282.

Osadetz, K. G., Pearson, D. E., & Stasiuk, L. D. (1990). Paleogeothermal gradients and changes in the geothermal gradient of the Alberta Plains. Current Research, Part D, Geological Survey of Canada, Paper 90-1D, 165-178. https://doi.org/10.4095/131352

Owens, T. J., Zandt, G. & Taylor, S. R. (1984). Seismic evidence for an ancient rift beneath the Cumberland Plateau, Tennessee: A detailed analysis of broadband teleseismic P waveforms. Journal of Geophysical Research: Solid Earth (1978-2012), 89(B9), 7783-7795.

Pana, D.I. (2003): Precambrian basement of the Western Canada Sedimentary Basin in northern Alberta; Alberta Energy and Utilities Board, EUB/AGS Earth Sciences Report 2002-02, 39.

Pană, D. I., & Elgr, R. (2013): Geology of the Alberta Rocky Mountains and Foothills. Energy Resources Conservation Board, ERCB/AGS Map 560.

Parcell, W. C., & Williams, M. K. (2005). Mixed sediment deposition in a retro-arc foreland basin: Lower Ellis Group (M. Jurassic), Wyoming and Montana, U.S.A.. Sedimentary Geology, 177, 175-194.

Passey, Q. R., Creaney, S., Kulla, J. D., Moretti, F., & Stroud, J. D. (1990). A practical model for organic richness from porosity and resistivity logs. American Association of Petroleum Geologists, Bulletin, 74, 1777-1794.

Pasyanos, M. E., Masters, T. G., Laske, G., & Ma, Z. (2014). LITHO1.0: An updated crust and lithospheric model of the Earth. Journal of Geophysical Research: Solid Earth, 119(3), 2153–2173.

Patton, T. L., & O'Conner, S. J. (1988). Cretaceous flexural history of northern Oman mountain foredeep, United Arab Emirates. Bull. Am. Ass. petrol. Geol., 72, 797–809.

Peterson, J. A., & MacCray, L. M. (1987). Regional stratigraphy and general petroleum geology of the U.S. portion of the Williston Basin and adjacent area. Rocky Mountain Association of Geologists, 9-43.

Pfiffner, O. A., Schlunegger, F., & Buiter, S. J. H. (2002). The Swiss Alps and their peripheral foreland basin: Stratigraphic response to deep crustal processes. Tectonics, 21(6), 4-1-4-3.

Pirera, F., & Zanzi, L. (1993). The reflectivity method as a tool for evaluating the seismic response of layered structures. Journal of Applied Geophysics, 30(1-2), 35-41. https://doi.org/10.1016/0926-9851(93)90016-R

Porter, J. W., Price, R. A., & McCrossan, R. G. (1982). The Western Canada Sedimentary Basin. Philosophical Transactions of the Royal Society of London, A305, 169-182.

Press, W. H., Teukolsky, S. A., Vetterling, W. T., & Flannery, B. P. (1992). Numerical Recipes in C, 2nd Ed., Cambridge University Press.

Price, R. A. (1973). Large-scale gravitational flow of supracrustal rocks, southern Canadian Rockies. Gravity and Tectonics. K. A. Jong and R. Scholten (eds.). New York, Weiley and Sons, 491-502.

Price, R. A. (1986). The southeastern Canadian Cordillera: thrust faulting, tectonics wedging, and delamination of the lithosphere. Journal of Structural Geology, 8, 239-254.

Price, R. A. (1994). Cordilleran Tectonics and the Evolution of the Western Canada Sedimentary Basin, Geological atlas of the Western Canada Sedimentary Basin. Compiled by GD Mossop and I. Shetsen. Canadian Society of Petroleum Geologists and Alberta Research Council, Calgary, Alta, 13 – 24.

Price, R. A., & Fermor, P. R. (1984). Structure section of the Cordilleran Foreland Thrust and Fold Belt west of Calgary. Geological Survey of Cnada Map 1501A.

Price, R. A., & Mountjoy, E. W. (1970). Geological structure of the Canadian Rocky Mountains between Bow and Athabasca Rivers: A progress report. Structure of the Southern Canadian Cordillera. J. O. Wheeler (ed.). Geological Association of Canada, Special Publication No. 6, 7-25.

Prior, G., Hathway, B., Glombick, P., Pană, D. I., Banks, C. J., Hay, D. C., Schneider, C. L., Grobe, M., Elgr, R., & Weiss, J. (2013): Bedrock Geology of Alberta. Alberta Energy Regulator, AER/AGS Map 600.

Quinlan, G., & Beaumont, C. (1984). Appalachian thrusting, lithospheric flexure and the Paleozoic stratigraphy of the Eastern Interior of North America. Can. J. Earth Sciences, 21, 973-996.

Rankin, D. W., Dillon, W. P., Black, D. F. B., Boyer, S. E., Daniels, D. L., Goldsmith, R., Grow, J. A., Horton, J. W., Hutchinson, D. R., Klitgord, K. D., McDowell, R. C., Milton, D. J., Owens, J. P., & Phillips, J. D. (1991). DNAG Centennial Continent/Ocean Transect #16, Volume E-4: Central Kentucky to the Carolina Trough. Geol. Soc. Am..

Reid, S. K., & Dorobek, S. L. (1993). Sequence stratigrpahy and evolution of a progradational, foreland carbonate ramp, Lower Mississippian Missian Canyon Formation and stratigraphic equivalents, Montana and Idaho. Mem. Am. Ass. petrol. Geol., 57, 327–352.

Riba, O. (1976). Syntectonic unconformities of the Alto Cardener, Spanish Pyrenees: a genetic interpretation. Sed. Geol., 15, 213–233.

Ricketts, B. D. (2008). Chapter 10: Cordilleran Sedimentary Basins of Western Canada Record 180 Million Years of Terrane Accretion, Sedimentary Basins of the World by Miall, A. D. (eds), 5, 363-394.

Roecker, S. (2001). Constraints on the crust and upper mantle of the Kyrgyz Tien Shan from the preliminary analysis of GHENGIS broad-band seismic data. Geologiya I Geofizika, 42, 1554-1565.

Rohais, S., Crombez, V., Euzen, T., & Zonneveld, J. (2018). Subsidence dynamics of the Montney Formation (Early Triassic, Western Canada Sedimentary Basin): insights for its geodynamic setting and wider implications. Bulletin of Canadian Petroleum Geology, 66(1), 128 – 160.

Rondenay, S. (2009). Upper mantle imaging with array recordings of converted and scattered teleseismic waves. Surveys in Geophysics, 30(4–5), 377–405. https://doi.org/10.1007/s10712-009-9071-5

Ross, G. M., Broome, J., & Miles, M. (1994). Potential Fields and Basement Structure - Western Canada Sedimentary Basin, Geological atlas of the Western Canada Sedimentary Basin. Compiled by GD Mossop and I. Shetsen. Canadian Society of Petroleum Geologists and Alberta Research Council, Calgary, Alta, 41 – 47.

Ross, G. M. & Eaton, D. W. (1997). Winagami reflection sequence: Seismic evidence for postcollisional magmatism in the Proterozoic of western Canada. Geology, 25(3), 199-202.

Ross, G. M., & Eaton, D. W. (2002). Proterozoic tectonic accretion and growth of western Laurentia: results from Lithoprobe studies in northern Alberta. Canadian Journal of Earth Sciences, 39(3), 313–329. https://doi.org/10.1139/e01-081

Ross, G. M., Eaton, D. W., Boerner, D. E., & Miles, W. (2000). Tectonic entrapment and its role in the evolution of continental lithosphere: An example from the Precambrian of western Canada. Tectonics, 19(1), 116–134. https://doi.org/10.1029/1999TC900047

Ross, G. M., Milkereit, B., Eaton, D., White, D., Kanasewich, E. R., & Burianyk, M. J. A. (1995). Paleoproterozoic collisional orogen beneath the Western Canada Sedimentary Basin imaged by Lithoprobe crustal seismic-reflection data. Geology, 23(3), 195–199.

Ross, G. M., & Stephenson, R. A. (1989). Crystalline basement: the foundations of the Western Canada Sedimentary Basin. Canadian Society of Petroleum Geologists, 33-46.

Ross, G. M., Villeneuve, M. E., Parrish, R. R., & Bowring, S. A. (1989). Tectonic subdivision and U-Pb geochronology of the Precambrian basement of the Alberta Basin, western Canada. Geological Survey of Canada, Open File Report 2103.

Ross, G. M., Villeneuve, M. E., Parrish, R. R., & Bowring, S. A. (1991). Geophysics and geochronology of the crystalline basement of the Alberta Basin, Western Canada. Canadian Journal of Earth Sciences, 28, 512-522. https://doi.org/10.1139/e91-045

Rost, S., & Thomas, C. (2002). Array seismology: methods and applications. Rev. Geophys., 40, 1008.

Rost, S., & Thomas, C. (2009). Improving seismic resolution through array processing techniques. Surveys in Geophysics, 30(4-5), 271-299.

Royden, L. H. (1993). The tectonic expression of slab pull at continental convergent boundaries. Tectonics, 12, 303–325.

Saikia, S., Chopra, S., Baruah, S., & Singh, U. K. (2017). Shallow sedimentary structure of the Brahmaputra Valley constraint from Receiver Functions analysis. Pure and Applied Geophysics 174, 229-247. https://doi.org/10.1007/s00024-016-1371-3

Sambridge, M., & Drijkoningen, G. (1992). Genetic algorithms in seismic waveform inversion. Geophysical Journal International, 109(2), 323-342.

Scales, J. A., Smith, M. L., & Fischer, T. L. (1992). Global optimization methods for highly multimodal inverse problems. Journal of Computational Physics, 101(1), 228-229.

Schlunegger, F., & Mosar, J. (2011). The last erosional stage of the Molasse Basin and the Alps. International Journal of Earth Sciences, 100, 1147-1162.

Schmandt, B., Lin, F. C., & Karlstrom, K. E. (2015). Distinct crustal isostasy trends east and west of the Rocky Mountain Front. Geophysical Research Letters, 42(23).

Schultz, R., & Stern, V. (2015). The Regional Alberta Observatory for Earthquake Studies Network (RAVEN) [Data set]. CSEG Recorder, 40(8), 34–37. https://doi.org/10.7914/SN/RV

Selway, K., Ford, H., & Kelemen, P. (2015). The seismic mid-lithosphere discontinuity. Earth and Planetary Science Letters, 414, 45-57.

Sengor, A. M. C. (1995). Sedimentation and tectonics of fossil rifts. In: Tectonics of Sedimentary Basisn (Ed. by C. J. Busby & R. V. Ingersoll). Blackwell Science, Oxford, 53–117.

Shearer, P. M. (2019). Introduction to seismology. Cambridge Press.

Shragge, J., Bostock, M. G., Bank, C. G., & Ellis, R. M. (2002). Integrated teleseismic studies of the southern Alberta upper mantle. Canadian Journal of Earth Sciences, 39(3), 399–411.

Sims, P. K., Lund, K., & Anderson, E. (2005). Precambrian crystalline basement map of Idaho — An interpretation of aeromagnetic anomalies. U.S. Geological Survey Scientific Investigations Map 2884.

Sinclair, H. D., & Allen, P. A. (1992). Vertical vs. horizontal motions in the Alpine orogenic wedge: stratigraphic response in the foreland basin. Basin Res., 4, 215–232.

Sinclair, H. D. (1997). Tectonostratigraphic model for underfilled peripheral foreland basins: An Alpine perspective. GSA Bulletin, 109(3), 324-346.

Sinha, R., & Friend, P. F. (1994). River systems and their sediment flux, Indo-Gangetic plains, northern Bihar, India. Sedimentology, 41, 825–845.

Sloss, L. L. (1988). Forty years of sequence stratigraphy. Geological Society of America, 100, 1661-1665. https://doi.org/10.1130/0016-7606(1988)100<1661:FYOSS>2.3.CO;2

Snieder, R., & Romanowicz, B. (1988). A new formalism for the effect of lateral heterogeneity on normal modes and surface waves: I Isotropic perturbations, perturbations of interfaces and graqvitational perturbations. Geophysical Journal International, 92(2), 207-221.

Song, P., Zhang, X., Liu, Y., & Teng, J. (2017). Moho imaging based on receiver function analysis with teleseismic wavefield reconstruction: Application to South China. Tectonophysics, 718, 118-131.

Srivastava, P., & Mitra, G. (1994). Thrust geometrics and deep structure of the outer and lesser Himalaya, Kumaon and Garhwal (India): implications for evolution of the Himalayan fold-and-thrust belt. Tectonics, 13, 89-109.

Stern, R. J. (2002). Subduction zones. Reviews of Geophysics, 40(4), 1–3. https://doi.org/10.1029/2001rg000108

Stern, T. A., Okaya, D., Kleffmann, S., Scherwath, M., Henrys, S., & Davey F. J. (2007). Geophysical exploration and dynamics of the Alpine Fault Zone, in A Continental Plate Boundary: Tectonics at South Island, New Zealand, AGU Geophys. Monogr. Ser., vol. 175, edited by Okaya, D., Stern, T., & Davey, F., pp. 207–233, AGU, Washington, D. C.

Stewart, J. H. (1972). Initial deposits of the Cordilleran geosyncline: Evidence of Late Precambrian (<850 Ma) continental separation. Geological Society of America Bulletin, 83, 1345-1360.

Stoffa, P. L., & Sen, M. K. (1991). Nonlinear multiparameter optimization using genetic algorithms: inversion of plane-wave seismograms. Geophysics, 56, 1794–1810. https://doi.org/10.1190/1.1442992

St-Onge, M. R., Searle, M. P., & Wodicka, N. (2006). Trans-Hudson orogen of North America and Himalaya-Karakoram-Tibetan orogen of Asia: Structural and thermal characteristics of the lower and upper plates, Tectonics, 25, TC4006.

Suman, S., & Giri, V. K. (2015). Genetic algorithms: basic concepts and real world applications. International Journal of Electrical, Electronics and Computer System, 3, 116-123.

Svenningsen, L., & Jacobsen, B. H. (2007). Absolute S-velocity estimation from receiver functions. Geophysical Journal International, 170, 1089 – 1138. https://doi.org/10.1111/j.1365-246X.2006.03505.x

Sweeney, J. F., Stephenson, R. A., Currie, R. G., & Delaurier, J. M. (1991). Geology of the Cordilleran Orogen in Canada, Chapter 2, Part C, Crustal geophysics. Geology of Canada, 4, 39-59.

Tatham, R. H. (1982). Vp/Vs and Lithology. Geophysics, 47(3), 336 – 344. https://doi.org/10.1190/1.1441339

Tesoniero, A., Auer, L., Boschi, L., & Cammarano, F. (2015). Hydration of marginal basins and compositional variations within the continental lithospheric mantle inferred from a new global model of shear and compressional velocity. Journal of Geophysical Research: Solid Earth, 120(11), 7789–7813.

Thomas, G. E. (1974). Lineament block tectonics: Williston-Blood Creek basins. American Association of Petroleum Geologists Bulletin, 58, 1305-1322.

Tobon, Z. L. M. (2012), Near-surface characterization and Vp/Vs analysis of a shale gas basin. MS thesis, University of Calgary, Canada.

Turcotte, D. L., & Schubert, G. (1982). Geodynamics: Applications of Continuum Physics to Geological Problems. John Wiley & Sons, New York, NY.

Van der Lee, S., & Frederiksen, A. (2005). Surface wave tomography applied to the North American upper mantle. Seismic Earth: Array Analysis of Broadband Seismograms, 67–80.

Vidale, J., & Li, YG. (2003). Damage to the shallow Landers fault from the nearby Hector Mine earthquake. Nature, 421, 524–526.

Villeneuve, M. E., Ross, G. M., Thériault, R. J., Miles, W., Parrish, R. R., & Broome, J. (1993). Tectonic subdivision and U-Pb geochronology of the crystalline basement of the Alberta Basin, Western Canada. Geological Survey of Canada, Bulletin 447. https://doi.org/10.4095/77642

Wang, J., Gu, Y. J., & Chen, Y. (2020). Shear velocity and radial anisotropy beneath southwestern Canada: Evidence for crustal extension and thick-skinned tectonics. Journal of Geophysical Research: Solid Earth, 125, e2019JB018310. https://doi.org/10.1029/2019JB018310

Wanless, R. K. (1970). Isotropic age map of Canada. Geological Survey of Canada, Map 1256A.

Ward, K. M., Porter, R. C., Zandt, G., Beck, S. L., Wagner, L. S., Minaya, E., & Tavera, H. (2013). Ambient noise tomography across the Central Andes. Geophysical Journal International, 194(3), 1559–1573.

Welford, J. K., & Clowes, R. M. (2006). Three-dimensional seismic reflection investigation of the upper crustal Winagami sill complex of northwestern Alberta, Canada. Geophysical Journal International, 166(1), 155–169. https://doi.org/10.1111/j.1365-246X.2006.02805.x

Wessel, P., Smith, W. H., Scharroo, R., Luis, J. & Wobbe, F. (2013). Generic mapping tools: Improved version released, Eos Trans. AGU, 94(45), 409-410. https://doi.org/10.1002/2013EO450001

Wölbern, I., Heit, B., Yuan, X., Asch, G., Kind, R., Viramonte, J., Tawackoli, S., & Wilke, H. (2009). Receiver function images from the Moho and the slab beneath the Altiplano and Puna plateaus in the Central Andes, *Geophysical Journal International*, 177(1), 296–308.

Wolf, M. B., & Wyllie, P. J. (1993). Some products of experimental dehydration-melting of amphibolite at 10 kbar. Russian Geology and Geophysics, 34 (12), 90-102.

Woodhouse, J. H., & Dziewonski, A. M. (1984). Mapping the upper mantle: three-dimensional modeling of earth structure by inversion of seismic waveforms. Journal of Geophysical Research: Solid Earth. 89(B7), 5953-5986.

Wright, G. N. (1984). The Western Canada Sedimentary Basin, a series of geological sections illustrating basin stratigraphy and structure. Canadian Society of Petroleum Geologist and the Geological Association of Canada.

Wright, G. N., McMechan, M. E., & Potter, D. E. G. (1994). Structure and Architecture of the Western Canada Sedimentary Basin, Geological atlas of the Western Canada Sedimentary Basin. Compiled by GD Mossop and I. Shetsen. Canadian Society of Petroleum Geologists and Alberta Research Council, Calgary, Alta, 25 – 40.

Wu, Lei, Gu, Y. J., Chen, Y., & Liang, H. (2019). Shear wave splitting discloses two episodes of collision-related convergence in western North America. Journal of Geophysics Research: Solid Earth, 124(3), 2990-3010.

Wyession, M. E., & Fischer, K. M. (2001). The Florida to Edmonton Broadband Experiment [Data set]. International Federation of Digital Seismograph Networks.

Xie, W. (2014). Seismic characterization of a possible buried impact structure near Bow City in Southern Alberta. MS thesis, University of Alberta, Canada

Yang, Y., Ritzwoller, M. H., Zheng, Y., Shen, W., Levshin, A. L., & Xie, Z. (2012). A synoptic view of the distribution and connectivity of the mid-crustal low velocity zone beneath Tibet. J. Geophys. Res., 117, B04303.

Yang, H., & Zhu, L. (2010). Shallow low-velocity zone of the San Jacinto fault from local earthquake waveform modelling, Geophysical Journal International, 183(1), 421–432. https://doi.org/10.1111/j.1365-246X.2010.04744.x

Yeck, W. L., Sheehan, A. F., & Schulte-Pelkum, V. (2013). Sequential H-κ stacking to obtain accurate crustal thicknesses beneath sedimentary basins. Bulletin of the Seismological Society of America. https://doi.org/10.1785/0120120290

Yuan, X., et al. (2000), Subduction and collision processes in the Central Andes constrained by converted seismic phases, Nature, 408(6815), 958–961.

Zandt, G., Velasco, A. A. & Beck, S. L. (1994). Composition and thickness of the southern Altiplano crust, Bolivia, Geology, 22(11), 1003-1006.

Zhang, P., Yao, H., Chen, L., Fang, L., Wu, Y., & Feng, J. (2019). Moho depth variations from receiver function imaging in the northeastern North China Craton and its tectonic implications. J. Geophys. Res.: Solid Earth, 124(2), 1852-1870.

Zheng, T., Zhao, L., & Chen, L. (2005). A detailed receiver function image of the sedimentary structure in the Bohai Bay Basin. Physics of the Earth and Planetary Interiors, 152(2005), 129-143.

Zheng, T., Zhao, L., & Zhu, R. (2009). New evidence from seismic imaging for subduction during assembly of the North China Craton. Geology, 37(5), 395–398.

Zhu, L., & Kanamori, H. (2000), Moho depth variation in southern California from teleseismic receiver functions. Journal of Geophysical Research, 105(B2), 2969 – 2980.

Zorin, Y. A., Mordvinova, V., Turutanov, E. K., Belichenko, B., Artemyev, A., Kosarev, G., & Gao, S. (2002). Low seismic velocity layers in the Earth's crust beneath Eastern Siberia (Russia) and Central Mongolia: receiver function data and their possible geological implication. Tectonophysics, 359(3), 307-327.